Microfluidics for cell manipulation and analysis

Despina Nelie Loufakis

Dissertation submitted to the faculty of the Virginia Polytechnic Institute and State University in partial fulfillment of the requirements for the degree of

Doctor of Philosophy
In
Chemical Engineering

Chang Lu

Donald Baird

Rafael Davalos

Richey Davis

09/04/2014

Blacksburg, VA

Keywords: microfluidics, mammalian cells, cell focusing, electrical cell lysis, cell electroporation, chamber formation, hydrodynamic focusing

Microfluidics for cell manipulation and analysis

Despina Nelie Loufakis

ABSTRACT

Microfluidic devices are ideal for analysis of biological systems. The small dimensions result to controlled handling of the flow profile and the cells in suspension. Implementation of additional forces in the system, such as an electric field, promote further manipulation of the cells. In this dissertation, I show novel, unique microfluidic approaches for manipulation and analysis of mammalian cells by the aid of electrical methods or the architecture of the device. Specifically, for the first time, it is shown, that adoption of electrical methods, using surface electrodes, promotes cell concentration in a microchamber due to isoelectric focusing (IEF). In contrast to conventional IEF techniques for protein separation, a matrix is not required in our system, the presence of which would even block the movement of the bulky cells. Electric field is, also, used to breach the cell membrane and gain access to the cell interior by electroporation (irreversible and reversible). Irreversible electroporation is used in a unique, integrated microfluidic device for cell lysis and reagentless extraction of DNA. The genomic material is subsequently analyzed by on-chip PCR, demonstrating the possible elimination of the purification step. On the other hand, reversible electroporation is used for the delivery of exogenous molecules to cells. For the first time, the effect of shear stress on the electroporation efficiency of both attached and suspended cells is examined. On the second part of my dissertation, I explore the capabilities of the

architecture of microfluidic devices for cell analysis. A simple, unique method for compartmentalization of a microchamber in an array of picochambers is presented. The main idea of the device lies on the fabrication of solid supports on the main layer of the device. These features may even hold a dual nature (e.g. for cell trapping, and chamber support), in which case, single cell analysis is possible (such as single cell PCR). On the final chapter of my dissertation, a computational analysis of the flow and concentration profiles of a device with hydrodynamic focusing is conducted. I anticipate, that all these novel techniques will be used on integrated microfluidic systems for cell analysis, towards point-of-care diagnostics.

"Πάντες ἄνθρωποι τοῦ εἰδέναι ὀρέγονται φύσει"

All men by nature desire to know

- Aristotle, 384-322 B.C

"Ἓν οἶδα ὅτι ουδὲν οἶδα"

I know that I know nothing

- Socrates, 469-399 B.C.

AKNOWLEDGMENTS

The completion of this dissertation would not have been accomplished without the support from my teachers, friends, and family. They have all played a significant role in my life, and have helped me become the person and researcher I am today. Their contribution has been invaluable to me. I would like to thank each of them separately in the following lines.

First of all, I would like to express my gratitude to my advisor and head of my committee, Dr. Chang Lu, for his guidance and support. His expertise in the field of microfluidics, and his enthusiasm to pass part of his knowledge to me, have helped me advance to a mature researcher. I value his guidance and mentorship in academic and career matters. I am, also, grateful for the financial support he provided to me. I feel very lucky and honored to have worked with him, and serve as an academic child of his.

I would also like to thank the rest of committee members, Dr. Donald Baird, Dr. Rafael Davalos, and Dr. Richey Davis for their insightful feedback and advices. Their support and contribution during my dissertation has been very important. Special thanks also go to Dr. David Mittelman at VBI and his graduate student Robin Varghese. Their proficiency in the field of genomics, guided me through my experiments on PCR.

I am very grateful to the department of chemical engineering at Virginia Tech for the great working environment. The staff have gladly offered their help and support numerous times on administrative and technical matters. On the same time, the faculty members, who are always interested in interdisciplinary topics and possible collaborations, have provided interesting comments, and have offered help at all times. Finally, the graduate student body, and its organization ChEGSA (Chemical Engineering Graduate Student Assembly), created a very

friendly environment both at work and outside it. I am also grateful to the department for awarding me with the Pratt and Hord Fellowships that came with financial support.

I also want to thank a lot my current labmates Zhenning Cao, Chen Sun, Sai Ma, Yan Zhu, Travis Murphy, and my former labmates Hamid Hassanisaber, Dr. Tao Geng, Dr. Yihong Zhan, Dr. Ning Bao. I thank them for the interesting conversations we have had over several research topics; the observation of a problem from different points of view and by experts is always very amusing, and efficient. Their friendship and support have made the countless hours spent in the lab very pleasant. These friends, along with the rest of my friends in VA, have made life in Blacksburg an incredible experience. I am glad we have established concrete friendships, which I trust, they will last for many years to come.

Last but not least, I would like to thank my family and friends back home for their continuous love and support. Especially, I want to thank my parents Kyriakos, and Rea, and my brothers Akis and Dimitris, who I cherish and admire. They have always been there for me, supporting me in every way and helping me overcome all difficulties. Their unconditional love has been an inspiration to me.

Above all, I want to thank my husband and best friend, Polydefkis, for his love, and support at all times. With him by my side, every step of the way is a wonderful adventure. Σ'αγαπώ.

TABLE OF CONTENTS

LIST OF FIGURES

LIST OF TABLES

LIST OF ABBREVIATIONS

SYMBOL	***DESCRIPTION***
pI	Isoelectric point
IEF	Isoelectric focusing
CHO	Chinese hamster ovary cells
1- ,2- ,3 - D	1- , 2- ,3- dimensions
R	Reaction
k	Reaction constant
E	Electric field intensity
d	Diameter
DNA	Deoxyribonucleic acid
RNA	Ribonucleic acid
SDS	Sodium dodecyl sulfate
PCR	Polymerase chain reaction
RT-PCR	Real time-PCR
AC	Alternating current
DC	Direct current
dNTPs	Deoxyribonucleotides
C_t	Threshold cycle
PDMS	Polydimethylsyloxane
PEG	Polyethyleneglycol
qPCR	Quantitative PCR

DIC	Differential interference contrast
$\Delta\psi_E$	Transmembrane potential
θ	Angle between the direction of the electric field and the normal of the cell starting from its center
ITO	Indium tin oxide
A	Area
W	Width
L	Length
PBS	Phosphate buffer saline
U_{max}	Maximum velocity
Q	Flow rate
T	Residence time
LOC	Lab-on-a-chip
μTAS	Micro total analysis system
DEP	Dielectrophoresis
CTC	Circulating tumor cell
RBC	Red blood cell
AFM	Atomic force microscopy
P	Pressure
g	Gravitational constant
v	Velocity
μ	Viscosity
ρ	Density

c	Concentration
D	Diffusion coefficient
EGFP	Enhanced green fluorescent protein
PI	Propidium Iodide

CHAPTER 1 – OVERVIEW

The scope of this research was the generation and optimization of microfluidic techniques for cell manipulation, and analysis. The field of microfluidics holds a set of characteristics that is ideal for cell manipulation. The small dimensions result to two important aspects: the generation of features that are of the same order of magnitude as the cells (or channels that are one order of magnitude larger than the cells), and a laminar flow profile (i.e. low Reynolds number). The combination of the two, leads to excellent control of the flow, and controlled manipulation of the cell trajectory. Additionally, implementation of other forces in the system, such as electrical forces generated by an electric field, is very easy and helps to further manipulate and analyze the cells.

The field of microfluidics has raised a new set of analysis tools, the lab-on-a-chip (LOC) and the micro-total-analysis-system (μTAS) devices. They are mainly characterized by the miniaturization of a process, which would typically take place in a lab, to a portable microfluidic chip. Their main advantage is the capability of integration of several steps on one device, for continuous, automatic analysis. This is often accompanied with minimal human interaction, which can highly increase the reproducibility, and potentially be used by non-trained users. The applications of LOCs are largely focused on biomedical applications, during which analysis of biological matter results to detection, for prognosis and diagnosis purposes, or treatment, such as gene delivery.

A continuous effort is required for the generation of efficient methods to be used on LOC systems. Each step, such as manipulation of the cell trajectory or cell lysis, is based on a separate method, and needs careful and individual optimization. In the following chapters, I will discuss novel microfluidic techniques for cell manipulation and analysis. The implementation of electrical methods will be discussed and analyzed for applications involving mammalian cell concentration, lysis, and electroporation. On the last two chapters, I will discuss the capabilities of the architecture of the device. The generation of smart features can lead to easy compartmentalization of the device. Moreover, on the last chapter I show, that careful manipulation of the laminar flow profile can lead to controlled spatial dilution.

The thesis is divided in two parts, based on the presence (part I) or absence (part II) of electrical methods in the system. The main focus of each chapter is outlined briefly:

Part I

Chapter 2 – Focusing of mammalian cells under an ultrahigh pH gradient created by unidirectional electropulsation in a confined microchamber

A microfluidic technique for concentration of mammalian cells under electropulsation is discussed. During the pulses, a steep pH gradient is generated in the microchamber, due to water electrolysis. This change in the solution pH, alters the surface charge of cells in suspension, and alters their directionality. As a result, the cells immobilize and focus in a location, according to their pI.

Chapter 3 – Electrical lysis of mammalian cells followed by on-chip PCR of the extracted genomic DNA

Mammalian cells are lysed under electrical pulses in a microfluidic chamber, which is supplemented with surface electrodes. Their extracted genomic DNA is subsequently amplified during on-chip PCR. The advantage of this reagentless method is the absence of the purification step of the extracted DNA.

Chapter 4 – Shear stress induced electroporation

The effect of shear stress on the electroporation efficiency of cells in suspension and attached cells is examined in this chapter. Small molecules and plasmid DNA are delivered on mammalian cells during a pulsed electric field under different flow profiles. The shear stress is controlled by the geometry of the channel and the flow velocity. Computational data validate the flow profiles in the microchannel at all cases.

Part II

Chapter 5 – A simple method for chamber formation in microfluidic devices and its importance on single cell analysis and digital PCR

Compartmentalization of a microchannel is achieved in an efficient way. The two-layer LOC device has simple architecture. An array of microstructures in the fluidic layer, supports the formation of individual chambers around them, when the control layer, which is constituted by a

big, rectangular channel, is pressurized. The advantage of this method, is that the generation of chambers is reversible, allowing the samples to flow out of the device, after on-chip analysis.

Chapter 6 – Hydrodynamic focusing in microfluidic devices for controlled spatial dilution

Computational simulation of the concentration and flow profile of a microfluidic device for red blood cell (RBC) lysis was performed. The laminar flow profile showed excellent control of the concentration profile and controlled spatial dilution downward the device.

CHAPTER 2 – FOCUSING OF MAMMALIAN CELLS UNDER AN ULTRAHIGH PH GRADIENT CREATED BY UNIDIRECTIONAL ELECTROPULSATION IN A CONFINED MICROCHAMBER

2.1 INTRODUCTION

Proteins and peptides have both amine and carboxylic acid groups and these groups can either donate or accept protons. Therefore the charge of a protein/peptide molecule varies with the surrounding pH. The pH value at which a protein molecule carries no net surface charge is referred to as the isoelectric point (pI) and is an important physiochemical property. Isoelectric focusing (IEF) has been widely used for protein concentration and separation[1, 2]. In these experiments, carrier ampholytes (i.e. a mixture of molecules with multiple aliphatic and carboxylate groups) or acrylamido buffers (typically covalently incorporated into the gels) are used to establish a linear pH gradient in gels or capillary tubes. A direct current (dc) field is then applied to focus various molecules to their respective pI values. IEF has also been applied to small bioparticles[3] (with diameters <5 μm) such as viruses[4, 5], bacteria[6, 7], and yeasts[8]. In these works, special care was taken to use very low concentrations for these bioparticles to avoid interference due to the interactions between the bioparticles and the ampholyte matrix[8]. IEF of mammalian cells (with diameters

typically in the range of 10-20 μm) on a simple and practical platform has yet to be demonstrated, due to the potential cell entrapment in matrices.

The surface charge of mammalian cells is typically negative at physiological pH. Cells are covered by a surface coat that is rich in carbohydrate, referred to as glycocalyx. These carbohydrates include oligosaccharide chains covalently bound to membrane proteins (glycoproteins) and lipids (glycolipids)[9]. The carbohydrate portion of these molecules contains a significant amount of sialic acid residues that carry negative charges at physiological pH[10-12]. At the same time, the carbohydrate groups also contain amino sugars which may become positively charged under low pH[10, 11]. Thus we hypothesized that concentration or focusing of mammalian cells under a very high pH gradient would be potentially feasible. Such method may find applications in microfluidic total analysis systems that require cell manipulations[13-16].

Here, by exploiting the interplay among microfluidics, electrochemistry, and electrokinetics, we demonstrate IEF of mammalian cells in a simple microfluidic electrochemical chamber containing a low-conductivity buffer. We observed focusing of cells in a closed microfluidic chamber when unidirectional pulses were applied by two surface electrodes. Our experimental and computational results show that an ultrahigh pH gradient (up to 0.14 Unit/μm) was generated by electrolysis of water inside the confined microscale space under the application of the electric pulses. The pH gradient was highly nonlinear and steepest at the center of the chamber. We also studied the correlation between the electrophoretic mobility of cells and the local pH and estimated the pI of Chinese hamster ovary (CHO) cells to be in the range of 4.5-6.5. Our setting offers a simple approach to generate an ultrahigh pH gradient at microscale in free solution. Such conditions uniquely permit the focusing of mammalian cells without involving matrices.

2.2 MATERIALS AND METHODS

2.2.1 DEVICE OPERATION AND ELECTROPULSATION

A two-layer microfluidic device was fabricated by multilayer soft lithography based on PDMS (Appendix A). The microfluidic device was mounted on an inverted fluorescence microscope (IX-71, Olympus, Melville, NY) equipped with a 10× dry objective and a CCD camera (ORCA-285; Hamamatsu, Bridgewater, NJ). The fluidic layer was flushed by the phosphate buffer supplemented with Tween 20 at 0.02% before the experiments, using a syringe pump (Fusion400, Chemyx, Stafford, TX). The surface electrodes were connected to a high voltage reed relay (5501, Coto Technology, North Dingstown, RI) and a dc power supply (PS350, Stanford Research Systems, Sunnyvale, CA) for application of electric pulses of milliseconds. A schematic of the system setup is illustrated in Fig. 2.1 and the setup was similar to that in our previous publication[17].

2.2.2 CELL SUSPENSIONS

CHO-K1 and Jurkat cells were cultured according to the protocol (Appendix B). Before the experiment they were harvested and resuspended in a low-conductivity phosphate buffer (4.8 mM Na_2HPO_4, 1.2 mM KH_2PO_4, and 250 mM sucrose, pH=7.4, unless otherwise specified) at a concentration of 3×10^6 cells/ml as determined by a hemocytometer. In the case where they were fluorescently labeled, Hoechst 33342 (Life Technologies Corporation, Grand Island, NY) was added to the cells medium (Appendix B).

2.2.3 IMAGE ANALYSIS

Image analysis was performed using a software package Fiji in order to extract the velocity of cells in the fluorescence image series[18]. A MATLAB (Mathworks, Natick, MA) code was written for analyzing the standard deviations in the cell location.

2.2.4 COMSOL MODELING

COMSOL Multiphysics 4.3 (Burlington, MA) was used to simulate the pH profiles in the microfluidic chamber. The "Transport of Diluted Species" module was used to simulate the H^+ OH^-, HPO_4^{2-}, $H_2PO_4^-$ concentration profiles due to diffusion and generation/consumption for 500 seconds (the duration of applying 50 pulses). A 1-D geometry was determined to be sufficient to accurately solve the concentration profiles. *Eqn. 1* was used to compute the concentrations of the ions.

$$\frac{\partial c_i}{\partial t} + \nabla \cdot (-D_i \nabla c_i) = R_i \qquad \textit{Eqn 1}$$

where c_i is the concentration of species i, D_i is the diffusion coefficient, and R_i is the generation or consumption of ions due to electrochemical reactions (R_{el}), the neutralization reaction between H^+ and OH^+ (R_{neut}) , and the reaction between the conjugate acid-base pair in the buffer HPO_4^{2-} and $H_2PO_4^-$ (R_{buf}). The diffusion coefficients are D_{H^+} = 9.31×10^{-9} m^2/s, D_{OH^-} = 5.32×10^{-9} m^2/s, $D_{HPO_4^{2-}}$ = 0.759×10^{-9} m^2/s, $D_{H_2PO_4^-}$ = 0.959×10^{-9} m^2/s [19].

Generation of ions H^+ and OH^- (R_{el}) takes place at the anode ($R_{H^+,1}$) and cathode ($R_{OH^-,1}$) during each pulse (*Eqn. 2*), assuming a homogeneous profile over the surface of the electrodes[20].

$$R_{el} = R_{OH^-,1} = R_{H^+,1} = \frac{i}{nFV} \qquad \textit{Eqn 2}$$

where i is the current (~34 μA as observed in our experiments), n is the number of electrons involved in the reaction, and V is the volume.

Neutralization reaction occurs when protons meet hydroxides.

$$H^+ + OH^- \underset{k_2}{\overset{k_1}{\leftrightarrow}} H_2O$$

$$R_{neut} = R_{H^+,2} = R_{OH^-,2} = -k_1\,[H]\,[OH] + k_2 \times 55.65 \qquad \textit{Eqn 3}$$

We consider one equilibrium between HPO_4^{2-} and $H_2PO_4^-$.

$$HPO_4^{2-} + H^+ \underset{k_4}{\overset{k_3}{\leftrightarrow}} H_2PO_4^-$$

$$R_{buf} = R_{H^+,3} = R_{HPO_4^{2-},3} = -R_{H_2PO_4^-,3} = -k_3\,[HPO_4^{2-}]\,[H^+] + k_4[H_2PO_4^-] \qquad \textit{Eqn 4}$$

2.3 RESULTS AND DISCUSSION

The microfluidic device used in our study is shown in Fig. 2.1 and Fig.2.2A. Cells (typically 10-150) were loaded into a microfluidic chamber of 1.5mm×400μm×13μm. These cells were sealed inside the chamber by closing the pneumatic valves at the two ends. Two long planar gold electrodes (120 μm wide, and 1mm apart) were inside the chamber and 30-ms-long dc pulses were applied via these electrodes every 10 sec for 50 times with the pulse intensity in the range of 400-1800V/cm. CHO cells were initially tested. Interestingly, under unidirectional pulses, the cells did not move in a consistent direction. The cells eventually focused into a narrow region around the center of the chamber (Fig. 2.2B). Such movement could be tracked by both phase contrast imaging and fluorescence imaging (after labeling the cells with Hoechst 33342 which penetrates the cell membrane and intercalates within their DNA). In general, the focusing of the cells became more rapid when higher field intensity pulse was used (in the range of 400-1800 V/cm). The cells finished focusing after 50 pulses under 1000 V/cm while the same process essentially was completed after 10 pulses of 1800 V/cm. Fig. 2.2C reveals that in general, high pulse intensity also

led to improved focusing. For example, a 1000 V/cm or higher field intensity was required for complete focusing of cells within a ~30 μm-wide region.

Next, we analyze the mechanistic details involved in such isoelectric focusing of mammalian cells. The use of a closed microscale chamber in our design amplified the impact of electrochemical lysis of water. Hydroxides were generated at the cathode (the negative terminal) and protons were produced at the anode (the positive terminal) under sufficiently high voltage. Thus during the course of electropulsation, the local pH at the cathode became basic while the pH close to the anode turned acidic. The generation of a pH gradient under this mechanism was a significant process given the tiny volume of the microfluidic chamber. We conducted COMSOL modeling to examine the electrochemical process. A couple of simplifications needed to be made in order for the modeling to converge. First, we neglected the electrophoresis of ions. We will discuss the implications of this simplification below. Second, we considered only two important reactions (neutralization between H^+ and OH^- and conversion between the anions in the buffer $H_2PO_4^-$ and HPO_4^{2-}). The other reactions associated with phosphoric acid and phosphate anion are only important in extreme pH (<3 or >12, respectively), thus have smaller impact on the buffering.

We modeled three buffer concentrations under the application of 50 pulses (each with a 30 ms duration and 1000 V/cm intensity): 1. $[HPO_4^{2-}]=0$, $[H_2PO_4^-]=0$ (Fig. 2.3A); 2. $[HPO_4^{2-}]= 4.8$ mM, $[H_2PO_4^-]=1.2$ mM (Fig. 2.3B); 3. $[HPO_4^{2-}]= 9.6$ mM, $[H_2PO_4^-]=2.4$ mM (Fig. 2.3C). As presented in the inset graphs of Fig. 2.3A, 2.3B and 2.3C, after the first pulse (with the onset at t=0 and a duration of 30 ms) at t= 0.04s, hydroxides and protons are generated at the locations of the electrodes inside the chamber. These ions then diffuse during the interval between the first and second pulse (9.97s) into the rest of the chamber volume, forming a sharp pH gradient close to the center of the chamber. Such pH gradient continues to increase with the application of first several

additional pulses. In all three cases, the pH profile reaches its steady state after roughly the first 10 cycles (with one cycle referring to one 30 ms pulse followed by 9.97 s interval). After reaching the steady state, the pH profile still experiences the dynamics caused by the production of protons and hydroxides by additional pulses. However, the pH profile at the end of each additional cycle is identical. With increasing buffer concentrations, the pH profile in the chamber shows more resistance to pulse-induced pH change. Furthermore, the buffer in general has more buffering power in the acidic region (the right side of the chamber) than in basic region (the left side of the chamber) due to the higher starting concentration for HPO_4^{2-} (4 times higher than that of $H_2PO_4^-$).

Electrophoresis of ions affects the pH profile. The electrophoresis of protons and hydroxides only has minor impact on the location of the neutral pH interface in the middle of the chamber. On the other hand, the electrophoresis of HPO_4^{2-} and $H_2PO_4^-$ may have more significant influence on the pH profile. The majority of these anions is swept to the right side of the chamber after the first 4 cycles by electrophoresis and stay there for the rest of the process, as shown in Fig. 2.4. Thus, after the first 4 cycles, the buffering effect is primarily present on the right side of the chamber (with roughly doubled buffer concentration) while the left side of the chamber has few buffering ions.

To summarize, the actual pH profiles in the chamber over the course of the 50 cycles are best described by mixing the results under various buffer concentrations shown in Fig. 2.3. For a buffer with the concentration of $[HPO_4^{2-}]$ = 4.8 mM and $[H_2PO_4^-]$=1.2 mM (which was used in most of our experiments), the pH profiles are similar to the ones in Fig. 2.3B for the first 4 cycles. Then for cycles 5 to 50, the left side of the pH profiles will be similar to those in Fig. 2.3A and the right side will be similar to those of Fig. 2.3C. The pH gradient forms in the chamber in spite of the presence of the buffer. The buffer provides some resistance to the pH change within the initial

10 cycles, with such buffering effect more pronounced on the right side than on the left side. The location of cell focusing observed experimentally (at x=~750 μm, as shown in Fig. 2.2B) matches the location of the steep pH gradient suggested by the modeling when the buffer is considered (Fig. 2.3B and 2.3C).

Based on the data generated by the modeling, we estimate that a pH gradient of 0.07 Unit/μm was formed after the first pulse and it reached and stabilized at ~0.14 Unit/μm after the 10th pulse (Fig. 2.3B) at a location around the center of the chamber. Such a pH gradient was roughly 2 orders of magnitude steeper than that in the typical protein IEF setting (between 0.001 and 0.2 unit per 100 μm[5, 21-23]). The anode pH decreased from 7.4 to 3.8 after the first pulse and further to 2.0 after the 10^{th} pulse. Similar trend was observed at the cathode where the pH became 11.6 after the first pulse, and increased to 12.2 after the 10^{th} pulse. At the steady state (after 10^{th} pulse), a pH range of 3.8 to 10.5 was covered in a narrow 50 μm distance along x.

The establishment and dynamics of the pH gradient could be observed experimentally by having fluorescein dissolved in the buffer. Fluorescein is pH-sensitive and its fluorescence reduces significantly in acidic environments (e.g. the fluorescence intensity of fluorescein decreases by about 70% as the pH changes from 10 to 5, due to its protonation[24]). Fig. 2.5 shows that the fluorescence on the right side of the chamber (close to the anode) started to disappear with the application of the pulses. The boundary (between the dark and fluorescent areas) continued to recede to the left as more pulses were applied. The boundary eventually stabilized after ~15 pulses at a location on the left side to the center of the chamber. Electrophoresis of the negatively charged fluorescein (with a mobility of -10 to -25 × 10^{-9} m^2V^{-1} s^{-1} [25]) did not affect the location of the fluorescence boundary because electrophoresis moved these molecules to the right side of the chamber (which was acidic and effectively quenched the fluorescence). In addition, there might

also be contribution from electrochemical processes that caused fluorescence quenching at the right side of the chamber (e.g. Kolbe electrolysis on the anode[26]). Thus the shift of the fluorescence boundary to the left end of the chamber roughly reflected the dynamic change in the pH inside the chamber. We found that having the interval (between pulses) at 9.97s was necessary to allow enough time for gas bubbles generated at the electrodes to dissipate through PDMS[17]. When the interval was much shorter (e.g. 0.97s, as in Fig.2.6), there was instability in the boundary, presumably due to the accumulated bubbles on the electrodes. Thus we used 9.97s intervals for all other experiments that applied consecutive pulses.

Close observation reveals that the cell movement had close correlation to its location relative to that of the fluorescein boundary which roughly separated the acidic and basic regions. In Fig. 2.6, we show the movement of both the fluorescein boundary (by having fluorescein in the buffer) and the cells during the first 10 pulses. At the beginning of the process, and before the first pulse, the solution had a slightly basic pH (7.4). Thus initially all cells were negatively charged and moved toward the anode (in the reverse direction of the applied field). However, after the first 2 pulses a significant region close to the anode turned acidic (indicated by the loss of fluorescein fluorescence). This led to a change in the moving direction for these cells, causing them to move towards the cathode. It is worth noting that cells stabilized when they crossed 10-20 μm over the fluorescein boundary line to the right, indicating that the neutralization in the cell surface charge occurred under a low pH. For the cells which were at the far left of the boundary line, they experienced only movement toward the right (anode) due to the fact that they were always under the basic pH. The effect of electroosmotic flow in here can be ignored as the chamber was closed during the process.

It is interesting to track the dynamics in the electrophoretic mobility of a cell under the pulse sequence and the local pH at the moment. The pH varied with the location inside the chamber and the number of pulses that have been exerted. We calculated the local pH values for cells at a particular moment based on our COMSOL modeling and tracked the corresponding velocity, and therefore the electrophoretic mobility, based on the videometric data. Fig. 2.7 shows that the local pH strongly affected both the direction and magnitude of the electrophoretic mobility. First of all, all cells moved from the cathode to the anode (shown with negative sign) when pH was higher than 6.5 (with an average μ of -19.86 $mm^2/(kV•sec)$ and a standard deviation of 8.01 $mm^2/(kV•sec)$), whereas the vast majority of the mobilities were positive when the pH was lower than 4.5 (the average value of μ was 1.68 $mm^2/(kV•sec)$ and the standard deviation was 4.20 $mm^2/(kV•sec)$). This confirms that cells were negatively charged at high pH and positively charged at low pH with a threshold range of pH 4.5-6.5 separating the two regimes. This fairly wide range for pI may be related to the heterogeneity in the cell population. Other than pH, mechanisms such as cell polarization in the electric field may also have effect on the distribution of the cell surface charge and the electrophoretic mobility[27].

We also tested various buffer concentrations (2.4 mM Na_2HPO_4-0.6 mM KH_2PO_4, 4.8 mM Na_2HPO_4-1.2 mM KH_2PO_4, and 8 mM Na_2HPO_4-2 mM KH_2PO_4) experimentally (Fig. 2.8). The results indicate that the mobility of cells was not significantly affected by the buffer concentration in this range. This confirms that the buffering power of the solution was not enough to counteract the generation of protons and hydroxides by the electrochemical reactions.

Our device and setup allow IEF of mammalian cells of various types and various concentrations (we show IEF of Jurkat cells at high and low concentrations in Fig. 2.9), owing to the ultrahigh pH gradient formed and the free solution arrangement. The focusing process involves

a complex interplay among the spatiotemporally varying parameters of local pH, cell surface charge, and cell electrophoretic mobility (shown in the schematic of Fig. 2.10). It is also worth noting that electroporation of cells may occur when the field intensity was higher than a threshold of 300-400 V/cm[28, 29].

2.4 CONCLUSION

To summarize, we demonstrate the IEF of mammalian cells in a microfluidic chamber by creating an ultrahigh pH gradient in free solution via electrolysis of water. The use of a closed chamber facilitates formation of significant pH gradient based on microscale electrochemical reactions and also eliminates potential undesired flow (e.g. electroosmotic flow) which is detrimental to pH gradient establishment. The free solution scheme allows the easy movement of cells. The focusing of cells requires high field intensities for the dc pulses, because of the relative low mobility of cells due to pH-induced surface charge. The ultrahigh and nonlinear pH gradient close to the center of the chamber permitted focusing of cells with minor difference in their pI. Our approach works universally for different mammalian cell types and concentrations.

REFERENCES

1. L. H. Silvertand, J. S. Torano, W. P. van Bennekom and G. J. de Jong, *J Chromatogr A*, 2008, **1204**, 157-170.
2. K. Shimura, *Electrophoresis*, 2009, **30**, 11-28.
3. J. Salplachta, A. Kubesova and M. Horka, *Proteomics*, 2012, **12**, 2927-2936.
4. S. Hjerten, K. Elenbring, F. Kilar, J. L. Liao, A. J. Chen, C. J. Siebert and M. D. Zhu, *Journal of Chromatography*, 1987, **403**, 47-61.
5. U. Schnabel, F. Groiss, D. Blaas and E. Kenndler, *Analytical Chemistry*, 1996, **68**, 4300-4303.
6. D. W. Armstrong, G. Schulte, J. M. Schneiderheinze and D. J. Westenberg, *Anal Chem*, 1999, **71**, 5465-5469.
7. M. Horka, J. Planeta, F. Ruzicka and K. Slais, *Electrophoresis*, 2003, **24**, 1383-1390.
8. Y. Shen, S. J. Berger and R. D. Smith, *Analytical Chemistry*, 2000, **72**, 4603-4607.
9. B. Alberts, *Molecular biology of the cell*, Garland Science, New York, 2002.
10. A. Varki, R. D. Cummings, J. D. Esko, H. H. Freeze, P. Stanley, C. R. Bertozzi and G. W. Hart, *Essentials of Glycobiology*, Cold Spring Harbor Laboratory Press, Cold Spring Harbor, NY, 2009.
11. G. M. Cook, *Biol Rev Camb Philos Soc*, 1968, **43**, 363-391.
12. T. Angata and A. Varki, *Chem Rev*, 2002, **102**, 439-469.
13. J. El-Ali, P. K. Sorger and K. F. Jensen, *Nature*, 2006, **442**, 403-411.
14. N. Agrawal, Y. A. Hassan and V. M. Ugaz, *Angew Chem Int Edit*, 2007, **46**, 4316-4319.

15. P. G. Schiro, M. X. Zhao, J. S. Kuo, K. M. Koehler, D. E. Sabath and D. T. Chiu, *Angew Chem Int Edit*, 2012, **51**, 4618-4622.

16. C. D. K. Sloan, P. Nandi, T. H. Linz, J. V. Aldrich, K. L. Audus and S. M. Lunte, *Annu Rev Anal Chem*, 2012, **5**, 505-531.

17. T. Geng, N. Bao, N. Sriranganathanw, L. Li and C. Lu, *Analytical Chemistry*, 2012, **84**, 9632-9639.

18. J. Schindelin, I. Arganda-Carreras, E. Frise, V. Kaynig, M. Longair, T. Pietzsch, S. Preibisch, C. Rueden, S. Saalfeld, B. Schmid, J. Y. Tinevez, D. J. White, V. Hartenstein, K. Eliceiri, P. Tomancak and A. Cardona, *Nature Methods*, 2012, **9**, 676-682.

19. W. M. Haynes, *CRC Handbook of Chemistry and Physics*, Taylor and Francis Group, 2010.

20. D. Di Carlo, C. Ionescu-Zanetti, Y. Zhang, P. Hung and L. P. Lee, *Lab on a Chip*, 2005, **5**, 171-178.

21. L. Goodridge, C. Goodridge, J. Wu, M. Griffiths and J. Pawliszyn, *Analytical Chemistry*, 2003, **76**, 48-52.

22. M. Horká, F. Růžička, A. Kubesová, V. Holá and K. Šlais, *Analytical Chemistry*, 2009, **81**, 3997-4004.

23. M. Horká, F. Růžička, V. Holá, V. Kahle, D. Moravcová and K. Šlais, *Analytical Chemistry*, 2009, **81**, 6897-6904.

24. M. M. Martin and L. Lindqvist, *Journal of Luminescence*, 1975, **10**, 381-390.

25. D. Milanova, R. D. Chambers, S. S. Bahga and J. G. Santiago, *Electrophoresis*, 2011, **32**, 3286-3294.

26. A. K. Vijh and B. E. Conway, *Chem Rev*, 1967, **67**, 623-664.

27. E. Prodan, C. Prodan and J. H. Miller, *Biophys J*, 2008, **95**, 4174-4182.

28. H. Y. Wang and C. Lu, *Analytical Chemistry*, 2006, **78**, 5158-5164.

29. N. Bao, J. Wang and C. Lu, *Electrophoresis*, 2008, **29**, 2939-2944.

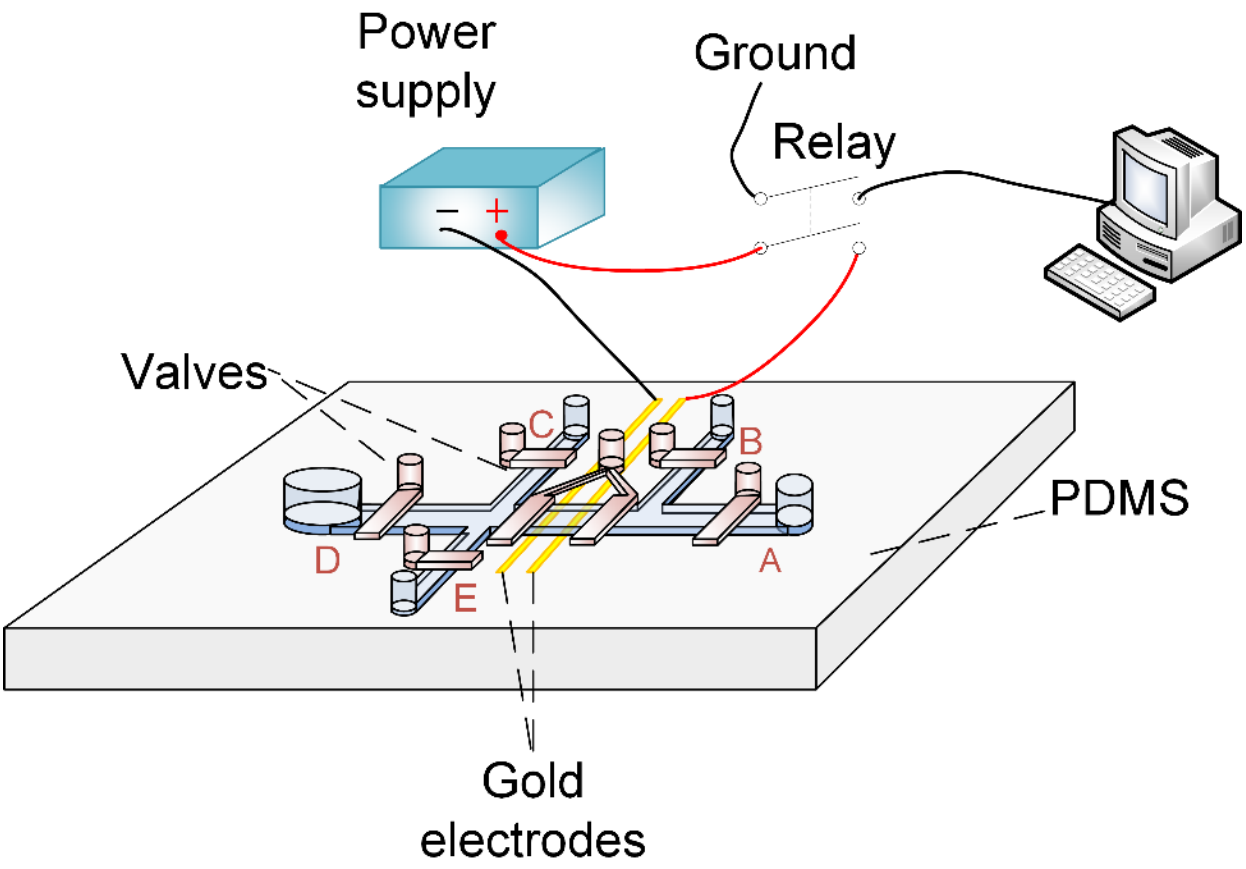

Figure 2.1. The design and setup of the entire microfluidic chip for cell focusing. The microfluidic device is made of PDMS and consists of two layers (fluidic layer in blue and control layer in pink). The fluidic layer has 3 inlets (A, B, C) and 2 outlets (D, E). All these ports can be closed by the microvalves that are adjacent to them. By selective closing of valves, the cells initially flow into the device from inlet B to outlet E. After the microfluidic chamber is populated with cells, the two valves close to the electrodes close to seal the chamber. Then buffer flows from E to C, and from A to B, to flush out the cells that are not in the electropulsation chamber. All the valves are closed during electropulsation. Two surface gold electrodes are in the electropulsation chamber, and connected to a circuit including a dc power supply and a relay. A computer is used to control the frequency and the duration of the pulses.

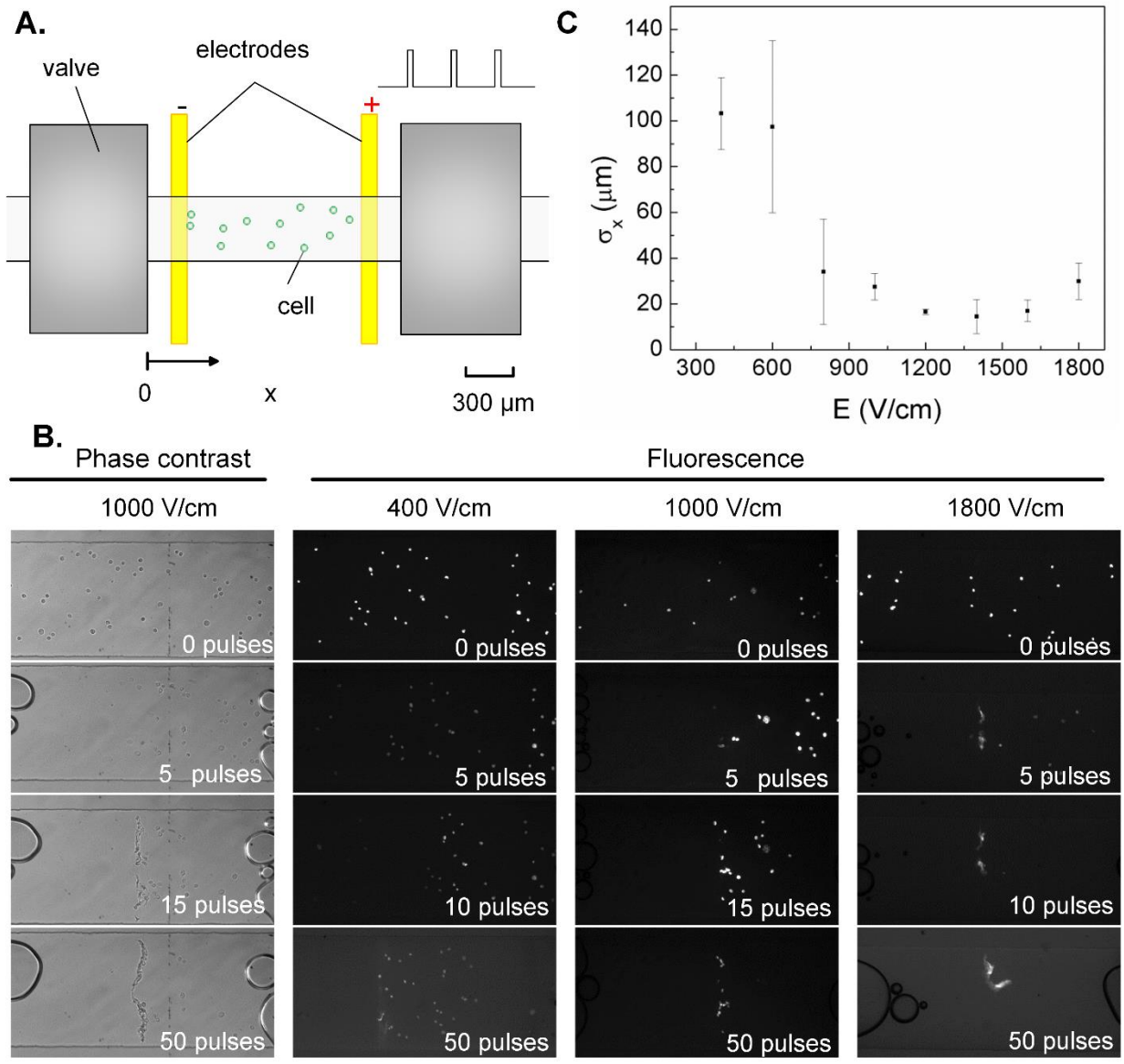

Figure 2.2. The focusing of cells in a closed microfluidic chamber under unidirectional electropulsation**.** (A) The design of the closed microfluidic chamber. The microfluidic chamber (1.5mm×400μm×13μm) was confined by two pneumatically actuated valves during electropulsation. Square pulses were applied to the system via two surface gold electrodes. (B) Time-lapse images of CHO-K1 cell focusing under 50 pulses of various field intensities (400,

1000, and 1800 V/cm). Each pulse was 30 ms in duration and rectangular and occurred at the beginning of a 10s duration (i.e. the interval between pulses was 9.97 s). In the fluorescent images, the cells were stained by Hoechst 33342. A buffer system containing 4.8 mM Na_2HPO_4, 1.2 mM KH_2PO_4, and 250 mM sucrose was used. (C) The effect of the field intensity E of the pulses on the standard deviation in the cell locations along X axis after 50 pulses.

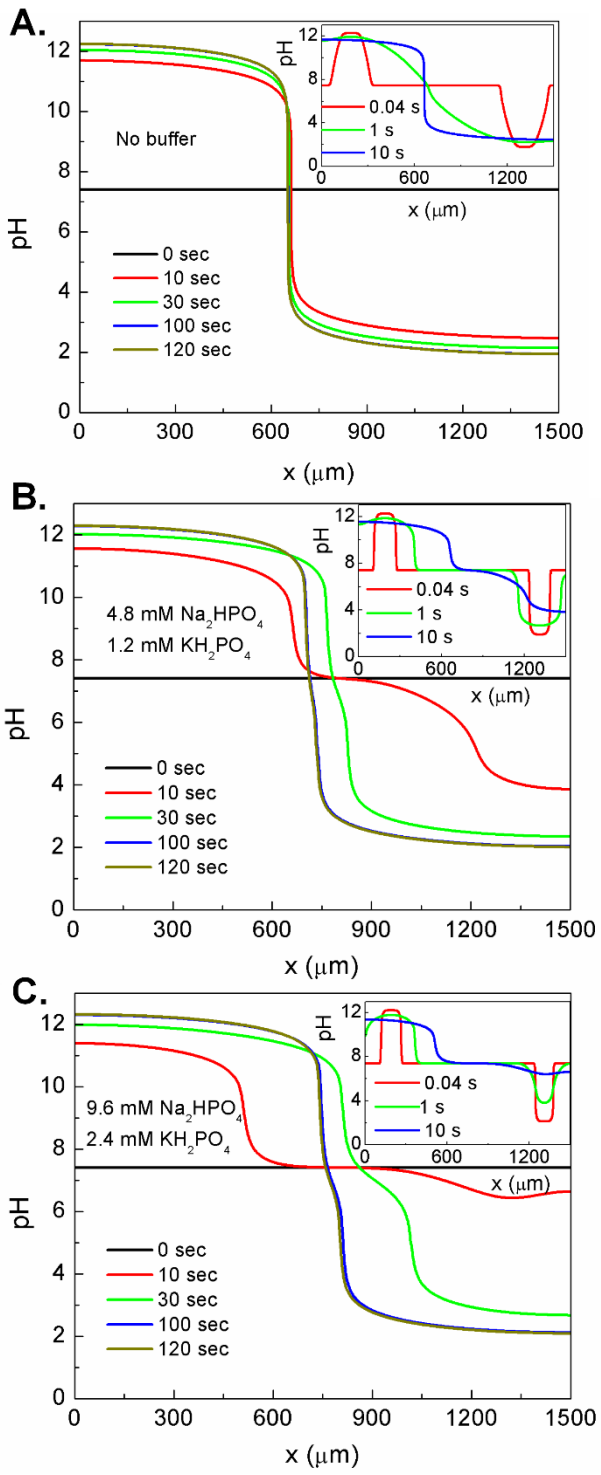
A.
No buffer
0 sec
10 sec
30 sec
100 sec
120 sec
0.04 s
1 s
10 s
pH
x (μm)
B.
4.8 mM Na2HPO4
1.2 mM KH2PO4
C.
9.6 mM Na2HPO4
2.4 mM KH2PO4

Figure 2.3. The formation of pH gradient due to water electrolysis. The pH profiles along the length of the microfluidic chamber (x axis) at multiple time points are computed by COMSOL Multiphysics for three buffer concentrations (A) no buffer, (B) 4.8 mM Na_2HPO_4, 1.2 mM KH_2PO_4, and (C) 9.6 mM Na_2HPO_4, 2.4 mM KH_2PO_4. The cathode is located at x=130-250 μm, the anode is located at x=1250-1370 μm, and both electrodes are 120 μm wide. The pulses are applied once every 10 s and last for the first 30 ms of each 10 s cycle (e.g. in the first cycle, the pulse lasts during t = 0-0.03 s). The insets show the pH profile change during the first cycle (t = 0-10 s).

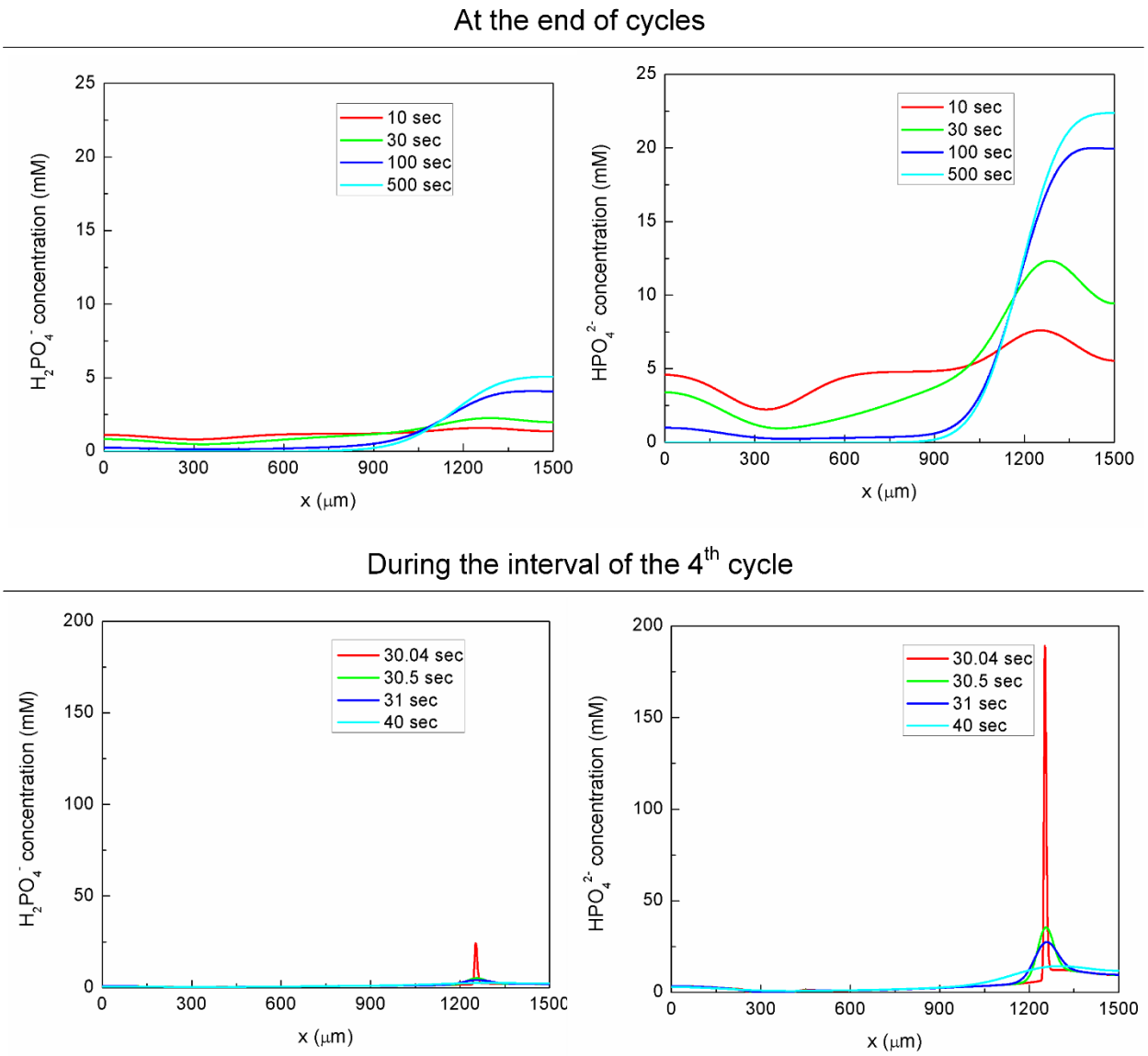

Figure 2.4. The modeled concentration profiles of $H_2PO_4^-$ and HPO_4^{2-} during the process of electropulsation. To simplify the modeling, we consider only electrophoresis and diffusion of the ions in the buffer (Na^+, K^+, $H_2PO_4^-$ and HPO_4^{2-}) for the solution containing 4.8 mM Na_2HPO_4, 1.2 mM KH_2PO_4 without involving the proton and hydroxide production. The pulses (1000 V/cm) are applied once every 10 s and last for the first 30 ms of each 10 s cycle. The cathode is located at

x=130-250 μm, the anode is located at x=1250-1370 μm, and both electrodes are 120 μm wide. At the end of the 4th cycle, 71% of $H_2PO_4^-$ and 83% of HPO_4^{2-} are at the proximity of the anode (within a 300 μm distance along x).

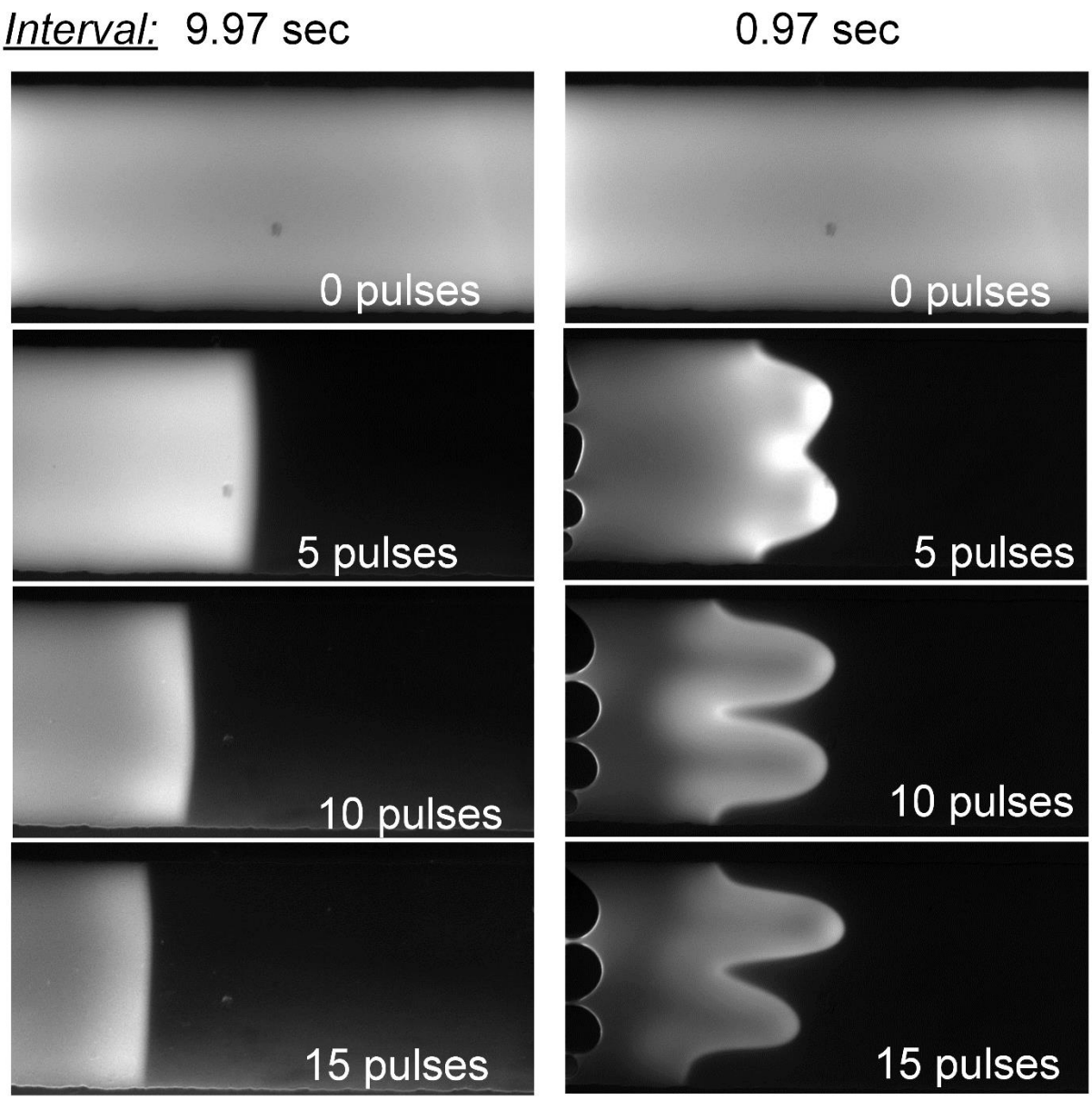

Figure 2.5. Time-lapse images of the buffer (4.8 mM Na_2HPO_4, 1.2 mM KH_2PO_4, and 250 mM sucrose) containing fluorescein during electropulsation (50 pulses of 30 ms duration and 1000 V/cm intensity). The left panel was taken when the interval was 9.97 s between pulses and the right panel had intervals of 0.97s.

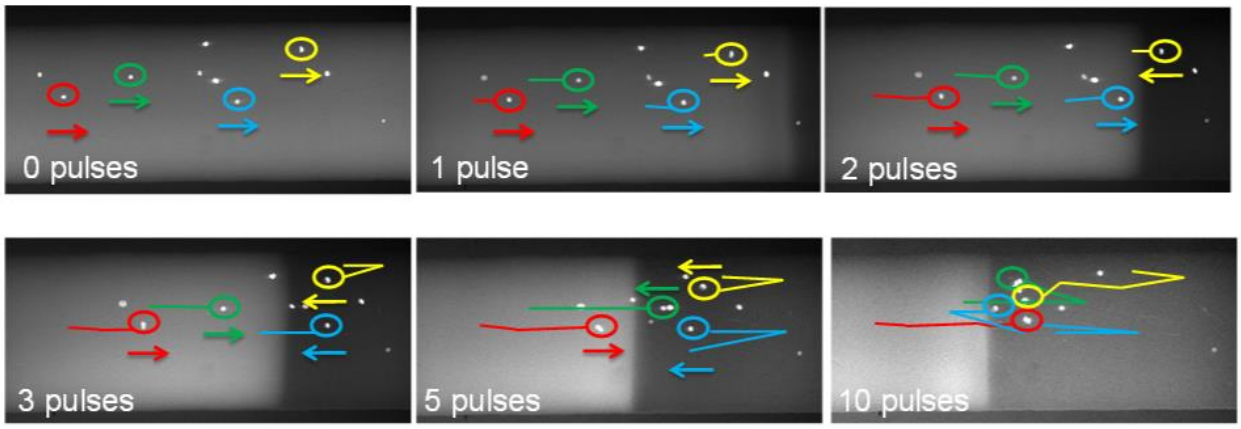

Figure 2.6. Time-lapse images that show the movement of cells inside the chamber in relation to the boundary formed by fluorescein. The cells were stained by Hoechst 33342 and suspended in the buffer containing fluorescein. A buffer system containing 4.8 mM Na_2HPO_4, 1.2 mM KH_2PO_4, and 250 mM sucrose was used. The pulses (1000 V/cm) were applied once every 10 s and lasted for the first 30 ms of each 10 s cycle.

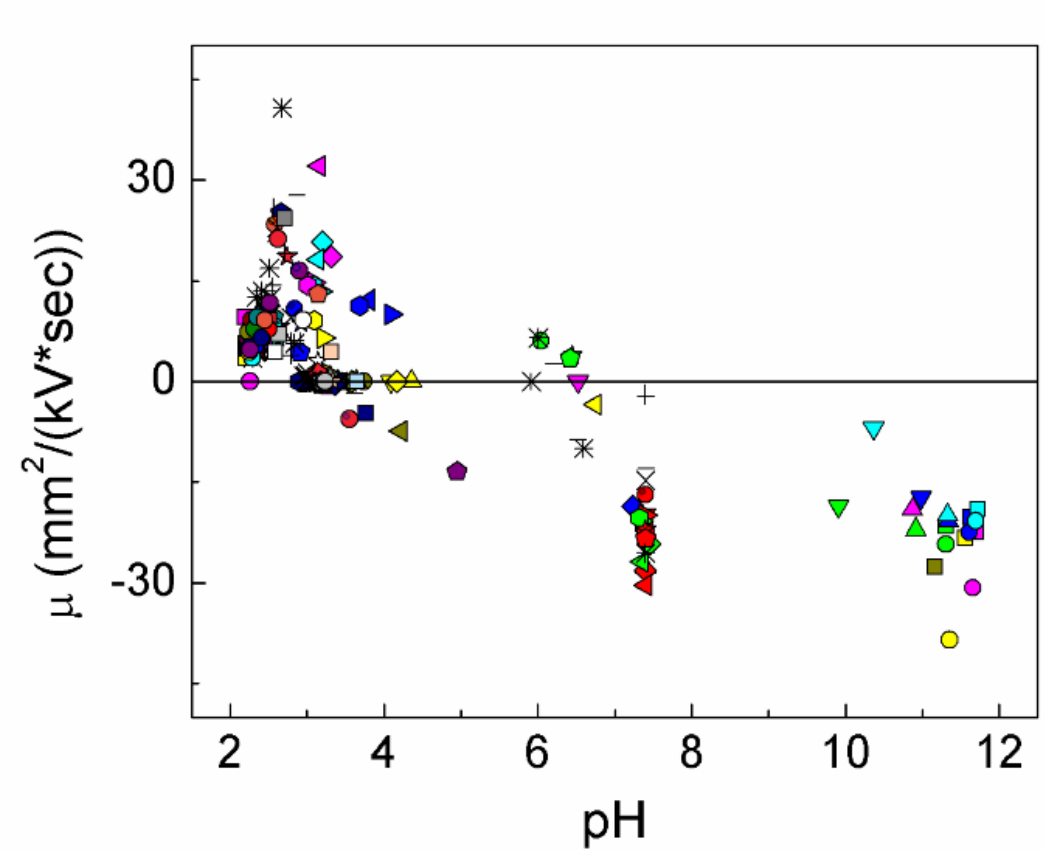

Figure 2.7. The effect of the local pH on the electrophoretic mobility of a cell during a pulse. The pH of the solution at various time points and physical locations (inside the chamber) was determined using COMSOL Multiphysics. The electrophoretic mobility of cells was calculated after measuring the velocity of cells (i.e. the distance it traveled during the pulse divided by the pulse duration) under an specific field intensity (i.e. 1000 V/cm). Each individual cell is represented by a specific type of markers. The pulses were applied once every 10 s and lasted for the first 30 ms of each 10 s cycle. A buffer system containing 4.8 mM Na_2HPO_4, 1.2 mM KH_2PO_4, and 250 mM sucrose was used.

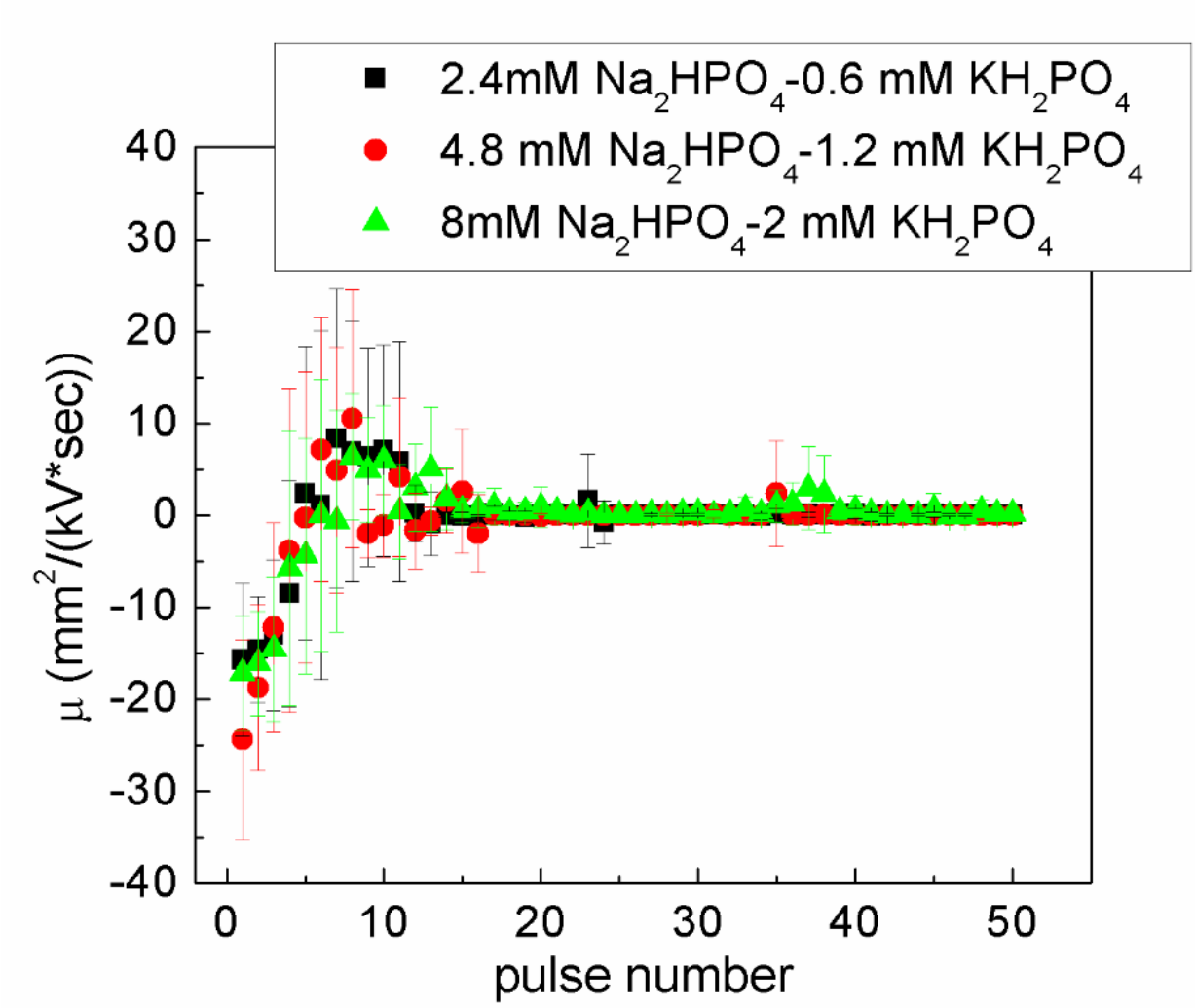

Figure 2.8. The average mobility of cells during each pulse for experiments performed in buffers of various ion concentrations. Three different buffers containing 2.4 mM Na_2HPO_4-0.6 mM KH_2PO_4, 4.8 mM Na_2HPO_4-1.2 mM KH_2PO_4, and 8 mM Na_2HPO_4-2 mM KH_2PO_4, supplemented with 250 mM sucrose in all cases, were tested. The electropulsation was conducted by applying 50 pulses with 1000 V/cm intensity, 30 ms duration, and 9.97 s intervals.

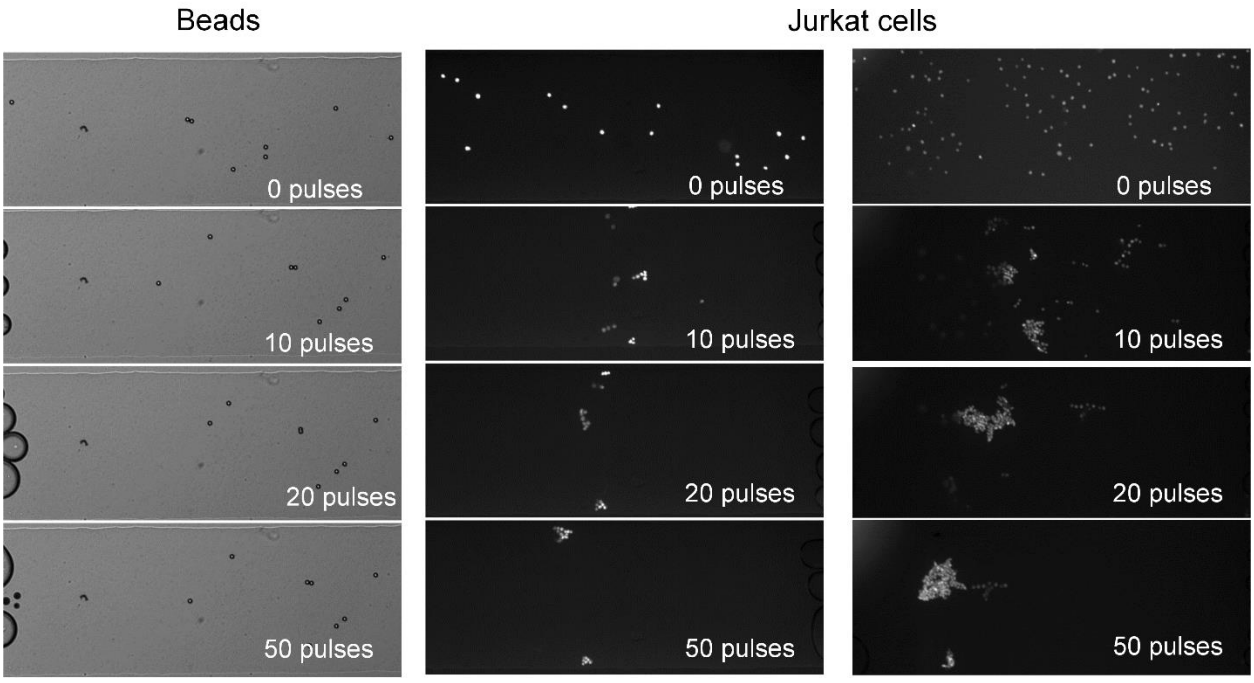

Figure 2.9. Time-lapse images during the application of 50 pulses of 1000 V/cm, 30 ms duration and 9.97 s intervals of polymeric beads (d~10 µm, left panel) and Jurkat cells. Jurkat cells of two different concentrations (middle and right panels) were tested. The cells and the beads were suspended in a phosphate buffer (4.8 mM Na_2HPO_4, 1.2 mM KH_2PO_4, and 250 mM sucrose). The polymeric beads did not focus under these conditions.

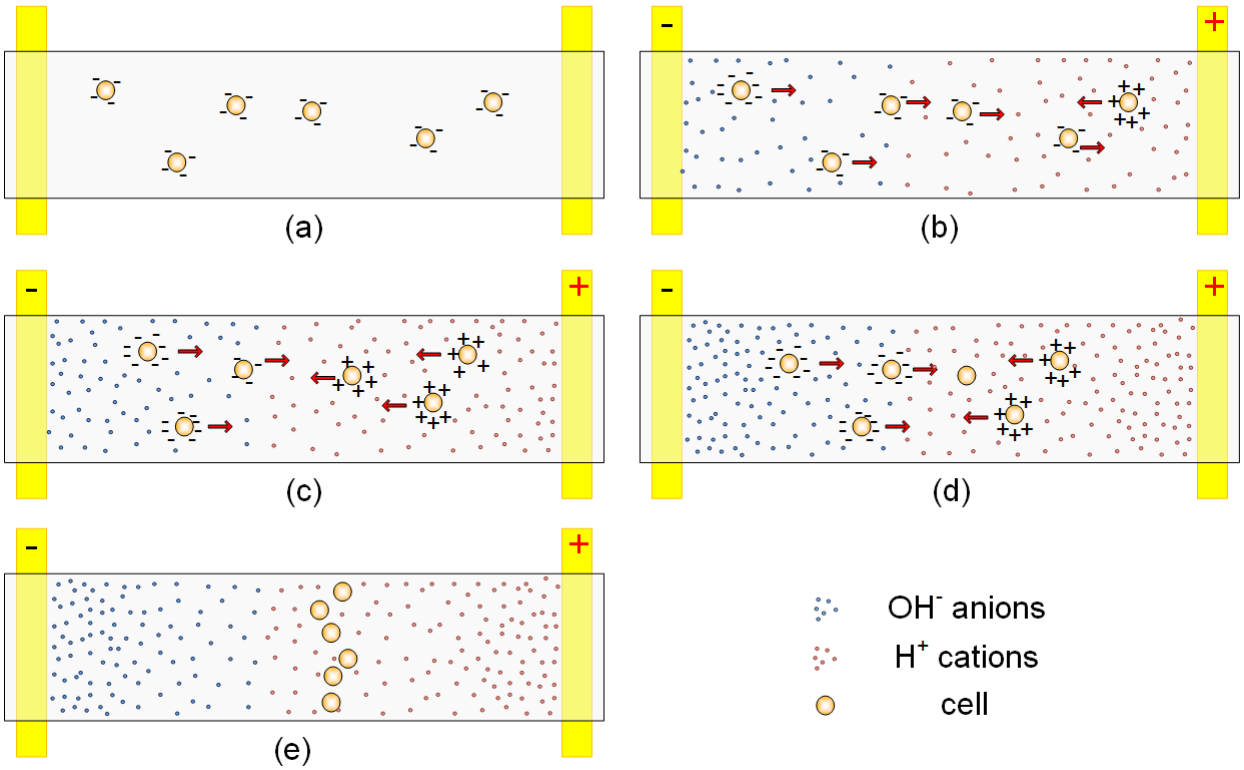

Figure 2.10. Proposed mechanism for IEF of mammalian cells in free solution. (a) Before the first pulse, cells naturally possess a negative surface charge in the pH 7.4 buffer. (b) The first pulse takes place and protons and hydroxides are generated at the electrodes. A pH gradient starts to form, and the acidic environment close to the anode renders some cells positively charged. Cells move in both directions depending on their locations. (c) The pH gradient becomes higher with additional pulses. There is a larger region that turns cells positively charged. There is reversal in the moving direction for certain cells. (d) The pH gradient becomes stable and does not change with additional pulses. Cells continue to move to their equilibrium positions. (d) All the cells are focused at the location where the pH is equal to cell pI and they have a neutral surface charge and stop moving.

CHAPTER 3 – ELECTRICAL LYSIS OF MAMMALIAN CELLS FOLLOWED BY ON-CHIP-PCR OF THE EXTRACTED GENOMIC DNA

3.1 INTRODUCTION

3.1.1 INTRODUCTION TO CELL LYSIS

Cell lysis, i.e. the rupture of the cell membrane, is a vital step for many biological applications. It is necessary in order to release the intracellular material, such as proteins, nucleic acids or organelles. Subcellular release is almost always followed by a separation and purification step in order to collect the molecules of interest and proceed to downward analysis. Depending on the molecule of interest and its characteristics, such analyses may include immunoprecipitation and western blot for the detection of a protein, DNA / RNA hybridization and amplification for genetic analysis, or centrifugation for organelle purification.

Several methods have been demonstrated to efficiently break the lipid bilayer that surrounds and protects the intracellular ingredients. An additional difficulty is encountered in the studies where the organellar membranes need to be intact after cell rupture. The speed of cell lysis is also important, in order to prevent further biochemical changes such as protein degradation, or nucleic acids fragmentation. The particular method to be used in every case is selected based on the downward application.

3.1.1.1 MICROFLUIDIC DEVICES FOR CELL LYSIS

The biological process of cell lysis has effectively been miniaturized to lab-on-a-chip devices. Conventional methods have been scaled-down to be applied on a microfluidic platform [1, 2]. The set of characteristics of microfluidics has also led to the development of new ways for cell membrane rupture. Methods for multiple and single cells have been shown and can be categorized to four groups: chemical, mechanical, thermal and electrical.

The simplest and most common one is chemical lysis, which uses lytic agents or lysis buffers that contain surfactants and solubilize the lipid membranes[2]. The drawback of this method is the necessity of a purification step; because the buffer interferes with downward applications (e.g. SDS inhibits PCR). This problem is usually overcome by off chip purification using DNA extraction buffers, degradation, centrifugation and filtration. Several studies have shown the application of such methods on chip. In a recent study, single cells were trapped in a microwell array and were subsequently chemically lysed with a conventional lysis buffer[1].

The implementation of different lytic agents has also been studied in microfluidic devices. Palladium electrodes were integrated on chip to induce hydroxide generation during hydrolysis[3]. The alkaline solution led to irreversible membrane poration, and cell lysis. In another work osmotic shock was used in order to lyse red blood cells[4]. The researchers took advantage of the laminar regime and used hydrodynamic focusing, during which the ion concentration of the cell suspension changed, only due to ion diffusion between adjacent fluidic layers.

Mechanical lysis is applied on microfluidic devices by producing shear and frictional forces to tear the cell membrane. Beads have been introduced in cell suspensions to granulate the cells and free the intracellular components[5]. This method is ideal for cells with thick walls that are harder to lyse. Sharp nanobarbs have also been fabricated on a chip, in an attempt for reagent free

lysis[6]. The features on the device remind nano-knives that break the cell membrane at several points and eventually cut them open. Another study uses mechanical microfluidic valves in order to crush the cells. During this work the cells are squeezed and flattened because of a high pressure that eventually bursts them[7].

Increased temperature has been used to denature the proteins on the cell membrane and damage it leading to the release of the subcellular content. Several heating features have been integrated on a device, the most common ones being resistive heaters[8]. Alternating magnetic field has also been used to wirelessly increase the temperature of a metal heating unit integrated in a microchamber[9]. Recently, mammalian cells were shown to be electrically heated for subsequent RT-PCR amplification[10].

Electrical lysis has also been reported at cell disruption experiments. Typically, when cells are exposed to an electric field, pores are generated on the cell membrane. If the field is too high, irreversible pore formation takes place, and as a result a permanent damage followed by the release of the intracellular content. Alternating current (AC) electric field has shown to effectively lyse cells using embedded gold electrodes[11]. Direct current (DC) pulses were shown to lyse bacterial cells[12] and recently they were used to extract DNA from mammalian cells[13]. An advantage of electrical lysis methods is the capability of damaging only the outer membrane of the cell without breaking other organellar membranes (e.g. nucleus)[14]. The majority of these reports use optical methods to detect the cell lysis. Alternatively, they perform DNA purification and off chip PCR amplification of the extracted genomic material. To our knowledge, the immediate on chip amplification of the cell lysate, after electrical lysis, does not exist yet.

3.1.2 Introduction to PCR

Polymerase chain reaction (PCR) is a method for in vitro nucleic acid amplification. The development of this method granted a Nobel Prize to its founder, Kary Mullis. In theory, even one copy of a gene is enough to create multiple copies with this method, and because of that, PCR has found wide applications in forensic investigations, ecology, and genetic analysis.

PCR is a method that mimics the DNA replication that takes place in all living cells. In vivo, initially the double helix of DNA unfolds at specific locations, and later, an enzyme, called polymerase, builds new double stranded DNAs, that are identical to the initial one, by addition of nucleotides (i.e. the building blocks of DNA) in a complementary –to the template- fashion. This is due to the preference of the nucleotides, or else dNTPs, to form hydrogen bonds with only their complementary pair[15]. Ex vivo, the first step is the denaturation of the double stranded DNA to two single strands, followed by the annealing of a set of short DNA sequences, the so-called primers, to the mother strands. During the next step, a thermostable polymerase catalyzes the extension of the daughter-strand. This procedure is repeated in cycles (typically 35-40 times) in order to create a sufficient amount of identical amplicons.

Just like any other reaction, the amplification of the gene of interest depends strongly on the reagents (i.e. the master mix, which includes the dNTPs and reaction buffers), the right concentration of the catalysts (i.e. the polymerase) and the temperature. The polymerase has an optimum temperature at which it can efficiently catalyze the reaction, and it also affected by the ion concentration in the buffer solution. Nowadays, the polymerases are mostly engineered, and are commercially available in their own buffer solution (master mix) for optimum activity. The fabrication of the right primers is vital in order to amplify the specific gene of interest. By the end

of the reaction, the majority of the DNA strands in the solution will be replications of the gene of interest.

There are three important temperature steps during PCR, which correspond to the denaturation of the DNA, the annealing of the primers, and the extension of the new strands. These steps altogether constitute a PCR cycle. The denaturation, or else melting, of the DNA requires a high temperature (typically 95^{o}C) to unwind the double stranded DNA to two single strands. The maximum temperature is limited by the temperature at which the degradation of the polymerase takes place. The second step of a PCR cycle, is the annealing of the primers with the template strands, and it only happens on primer-specific temperature (~50-70^{o}C). The third and final step is the extension of the DNA using the polymerase, the temperature of which is controlled by the polymerase (~65-80^{o}C). Commercially available heaters, named thermal cyclers, are used for this technique.

After the completion of the reaction, analysis of the PCR products follows to ensure the correct outcome of the experiment. A common way for examining the amplicons is using agarose gel electrophoresis, during which the DNA fragments travel through a gel matrix driven by electrophoretic force. The fragments are then separated based on their size, with the smaller ones moving a longer distance. A solution with fragments of known size, the so-called ladder, is used to compare the length of the products. A fluorescent dye binds within the nucleic acids for visualization in the gel. Another post-PCR detection analysis involves the use of homogeneous hybridization probes[16]. An increase in the fluorescence intensity is recorded only when the probe recombines with the PCR product.

3.1.2.1 Real-time PCR

A method that can provide high accuracy and real-time information is quantitative real-time PCR. During this method a fluorescent dye, which is introduced in the master mix, binds with the double stranded DNA and emits a fluorescent signal. This signal is proportional to the amount of the double stranded DNA in the sample. The fluorescence signal is recorded after each cycle, giving a precise measurement of the amount of amplicons.

RT-PCR is also applied to determine the initial amount of template DNA in a solution. A threshold cycle (C_t) is determined for each sample, which is the cycle at which a detectable increase in fluorescence is recorded, and it is strongly dependent on the initial amount of DNA. Comparison of the C_t with samples of known initial DNA concentration gives information for the sample with unknown concentration. A drawback of this method is that the amplicon length cannot exceed 250bp.

3.1.2.2 On-chip PCR

PCR amplification reactions have also been miniaturized and applied on microfluidic devices. Several different designs have been demonstrated, that can be categorized mainly by the method used to heat the solution at every step during each cycle. The use of a conventional flatbed thermal cycler is the most convenient way to achieve the temperature steps; however integrated heaters have also shown good results [17-19]. In the latter case the microdevices can perform a PCR reaction either in a stationary or a dynamic mode. During the operation of a stationary microchip the master mix is inserted in an amplification chamber, the temperature of which is controlled by heaters according to the cycling profile[20]. On the other hand, the architecture of a device that functions on a dynamic mode requires integrated steady temperature heaters along the surface. The

solution then flows continuously through the regions of the fixed temperature enabling the reaction[17].

The small volume that microfluidic devices support, allowed the decrease of the amount of template DNA. Single-molecule amplification has been demonstrated ensuring the presence of only one genome in each chamber using surface tension-based sample partitioning[18]. However, the small volume in addition to the high surface to volume ratio lead to increased evaporation through the PDMS device during thermal cycling resulting in concentration changes and unsuccessful reactions[17].

In order to keep the advantages of cheap, fast, and easy fabrication of the PDMS chips, several methods were proposed to overcome the problem of evaporation. Two phase mixture was introduced in the microchannel, with oil supporting and protecting a drop of master mix from evaporating[17]. In another study, a low permeability polymer was used to fabricate a barrier layer on top of the fluidic channel, where the PCR reaction took place[18]. A hydration layer was also shown to reduce the effect of vapor transport by increasing and fixing the vapor pressure around the master mix solution [18, 19, 21].

Different methods have also been demonstrated to detect the outcome of the reactions in the microchannel. End point detection has taken place using agarose gel electrophoresis off-chip[17], or capillary electrophoresis on an integrated channel on the device[20]. In case of arrays and small volume reactions, on chip detection has only been shown. Fluorescent molecules, either attached to probes or free, are introduced in the master mix, to enable the monitor of the progress of PCR after each cycle [18, 21].

3.2 MATERIALS AND METHODS

3.2.1 DEVICE OPERATION

A two layer microfluidic device was fabricated by multilayer soft lithography based on PDMS (Appendix A). The fluidic layer accommodates channels of different depths (13 μm, and 60 μm). The control layer holds the control chambers, and a hydration channel that is necessary during the on-chip PCR. The depth of the control channels is 28 μm. The 2-layer PDMS was bonded with 0.16 mm thick glass slide, supplemented with gold surface electrodes (Appendix A).

The device was mounted on an inverted fluorescence microscope (IX-71, Olympus, Melville, NY) equipped with a 2x and a 10x objective, and a CCD camera (ORCA-285, Hamamatsu, Bridgewater, NJ). The microfluidic chip was also connected to solenoid valves (ASCO Scientific, Florham Park, NJ), for pneumatic actuation of the control channel, and was controlled by a LabView program (National Instruments, Austin, TX) and a DAQ card (NI SCB-68, National Instruments, Austin, TX). The gold surface electrodes were connected to a custom electronic circuit and a DC power supply (PS350, Stanford Research Systems, Sunnyvale, CA) to provide reverse direction, electrical pulses to the system, which were controlled by a LabView program (National Instruments, Austin, TX).

3.2.2 DNA AND CELL SUSPENSION PREPARATION

Genomic DNA was extracted from CHO-K1 cells using the QIAmp DNA Blood Mini Kit (QIAGEN, Valencia, CA). CHO-K1 cell suspension was prepared in a low conductivity phosphate buffer (4.8 mM Na_2HPO_4, 1.2 mM KH_2PO_4, and 250 mM sucrose, pH=7.4), and at a concentration of $1x10^6$ cells/ml for the experiments (Appendix B).

3.2.3 PCR CONDITIONS

The PCR master mix was prepared by adding 1x Fast Plus EvaGreen qPCR Master Mix (Biotium, Hayward, CA), 0.8% PEG 8000 (Sigma Aldrich, St. Louis, MO), 0.08% Tween 20 (Sigma Aldrich, St. Louis, MO), 0.2U/μl Taq polymerase (Invitrogen, Grand Island, NY), 1.2mM NV1 primers (Integrated DNA Technologies Inc, Coralville, IA). The primers are CHO-K1 genome specific, and the amplified product is 110bp long (forward: ACAGGTTTCTGCTTCTGGCT, reverse: CATCAGCTGACTGGTTCACA)[22]. The cycling parameters were: 95°C for 2 minutes, and then 40 cycles of 95°C for 1 minute, 60°C for 30 seconds, 72°C for 35 seconds.

3.3 RESULTS AND DISCUSSION

The 2-layer microfluidic device shown in figure 3.1 was used for the experiments of this project. CHO-K1 cells were initially lysed using electrical pulses, and their genomic DNA was later analyzed by on-chip PCR. The integrated microfluidic device has the ability of performing the experiment with limited human interaction. The device is similar to the one used in our previous work[23]. The top layer is consisted of the control channels (A, B, D), and a hydration channel (C). The fluidic layer has channels of different depths that can be isolated from each other using the microfluidic valves (i.e. loading and reaction channels). Valves can also be used to completely isolate the fluidic channels to three separate chambers (if they are completely isolated, we will be calling them chambers from now on). Depending on the demands of each particular step of the integrated process, a different number of valves was actuated, and different solutions

entered the system. The device was also equipped with two gold surface electrodes to allow electrical cell lysis.

Initially, valve B was closed to separate the center channel of the device (reaction channel) with the two marginal ones (loading channels). A low number of CHO-K1 cells, suspended in low conductivity buffer, was added through the main channel (solution A in Fig. 3.1A), and immediately after that, valves A and D closed to completely isolate the reaction chamber. Electrical cell lysis followed, when electrical pulses were generated by two gold surface electrodes that were in contact with the cell suspension. After the cell lysis, valves A and D opened, and PCR master mix (Solution B) was flushed in the loading chamber, before A, and D closed once more. Mixing of the solutions that were present in the loading and reaction chambers (i.e. master mix and the extracted intracellular material respectively) followed by opening valve B. Diffusion was the only driving force for mixing, in the absence of advective flow. Smaller molecules that were present in the master mix (such as dNTPs, polymerase etc.) diffused in the center chamber, while the larger genomic DNA did not diffuse out[23]. We found that 30 minutes were enough, to achieve the required master mix concentration in the reaction chamber. The next step was on-chip PCR. For that, all valves closed once more, including the hydration chamber (valve C), and the microfluidic device was mounted on a flatbed thermal cycler. The temperature and cycling parameters are shown on paragraph 3.1.2.2. After the completion of the on-chip PCR, the amplified product was flushed out of the device, and analyzed further using real-time PCR. A quantitative result, with regards to the initial amount of DNA in the solution, was determined using this method.

Figure 3.2 shows data obtained from these experiments, and specifically from the RT PCR. Different initial cell numbers were tested. The electrical conditions that were used for the cell lysis were 2000 V/cm, for a total duration of 1 minute, throughout 10 DC square pulses (i.e. 100ms

duration per pulse, and one pulse every 10 seconds). Increase of the initial number of cells showed a slight increase in the number of amplified copies after the on-chip PCR (i.e. before the RT PCR) for the same electrical parameters. On the other hand, absence of the electric field, resulted in a much lower number of copies, even if the initial number of cells was higher. This result is even more interesting, if it is compared with the melt curve of figure 3.2B. The sample with absence of electric field has a peak at 73ºC, which is the same as the sample with the no-template negative control (i.e. water). On the contrary, the samples that experienced electric field, presented a melt temperature of 82ºC, which is the same as the sample with the purified DNA. The no-template negative control and the purified DNA are negative and positive controls that denote the melt temperatures of the primer dimers and the product of interest respectively. Therefore, we conclude that the presence of a high electric field on the sample, was responsible for the electrical lysis of cells and the extraction of DNA.

Figure 3.3A shows a sequence of images during the electrical pulses in the reaction chamber. Immediately after the application of pulses, bubbles are generated on the electrodes due to water electrolysis according to the following reactions.

Cathode: $4\,H_2O + 4e^- \rightarrow 4OH^- + 2H_2$

Anode: $2H_2O \rightarrow 4H^+ + 4e^- + O_2$

The bubbles become slightly bigger during the following pulses, but eventually disappear by diffusing out of the device through the gas permeable PDMS. In order to achieve that, the hydration chamber was actuated during the pulses to add pressure to the reaction chamber and lead to faster disappearance of the bubbles[13]. Additionally, we ensured that consecutive pulses had reverse direction to counteract the generation and accumulation of H^+ and OH^- in the device. Otherwise,

the electrical pulses could result to the generation of a high pH gradient, due to the contact of the electrodes with the solution, that could potentially harm the DNA or the master mix[24].

The cell lysis process can be observed in the phase contrast images of figure 3.3B. CHO-K1 cells are shown intact before the pulses. After a few pulses, it is clear that the cells are damaged, and only cell debris is present. It is important to note, that cells possess a negative surface charge at physiological pH, which results to a negative electrophoretic mobility. On our previous work we showed, that if cells are exposed to an electric pulsed field in a closed microchamber, they will eventually focus at the center of the chamber, due to a high pH gradient that appears[24]. Here, reversal of the direction of the electric field, ensures that such a focusing doesn't take place. However, electrophoretic mobility of the cells is still present, which drives them throughout the chamber, at the high electric field.

3.4 CONCLUSION

In this chapter, we presented a microfluidic device for electrical lysis of mammalian cells and subsequent on-chip PCR. With experimental data, we showed that a high electric field was necessary to breach the cell membrane and extract the genomic DNA. The reagentless cell lysis has the important advantage of possible elimination of the DNA purification step, which is typically necessary before PCR amplification. We anticipate that our simple, integrated device will find use in many microfluidic platforms for genetic analysis of cells.

REFERENCES

1. C. P. Jen, J. H. Hsiao and N. A. Maslov, *Sensors*, 2012, **12**, 347-358.
2. J. Kim, M. Johnson, P. Hill and B. K. Gale, *Integr. Biol.*, 2009, **1**, 574-586.
3. D. Di Carlo, C. Ionescu-Zanetti, Y. Zhang, P. Hung and L. P. Lee, *Lab on a Chip*, 2005, **5**, 171-178.
4. Y. H. Zhan, Loufakis, D.N., Bao, N., Lu, C., *Lab on a Chip*, 2012, **12**, 5063-5068.
5. J. Kim, S. H. Jang, G. Y. Jia, J. V. Zoval, N. A. Da Silva and M. J. Madou, *Lab on a Chip*, 2004, **4**, 516-522.
6. D. Di Carlo, K. H. Jeong and L. P. Lee, *Lab on a Chip*, 2003, **3**, 287-291.
7. H. Takamatsu, R. Takeya, S. Naito and H. Sumimoto, *J. Biomech.*, 2005, **38**, 117-124.
8. R. H. Liu, J. N. Yang, R. Lenigk, J. Bonanno and P. Grodzinski, *Anal. Chem.*, 2004, **76**, 1824-1831.
9. S. K. Baek, J. Min and J. H. Park, *Lab on a Chip*, 2010, **10**, 909-917.
10. A. K. White, M. VanInsberghe, O. I. Petriv, M. Hamidi, D. Sikorski, M. A. Marra, J. Piret, S. Aparicio and C. L. Hansen, *Proceedings of the National Academy of Sciences of the United States of America*, 2011, **108**, 13999-14004.
11. H. Lu, M. A. Schmidt and K. F. Jensen, *Lab on a Chip*, 2005, **5**, 23-29.
12. H.-Y. Wang, A. K. Bhunia and C. Lu, *Biosensors & Bioelectronics*, 2006, **22**, 582-588.
13. T. Geng, Bao, N., Sriranganathan, N., Li, L., Lu, C., *Anal. Chem.*, 2012, **84**, 9632-9639.
14. Y.-H. Lin and G.-B. Lee, *Applied Physics Letters*, 2009, **94**.
15. J. L. Tymoczko, Berg, J.M., Stryer, L., *Biochemistry A Short Course*, W.H. Freeman and Company, New York, 2010.

16. K. J. Livak, S. J. A. Flood, J. Marmaro, W. Giusti and K. Deetz, *Pcr-Methods and Applications*, 1995, **4**, 357-362.

17. A. Polini, E. Mele, A. G. Sciancalepore, S. Girardo, A. Biasco, A. Camposeo, R. Cingolani, D. A. Weitz and D. Pisignano, *Biomicrofluidics*, 2010, **4**.

18. K. A. Heyries, C. Tropini, M. VanInsberghe, C. Doolin, O. I. Petriv, A. Singhal, K. Leung, C. B. Hughesman and C. L. Hansen, *Nature Methods*, 2011, **8**, 649-U664.

19. J. S. Marcus, W. F. Anderson and S. R. Quake, *Anal. Chem.*, 2006, **78**, 956-958.

20. N. M. Toriello, C. N. Liu and R. A. Mathies, *Anal. Chem.*, 2006, **78**, 7997-8003.

21. V. Lecault, M. VanInsberghe, S. Sekulovic, D. J. H. F. Knapp, S. Wohrer, W. Bowden, F. Viel, T. McLaughlin, A. Jarandehei, M. Miller, D. Falconnet, A. K. White, D. G. Kent, M. R. Copley, F. Taghipour, C. J. Eaves, R. K. Humphries, J. M. Piret and C. L. Hansen, *Nature Methods*, 2011, **8**, 581-U593.

22. P. M. Nissom, *Biologicals : journal of the International Association of Biological Standardization*, 2007, **35**, 211-215.

23. S. Ma, D. N. Loufakis, Z. Cao, Y. Chang, L. E. K. Achenie and C. Lu, *Lab on a Chip*, 2014.

24. D. N. Loufakis, Z. Cao, S. Ma, D. Mittelman and C. Lu, *Chemical Science*, 2014, **5**, 3331-3337.

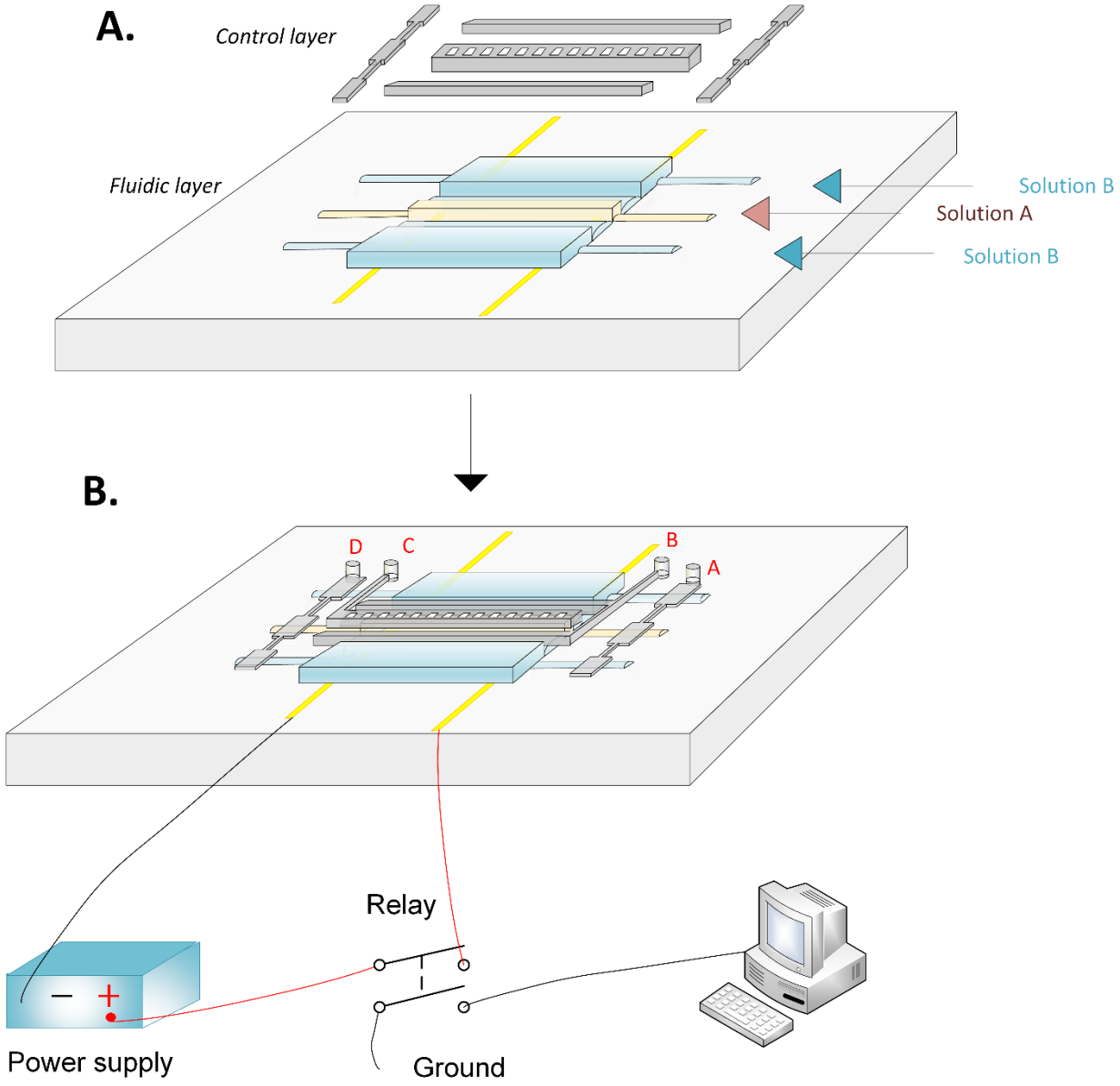

Figure 3.1. The design and setup of the entire microfluidic chip. A) The fluidic and control layers of the device. When the valves are depressurized, the device is unified, however application of the valves isolates the pink and blue illustrated areas from each other. Solution A is the cell suspension,

which flows through the center channel (illustrated in pink). Solution B initially enters through the blue areas, and later diffuses into the center channel. B) Valve B isolates the pink from the blue areas. Once there are enough cells in the center channel (pink area), valves A and D close, to completely isolate the chamber. Gold surface electrodes are connected to an external power supply and a relay system controlled by a computer, to generate pulses in the confined center chamber. After the electropulsation, valve B opens, and the master mix, which is located in the blue areas, is diffused in the central area. Later, all valves are closed once more, and the device is placed on a thermal cycler for on chip PCR. Valve C is the hydration layer, which is used to reduce evaporation during on chip PCR.

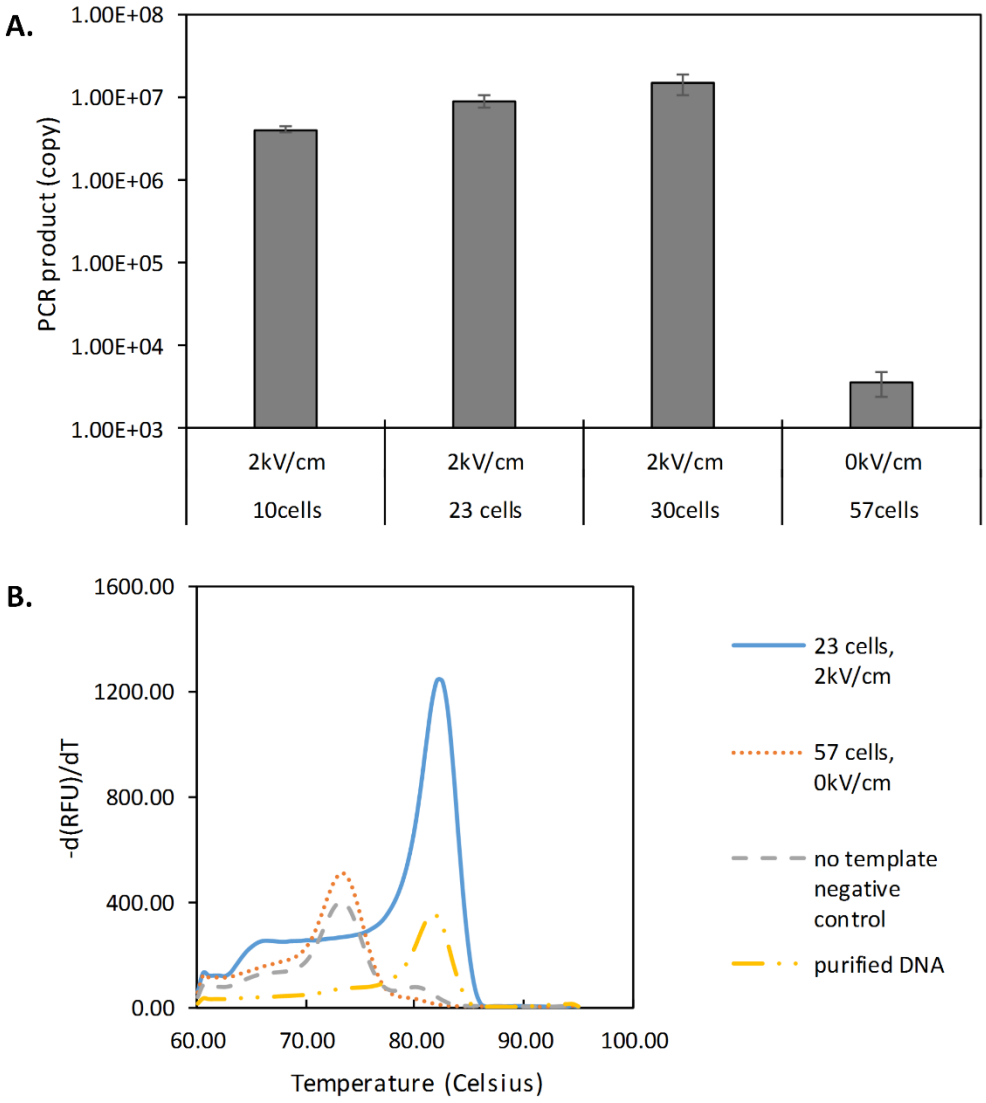

Figure 3.2. Results from electrical cell lysis followed by on-chip PCR. The amplification product was flushed out of the device and quantified on RT-PCR. A) The number of copies of the amplified gene of interest after on-chip PCR. Samples with 10, 23 and 30 cells were exposed to 2 kV/cm electrical pulses, for a total of 1 minute duration, for electrical lysis. In a control experiment, a sample with 57 cells was exposed to a 0 kV/cm electrical pulses (i.e. no electric field) and amplified on chip. B) The melt curve obtained after the RT-PCR. The samples with the purified

DNA and the 2kV/cm-exposed-cells have the same melting temperature, which means that they correspond to the same product. Similarly, the samples with the 0kV/cm-exposed-cells and the no-template negative control have the same melting temperature, which corresponds to primer dimers.

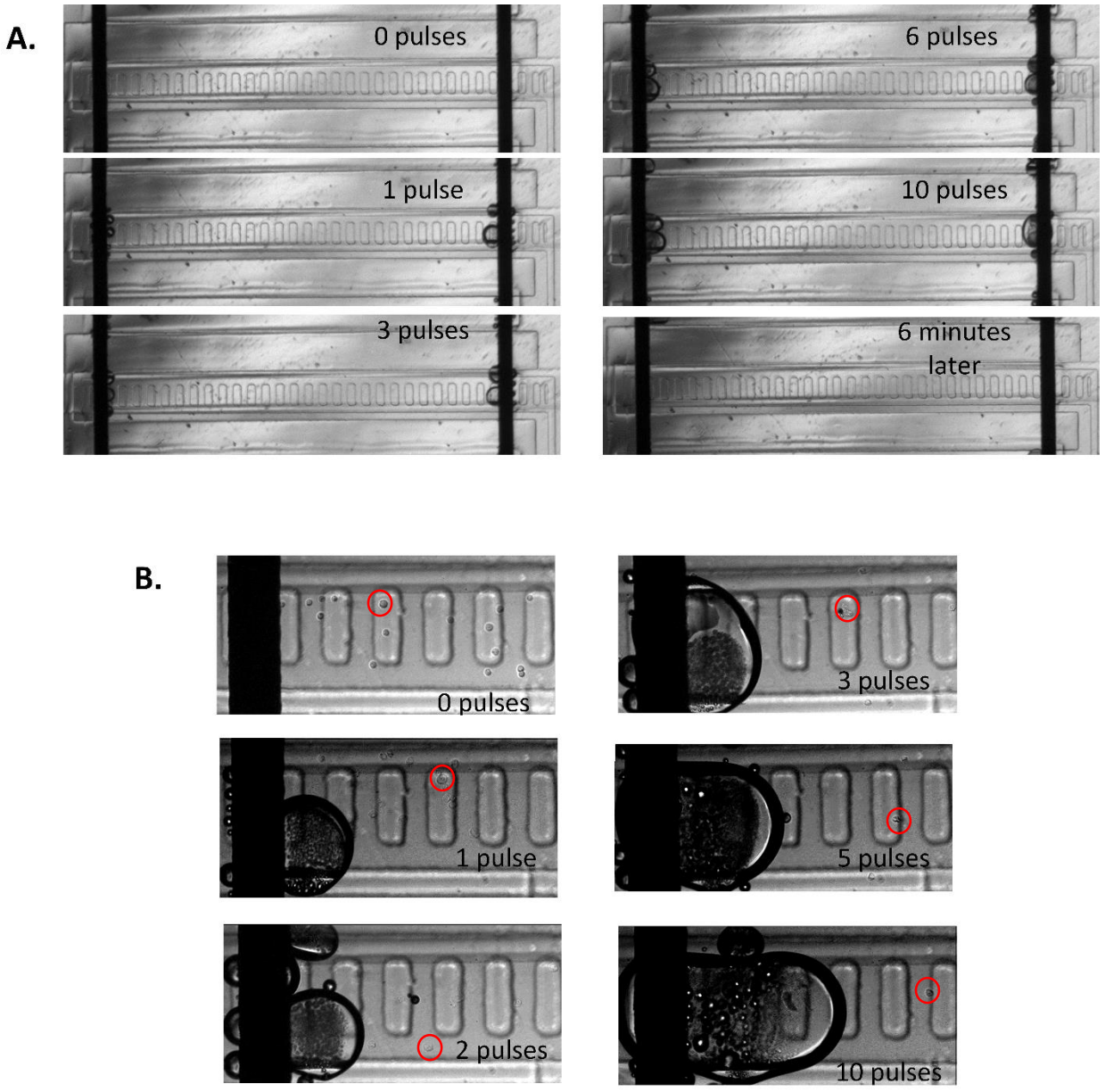

Figure 3.3. Time lapse images of the electropulsation area. A) Bubbles are generated at the area of the electrodes during the electrical pulses. Six minutes after the termination of the pulses, the bubbles diffuse through the gas permeable PDMS. B) The cell lysis observed under the differential interference contrast (DIC) microscope during 10 pulses.

CHAPTER 4 – SHEAR STRESS INDUCED ELECTROPORATION

4.1 INTRODUCTION

Biological cells are surrounded by a phospholipid bilayer membrane that encloses and protects intracellular material such as proteins, and genetic information[1]. The advancement of the field of biomedical engineering, often requires the access to the interior part of the cell, either for introduction of exterior molecules or extraction of intracellular material[2]. For example, in genetic engineering, foreign genetic information needs to penetrate through the cell's membrane before it is expressed in the transfected cell[3-5]. On the other hand, new diagnostic methods and drug development are often based on the relationship between the expressions of particular proteins and the pathological state of cells. For that, the release of the cell contents is necessary by means of transient or permanent breakage of the cell membrane[6, 7]. Of particular interest are the former methods for introduction of foreign molecules into cells, and for applications such as gene therapy. Typically, these methods must be "gentle" to cells, and must be accompanied by high cell viability rate; only when the cells are alive, will they be able to express the introduced gene.

Several methods have been developed to gain access to the interior part of the cell. These include biological [8-10], chemical [9-11], and physical methods[2, 12]. Typically biological methods (e.g. viral vectors) are used to introduce exogenous DNA or RNA to the cell and transfect it with new genes, but they suffer from high cytotoxicity[13]. In order to overcome this drawback, non-viral, vectors (i.e. chemical methods) were developed that are not as toxic to cells, but, on the same time,

are less efficient. The best approach for cell transfection proves to be electroporation[14, 15]. It is a simple physical method that uses electric field to generate pores on the cell membrane, which allow the introduction of molecules into the cell. It has high efficiency and reproducibility and it can be applied to many cell types. In addition, another advantage of electroporation is that the generation of pores may allow the transport of materials not only into, but also out of the cell[6, 16]. In comparison to other methods (biological and chemical), only chemical treatment could lead to extraction of cell contents by permanent membrane breakage using lysing agents.

4.1.1 THEORY OF CELL ELECTROPORATION

When a cell is exposed to an external electric field, a transmembrane potential ($\Delta\psi_E$) is generated between the interior and exterior part of the cell. With the application of the field, at first the membrane acts as a capacitor and it is charged, up to a maximum $\Delta\psi_E$. After that, a rapid discharge takes place, by the generation of micropores on the cell membrane. During this time, which is only in the range of microseconds, the transfer of materials (into or out of the membrane) can take place. It has been found that the transmembrane potential follows the equation[17]:

$$\Delta\psi_E = \psi_{in} - \psi_{out} = -f g(\lambda) E cos\theta \qquad \text{eqn. 4.1}$$

where f = 1.5 for sphere-shaped cells and f = 2 for rod-like cells, $g(\lambda)$ is a function related to the conductivities of the cell and the medium inside and out of the cell, E is the electric field intensity and θ is the angle between the direction of the electric field and the normal of the cell starting from its center. This equation assumes that the charging time for the cell membrane is much smaller compared to the electric pulse duration. The cosine term suggests that the cell membrane does not experience the same absolute potential throughout its circumference, rather it varies with a maximum at $\theta = 0^{o}$ and $\theta = 180^{o}$, and a minimum at $\theta = 90^{o}$. Therefore, the generation of pores

is expected to be more intense at the poles compared to the rest of the cell membrane area[15]. It has been found that the generated pores are quantitatively more at the poles, but are bigger in size closer to the equator. Moreover, generally, higher electric field intensity leads to larger pores, but longer electric pulse duration, results to the increase of the number of pores overall[2].

4.1.2 MICROFLUIDIC DEVICES FOR CELL ELECTROPORATION

Microfluidic devices prove to be ideal for performing cell electroporation. Apart from their characteristic dimensions, which are ideal for cell manipulation, and the laminar flow profile, which is excellently controlled, the specific-application-optimized architecture and the ability of implementation of electrodes in a simple manner, have given rise to several microfluidic electroporation platforms[2, 18-21].

The electrodes are the main feature of a microfluidic electroporation device and are necessary to transfer the electric field to the microsystem. They can either be fabricated on the surface of the device (surface electrodes)[6, 16, 22, 23], or they can be embedded in the system, through the inlet and outlet of the channel, in the form of wires[15, 24, 25]. The surface electrodes are typically out of Au or indium tin oxide (ITO), with varied shape depending on the operation of the device. Their advantage is that they can be fabricated on specific areas of the channel, to apply locally the electric field. This is important for integrated microfluidic devices, where an upward/downward analysis might be inhibited by the electric field. However, since the electrodes are in contact with the medium, the generation of bubbles might be a problem due to water electrolysis.

On the other hand, the latter category of devices is less demanding in terms of fabrication, and the wired electrodes are typically made out Pt or Ag/AgCl, due to their chemical stability. The downside is that the required voltage for the same field intensity is higher compared to having

surface electrodes, because the electrodes are typically further apart. Several optimization techniques have been demonstrated, that mostly deal with the architecture of the device, in order to increase the electric resistance in a specific location, and therefore increase the field intensity.

Flow through electroporation is a method for microfluidic electroporation that uses geometric variation of the channel for local maxima in the electric field[15, 26, 27]. According to Ohm's law, when a DC field is applied at a conductive channel with sectors of different areas, then the field intensity in each section will follow the equation:

$$\frac{E_i}{E_j} = \frac{A_j}{A_i} \qquad \text{eqn. 4.2}$$

where *E* is the electric field intensity and *A* is the area.

Assuming that the height is the same everywhere, and that there are two different widths, then equation 2 becomes:

$$\frac{E_1}{E_2} = \frac{W_2}{W_1} \qquad \text{eqn. 4.3}$$

where *W* is the width, the narrow section is denoted by *1*, and the wide section by *2*. A schematic of the system is shown in figure 4.1A.

For a desired field intensity, the necessary voltage, *V*, to be applied can be calculated by:

$$V = E_1\left(\frac{L_2 W_1}{W_2} + L_1\right) \qquad \text{eqn. 4.4}$$

The total duration that each cell experiences the high field intensity, equals to the residence time of the cells in the narrow section:

$$Q = \frac{W_1 L_1 H}{T_1} \quad \text{eqn. 4.5}$$

Flow through electroporation is a simple method for electroporation of cells in suspension, with a simple power supply. It has the advantage of high processing rates using high flow rates, showing remarkable results of high efficiency and high viability[27]. It has been found that the increased efficiency originates from the rotational trajectory of the cells in the microfluidic system[28]. Although there is a constant DC voltage in flow through electroporation experiments, it has been shown that typically the temperature increase is below cytotoxic levels, mainly due to the flow rate[29].

In other studies, researchers coupled electroporation with hydrodynamic focusing, a method that takes advantage of the laminar flow profile of the system. In such a device, a three layer flow is developed, with the sandwiched layer having a much lower conductivity buffer compared to the two that surround it. As a result, a desired electric field intensity is generated in the middle layer (which contains the cell suspension) with application of minimal voltage[22, 25].

Even though there has been an excessive list of studies on microfluidic electroporation systems, to our knowledge, there isn't any report that examines the effect of the shear stress profile on the cell electroporation efficiency. It is expected that mechanical stress, induced by the shear rate, will promote the generation of pores on the cell membrane[30]. Using two different device configurations (one with cells flowing in suspension and one with attached cells), we studied the effect of the shear stress on the permeabilization of the cell membrane.

4.2 MATERIALS AND METHODS

4.2.1 DEVICE OPERATION

Two different device configurations were used during this project (Fig. 4.1), and they were fabricated using soft lithography (Appendix A). On the first set of experiments, flow-through electroporation was conducted, using the device shown on figure 4.1A. Its height was 28 μm, and it was 35 μm and 500 μm wide at the narrow and wide sections respectively. Different lengths of the two sections were tested. Two platinum electrodes were inserted in the inlet and outlet of the channel and were connected to an external power supply. The experiments were conducted in the biosafety cabinet to prohibit contamination. At first, a phosphate buffer was flown through the device to expel all air bubbles. During the experiment, the cell suspension (80 μl) flowed at a particular flow rate, which was determined by a syringe pump. The cells were electroporated when they passed through the narrow section. The residence time at this section (i.e. the pulse duration) was set to be 4.2 ms at all experiments. After the cells exerted the device, they were collected in 2 96-well plates (i.e. 40 μl in each well plate) filled with 200 μl medium, and incubated at 37oC and 5% CO2 concentration. The cells in the first well plate were examined after 1 hour for determination of the viability rate. Specifically, they were, first, washed with PBS (Fisher Scientific, Suwanee, GA) by centrifugation at 200g for 5 minutes, and then, propidium iodide (Life Technologies Corporation, Grand Island, NY) solution was added to the cells at a concentration of 1 $\mu g\ ml^{-1}$. After incubation in the dark, and at room temperature for 15 minutes, they were centrifuged and rewetted with PBS. The well plate was placed on an inverted fluorescence microscope (IX-71, Olympus, Melville, NY), equipped with a 10x objective, and a CCD camera (ORCA-285, Hamamatsu, Bridgewater, NJ). Fluorescent images were taken using a filter cube with excitation filter HQ535/50x, emission filter HQ645/75m and beamsplitter Q565LP (Chroma

Technology). The second well plate was used to determine the efficiency rate. The incubation time depended on the molecule that was delivered to the cells. For the case that the cells were transfected with plasmid, they were incubated for 48 hours, before they were washed with PBS, and examined for fluorescence. For that, a FITC filter cube was used with excitation filter HQ480/40x, emission filter HQ535/50m and beamsplitter Q505LP (Chroma Technology). ImageJ was used to count the cells in the fluorescent and phase contrast images.

The second set of experiments was done using the device configuration 4.1B. Its dimensions were 500 μm wide, 36 μm deep, and 7 mm long. CHO-K1 cells were cultured according to the protocol (Appendix B), and were attached in the device one day before the experiment. More specifically, at first, fibronectin from bovine plasma (Sigma-Aldrich, St. Louis, MO) at a concentration of 100 $\mu g\ ml^{-1}$ was flown through the device, which was later incubated at 37^oC for 1h. Cells were harvested and resuspended in medium at a concentration 2.5×10^6 cells ml^{-1}, and 5 μl of the suspension was added at the outlet of the microchannel to let the cells flow in the device. A 200 μl tip was added in the outlet, and was filled with medium to allow perfusion for the next several hours. The device was incubated at 37^oC and 5% CO_2 concentration until used. Before the experiment, the tip was extracted, and the liquid in the outlet was aspirated and substituted by phosphate buffer [8 mM Na_2HPO_4 (Sigma-Aldrich), 2 mM KH_2PO_4 (Sigma-Aldrich), and 250 mM sucrose (Sigma-Aldrich), pH=7.4]. At least 5 minutes later, the liquid in the outlet was substituted by a phosphate buffer supplemented with SYTOX Green(Life Technologies Corporation, Grand Island, NY). Platinum wired electrodes were installed in the inlet and outlet of the channel, and connected to a custom electronic circuit and an external DC power supply (PS350, Stanford Research Systems, Sunnyvale, CA). The circuit was controlled by a DAQ card (NI SCB-68, National Instruments, Austin, TX) and a LabView program (National

Instruments, Austin, TX) to provide electrical pulses (10ms duration) to the cells in the channel. A SYTOX solution flowed in the device at a specified flow rate for 3 minutes, and then the pulse was applied. After the experiment, the outlet reservoir was emptied and filled with medium, and the device was incubated at 37oC and 5% CO2 for 1 h. Later, the device was mounted on the inverted fluorescence microscope and fluorescent images were taken using the FITC filter cube (excitation: ET480/40x, emission: ET535/50m). The images were analyzed using a MATLAB (Mathworks, Natick, MA) code, and ImageJ.

4.2.2 CELL SUSPENSION PREPARATION

CHO-K1 cells were cultured according to the protocol shown in Appendix B. Before the flow-through electroporation experiments, they were harvested, and washed with PBS by centrifugation at 300g for 5 minutes. They were resuspended in phosphate buffer supplemented with pEGFP-C1 plasmid vector (4.7 Kb, Clontech, Palo Alto, CA) at a concentration of 40 μg ml^{-1} or 60 μg ml^{-1}.

4.2.3 COMSOL MULTIPHYSICS SIMULATIONS

COMSOL Multiphysics 4.3 was used to simulate the flow profile in the device. The module "Laminar Flow" was used to solve the steady state Navier Stokes equation coupled with the continuity equation at a 3-D model.

$$\rho(v \cdot \nabla v) = -\nabla P + \mu \nabla^2 v \qquad \text{eqn.4.6}$$

$$\nabla \cdot (\rho v) = 0 \quad \text{eqn.4.7}$$

where ρ is the fluid density, v is the velocity, P is the pressure, μ is the viscosity.

The boundary conditions were the flow rate at the inlet and a zero relative pressure at the outlet.

For the case of flow through electroporation experiments, only the narrow section of the device was modeled, for ease of computation. The mesh size varied between 139125, 168375, 220875, 310125, 424500 for devices of narrow section length between 1.5, 2, 3, 5, 8 mm respectively. For the second device configuration, the total mesh elements were 472800.

4.3 RESULTS AND DISCUSSION

Two different set of experiments were conducted during this project to determine the effect of shear stress on the electroporation efficiency that was performed on suspended, and attached CHO-K1 cells. In both cases, the electric field distribution during the pulse was homogenous. At the flow-through electroporation device (Fig. 4.1A), the cells were in suspension, and therefore the field intensity that they experienced was dependent on their location inside the device. As it was explained above, an electric field exists in both the wide and narrow sections of the microchannel, since the wired electrodes are at the inlet and the outlet of the channel. However, only the one at the narrow section is high enough, while the other one is considered insignificant. As a result, the cells experienced a pulsed electric field, when they passed through the narrow section of the device. The second device configuration (Fig. 4.1B) required a custom electronic circuit to apply electrical pulses to the attached cells. We will discuss the results from each device configuration separately, starting from the flow-through electroporation experiments.

The device shown in figure 4.1A was tested first. The shear stress in the device varied, by varying the flow velocity, while the electric field parameters (i.e. electric field intensity, and pulse duration) remained constant. The residence time in the narrow section (i.e. the pulse duration) was kept at 4.2 ms at all cases, by altering its length. Previous studies showed, that the ratio of the narrow and wide section lengths also affects the electroporation efficiency[27]. Therefore, we varied

Length of narrow section (mm)	***Total length of wide section (mm)***	***Flow rate (μl min^{-1})***	***U_{max} (m s^{-1})***
1.5	4.875	21	0.73875
2	6.5	28	0.984
3	9.75	42	1.48
5	16.25	70	2.46
8	26	112	3.94

Table 4.1. Parameters for the flow-through electroporation experiments. The lengths of the narrow and wide sections of the devices. The flow rate varied for each device, to result to 4.2 ms residence time in the narrow section at all cases. The final column shows the corresponding maximum velocity in the narrow section as determined by COMSOL Multiphysics.

the length of the different sections of the device proportionally as shown on table 4.1. For each case a different flow rate was used to result to the same residence time.

Computational simulations using COMSOL Multiphysics were performed to calculate the flow profile in the narrow section. The maximum velocity for each different geometry is presented in table 4.1. Figure 4.2A shows, that for the extreme cases, the wall shear stress increases by more than 5 times, and specifically varies from 1160 dyne cm^{-2} to 6200 dyne cm^{-2}. The velocity and shear stress profiles at a x-z slice and along the y-axis are shown for the device with 3 mm narrow section length (Fig.4.2B, C). The qualitative profiles at the devices with different lengths are

very similar, but they vary quantitatively. The mean cell diameter (~10 μm) is of the same order of magnitude as the width of the device (35 μm). Smaller channel width would lead to increased clogging. It is noted, that even though the exact trajectory of each cell in the channel is unknown, it is assumed that differences due to shear stress in different devices will be evident, considering the high cell number and narrow channel.

A CHO-K1 cell suspension was transfected with plasmid (40 μg plasmid ml^{-1} solution) in such a device. Figure 4.3 shows the results obtained for different field intensities. As it is expected, increase of the field intensity leads to increase in the electroporation efficiency rate. Higher electric field during a known pulse duration results to generation of larger pores[2], that may positively impact transfection. On the downside, this also promotes permanent cell electroporation (i.e. cell lysis) (Fig. 4.3B). Different narrow section lengths showed a variation in the efficiency only for the higher field intensities. In order to better visualize the results, we plotted the efficiency and the viability with respect to the narrow section length for 1000 V cm^{-1} and 1100 V cm^{-1} (Fig. 4.4A, B). Once more, higher field intensity resulted in overall better efficiency. The narrowest device showed slightly higher efficiency rate, without, however, having a significant difference. The same observation is apparent on figure 4.4C, which was obtained when the experiment was conducted with higher plasmid concentration (60 μg ml^{-1}), in attempt to detect higher variation between different devices. This was based on the findings of previous studies, which state that increase in the plasmid concentration, generally results to better efficiency, up to a threshold concentration, after which it becomes toxic to the cells[31].

The delivery efficiency of other small molecules into cells was also tested using the same device configuration. SYTOX green is a dye molecule, which penetrates through the pores of the

cell membrane during electroporation, and fluoresces when it intercalates within its DNA. In comparison to plasmid transfection, SYTOX is easier to be delivered. Figure 4.4E shows that 1100 V cm^{-1} results to efficiencies that reach almost 100% at all cases. A much lower field intensity of 500 V cm^{-1}, leads to overall lower efficiency rates that also demonstrate a variation between the device lengths. The delivery rate at short microchannels (1.5 and 2 mm narrow length) was 40%, and it increased to 60% for longer devices (3, 5, and 8 mm narrow length). In comparison to the plasmid transfection experiments, the effect of the device geometry (and therefore the effect of shear stress) followed a different general trend, suggesting the presence of a different mechanism for the delivery of each substance. For example, it is possible, that higher shear stress did not permit the delicate plasmid to penetrate through the pores of the membrane, by dragging it with the flow, or promoting its degradation[32, 33], something that did not apply to the smaller SYTOX molecule.

On the second set of experiments, the effect of shear stress on attached cells was studied, using the device configuration shown on figure 4.1B. The shear stress varied from 0.016 to 160 dyne cm^{-2} (Fig. 4.5A) by varying the inlet flow rates, and therefore the flow velocities (Table 4.2). COMSOL Multiphysics was used to simulate the flow profile inside the device. The velocity and shear stress profiles for each case vary only quantitatively, and are shown in figures 4.5B, and C for the case of 10 μl min^{-1}. This time, the cells are attached on the bottom wall of the microchannel, and as a result they experience a very specific, and controlled shear stress (at a ~3 μm depth).

Flow rate (μl min^{-1})	***U_{max} (m s^{-1})***
0.01	1.47E-05
0.1	1.47E-04
1	0.00147
10	0.0147
20	0.0294
50	0.073
100	0.1463

Table 4.2. The flow rates used for the second set of experiments, in which case the cells were attached, and the corresponding maximum velocities as computed by COMSOL Multiphysics.

A SYTOX solution flowed in the device, and the dye molecule entered the cell membrane during electroporation. The fluorescence intensity of cells was later analyzed on ImageJ, and the results were plotted with respect to the flow rate. Figure 4.6A shows the effect of low flow rates on the cell fluorescence. In general, increase of the electric field resulted to higher intensities. An increase in fluorescence is also observed for higher flow rates, suggesting that the shear stress had a positive impact on the electroporation efficiency. It is interesting to note, that very low rates (0.01 and 0.1 μl min^{-1}) resulted to a signal that was similar to that of the negative control with 0 V cm^{-1} electric field. Further increase of the flow rate plateaued its effect on the fluorescence intensity (Fig. 4.6B).

4.4 CONCLUSION

In this chapter, the effect of shear stress on the electroporation efficiency of suspended and attached cells was studied. The results showed that the later ones were more susceptible to shear stress, showing a bigger difference on their electroporation efficiency compared to the cells in suspension. More specifically, increase of the flow rate (and therefore the shear stress) resulted to increased electroporation efficiency, up to a threshold, after which the efficiency plateaued. The main reason is that the cells are on a fixed location on the z axis in the microchannel (at about 3 μm when they are attached), and therefore they experience a controlled, high shear stress. On the contrary, cells in suspension are allowed to rotate and move freely in the x-z plane, and as a result, the applied shear stress may vary on each cell. By examining the electroporation of suspended cells, if was found that plasmid transfection showed a smaller variation on the effect of shear stress at the examined parameters, that was possibly affected by the effect of shear stress on the plasmid. On the other hand, SYTOX delivery resulted to increased efficiency with increase of the shear stress. We anticipate, that our results will be important on future electroporation applications.

REFERENCES

1. B. Alberts, *Molecular biology of the cell*, Garland Science, New York, 2002.
2. T. Geng and C. Lu, *Lab on a Chip*, 2013, **13**, 3803-3821.
3. V. F. Van Tendeloo, C. Van Broeckhoven and Z. N. Berneman, *Leukemia*, 2001, **15**, 523-544.
4. M. Simonato, J. Bennett, N. M. Boulis, M. G. Castro, D. J. Fink, W. F. Goins, S. J. Gray, P. R. Lowenstein, L. H. Vandenberghe, T. J. Wilson, J. H. Wolfe and J. C. Glorioso, *Nature reviews. Neurology*, 2013, **9**, 277-291.
5. J. L. Pinyon, S. F. Tadros, K. E. Froud, Y. W. AC, I. T. Tompson, E. N. Crawford, M. Ko, R. Morris, M. Klugmann and G. D. Housley, *Science translational medicine*, 2014, **6**, 233ra254.
6. Y. Zhan, C. Sun, Z. Cao, N. Bao, J. Xing and C. Lu, *Analytical Chemistry*, 2012, **84**, 8102-8105.
7. E. R. Brown, T. Doig, N. Anderson, T. Brenn, V. Doherty, Y. Xu, J. M. S. Bartlett, J. F. Smyth and D. W. Melton, *European Journal of Cancer*, 2012, **48**, 865-874.
8. S. M. Dizaj, S. Jafari and A. Y. Khosroushahi, *Nanoscale research letters*, 2014, **9**, 252.
9. S. Zhang, Y. Xu, B. Wang, W. Qiao, D. Liu and Z. Li, *Journal of Controlled Release*, 2004, **100**, 165-180.
10. A. M. R. Haines, A. S. Irvine, A. Mountain, J. Charlesworth, N. A. Farrow, R. D. Husain, H. Hyde, H. Ketteringham, R. McDermott, A. F. Mulcahy, T. L. Mustoe, S. C. H. Reid, M. Rouquette, J. C. Shaw, D. R. Thatcher, J. H. Welsh, D. E. Williams, W. Zauner and R. O. Phillips, *Gene Therapy*, 2001, **8**, 99-110.

11. T. K. Kim and J. H. Eberwine, *Analytical and bioanalytical chemistry*, 2010, **397**, 3173-3178.

12. E. P. Papapetrou, N. C. Zoumbos and A. Athanassiadou, *Gene Ther*, 2005, **12 Suppl 1**, S118-130.

13. C. E. Thomas, A. Ehrhardt and M. A. Kay, *Nature reviews. Genetics*, 2003, **4**, 346-358.

14. J. Gehl, *Acta physiologica Scandinavica*, 2003, **177**, 437-447.

15. T. Geng, Y. Zhan, J. Wang and C. Lu, *Nat. Protocols*, 2011, **6**, 1192-1208.

16. T. Geng, N. Bao, N. Sriranganathanw, L. Li and C. Lu, *Analytical chemistry*, 2012, **84**, 9632-9639.

17. J. Teissie, M. Golzio and M. P. Rols, *Biochimica et Biophysica Acta (BBA) - General Subjects*, 2005, **1724**, 270-280.

18. S. Movahed and D. Li, *Microfluid Nanofluid*, 2011, **10**, 703-734.

19. S. Le Gac and A. van den Berg, *Methods in molecular biology (Clifton, N.J.)*, 2012, **853**, 65-82.

20. R. V. Davalos, Y. Huang and B. Rubinsky, *Microscale Thermophysical Engineering*, 2000, **4**, 147-159.

21. Y. Huang and B. Rubinsky, *Biomedical microdevices*, 1999, **2**, 145-150.

22. Z. Wei, D. Zhao, X. Li, M. Wu, W. Wang, H. Huang, X. Wang, Q. Du, Z. Liang and Z. Li, *Analytical Chemistry*, 2011, **83**, 5881-5887.

23. D. N. Loufakis, Z. Cao, S. Ma, D. Mittelman and C. Lu, *Chemical Science*, 2014, **5**, 3331-3337.

24. N. Bao, J. Wang and C. Lu, *Electrophoresis*, 2008, **29**, 2939-2944.

25. T. Zhu, C. Luo, J. Huang, C. Xiong, Q. Ouyang and J. Fang, *Biomedical microdevices*, 2010, **12**, 35-40.

26. H. Y. Wang and C. Lu, *Analytical Chemistry*, 2006, **78**, 5158-5164.

27. T. Geng, Y. Zhan, H.-Y. Wang, S. R. Witting, K. G. Cornetta and C. Lu, *Journal of Controlled Release*, 2010, **144**, 91-100.

28. J. Wang, Y. Zhan, V. M. Ugaz and C. Lu, *Lab Chip*, 2010, **10**, 2057-2061.

29. B. del Rosal, C. Sun, D. N. Loufakis, C. Lu and D. Jaque, *Lab on a Chip*, 2013, **13**, 3119-3127.

30. A. Sharei, J. Zoldan, A. Adamo, W. Y. Sim, N. Cho, E. Jackson, S. Mao, S. Schneider, M.-J. Han, A. Lytton-Jean, P. A. Basto, S. Jhunjhunwala, J. Lee, D. A. Heller, J. W. Kang, G. C. Hartoularos, K.-S. Kim, D. G. Anderson, R. Langer and K. F. Jensen, *Proceedings of the National Academy of Sciences*, 2013.

31. H. Y. Wang and C. Lu, *Biotechnology and bioengineering*, 2008, **100**, 579-586.

32. C. S. Lengsfeld and T. J. Anchordoquy, *Journal of pharmaceutical sciences*, 2002, **91**, 1581-1589.

33. F. J. Meacle, H. Zhang, I. Papantoniou, J. M. Ward, N. J. Titchener-Hooker and M. Hoare, *Biotechnology and bioengineering*, 2007, **97**, 1148-1157.

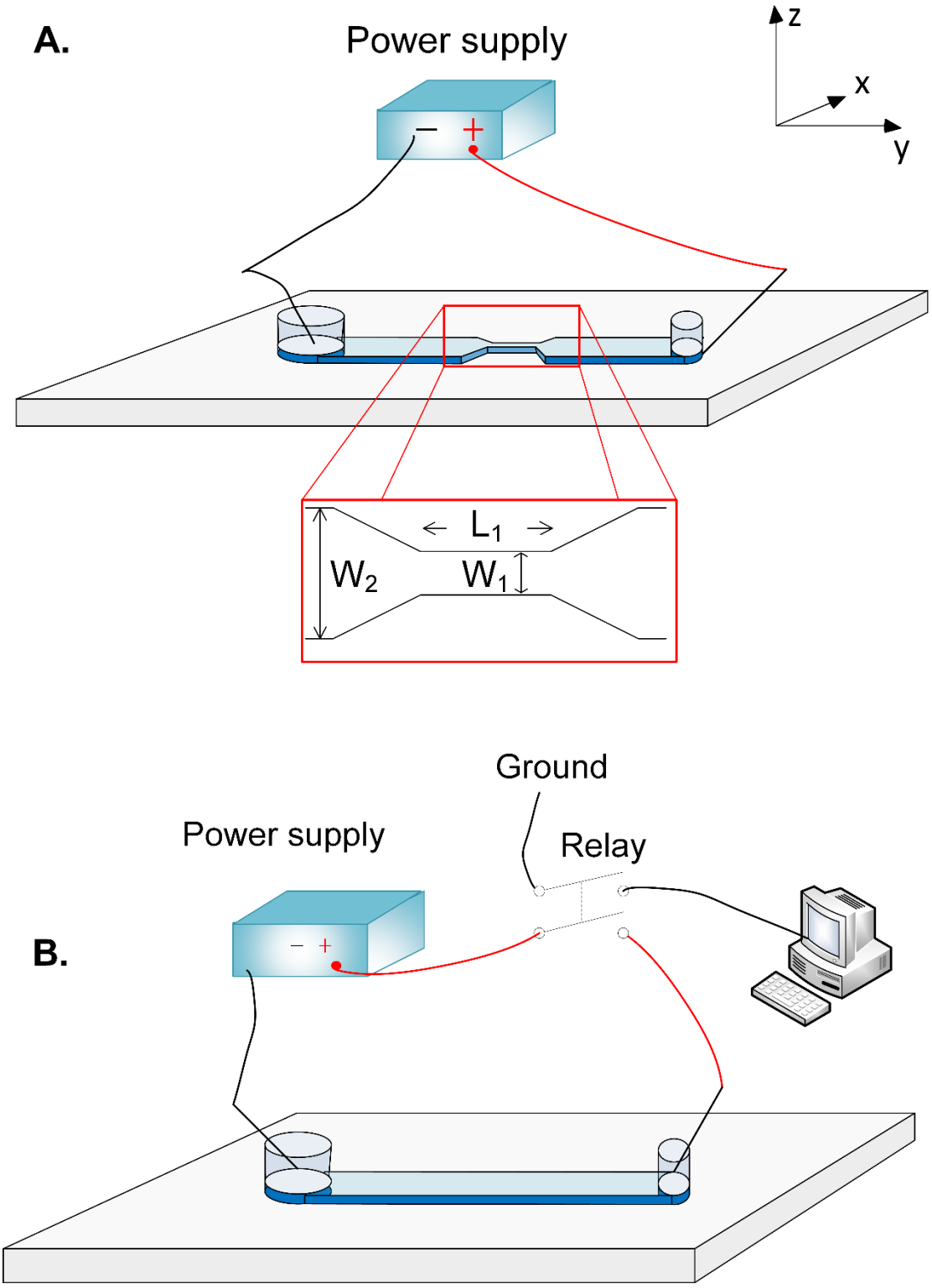

Figure 4.1. Schematic of the devices and the setup. A) A schematic representation of the flow through electroporation device. If a constant direct current voltage is applied through the inlet and

outlet of the system, the electric field within the device will vary due to the geometric variation. A higher field intensity will appear at the narrow area. The cells flow through the device at a controlled flow rate. B) A schematic representation of the device and the setup of the second set of experiments. The cells were attached on the glass.

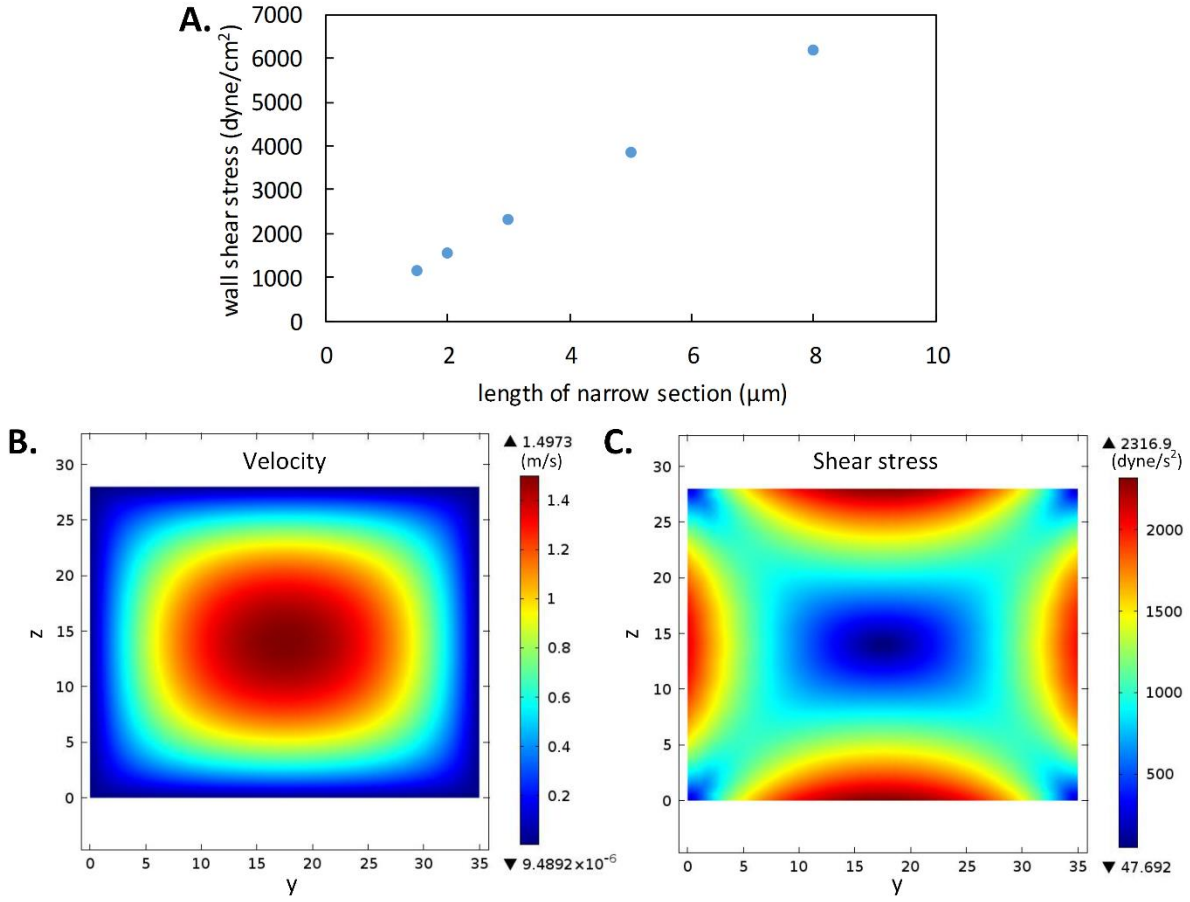

Figure 4.2. Results obtained from COMSOL Multiphysics modeling for the flow-through electroporation experiments. A) The wall shear stress generated at the narrow section of each channel for the flow-through electroporation experiments with respect to the length of the narrow section. At each different channel length, the flow rate was changed to result to the same residence time. B) The velocity profile of the device with 3 mm narrow section at a slice in the x-z plane, and in the middle of the narrow section along the y-coordinate. C) The shear stress profile at the same plane and for the same device.

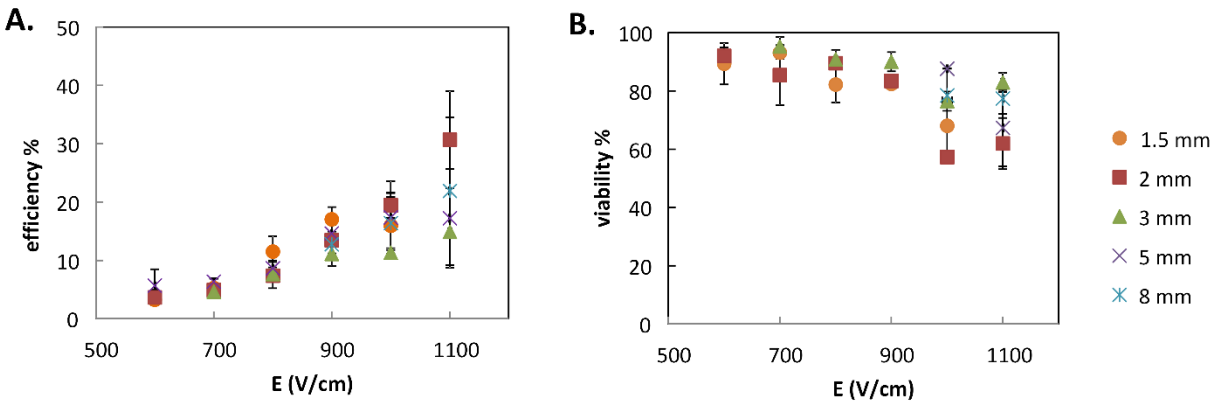

Figure 4.3. The efficiency (A) and the viability (B) with respect to the electric field for the flow-through electroporation experiments. Devices with different lengths were used. The length of the narrow section is shown on the legend. The plasmid concentration was 40 μg/ml solution.

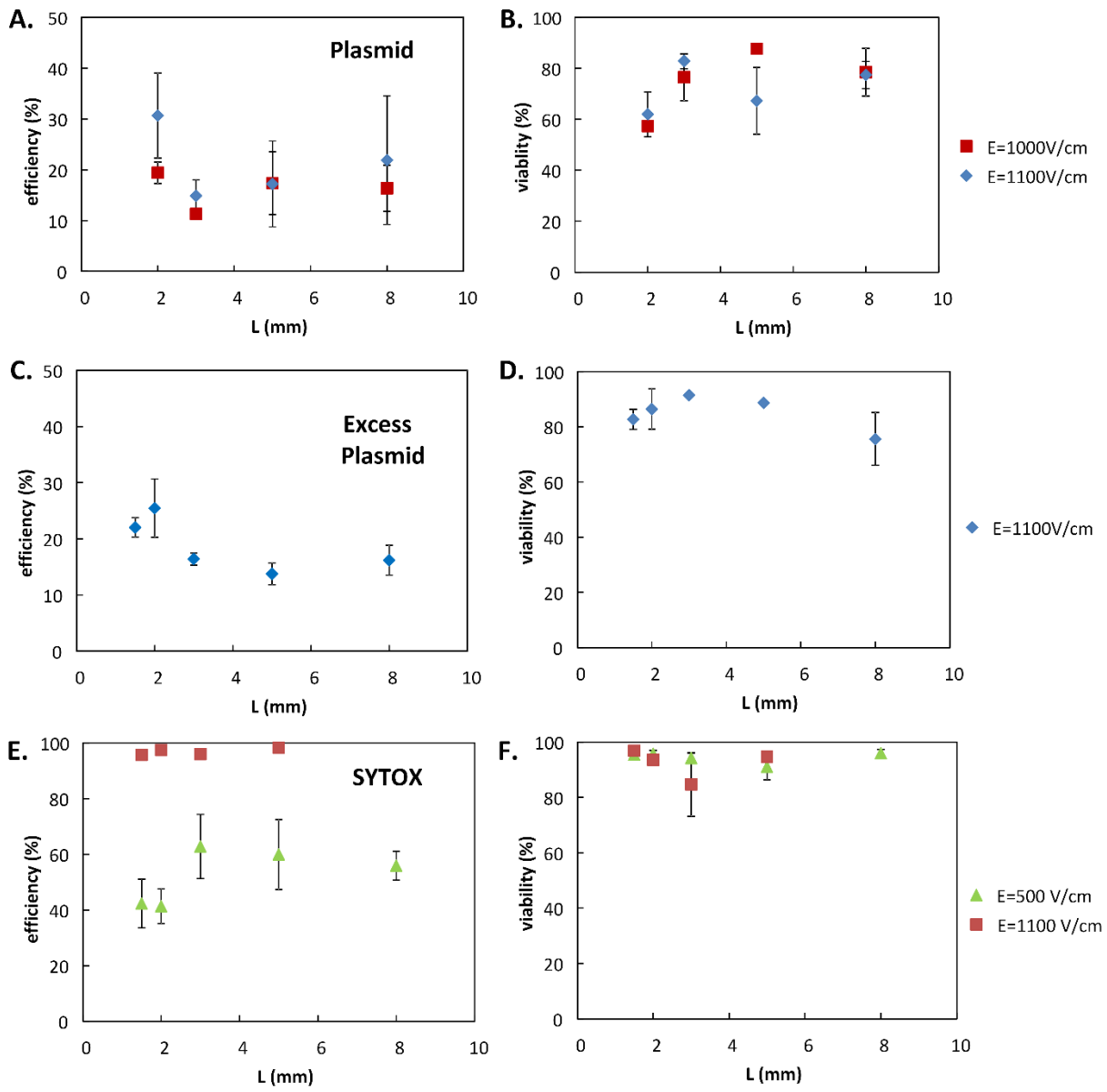

Figure 4.4. The efficiency and viability results for the flow-through electroporation experiments, with respect to the length of the narrow section. The electric field used in each case is shown on the legends. A, B) The delivered molecule was plasmid at a concentration of 40 μg/ml solution, and C, D) 60 μg/ml solution. E, F) The delivered molecule was SYTOX at a concentration of 1 μM.

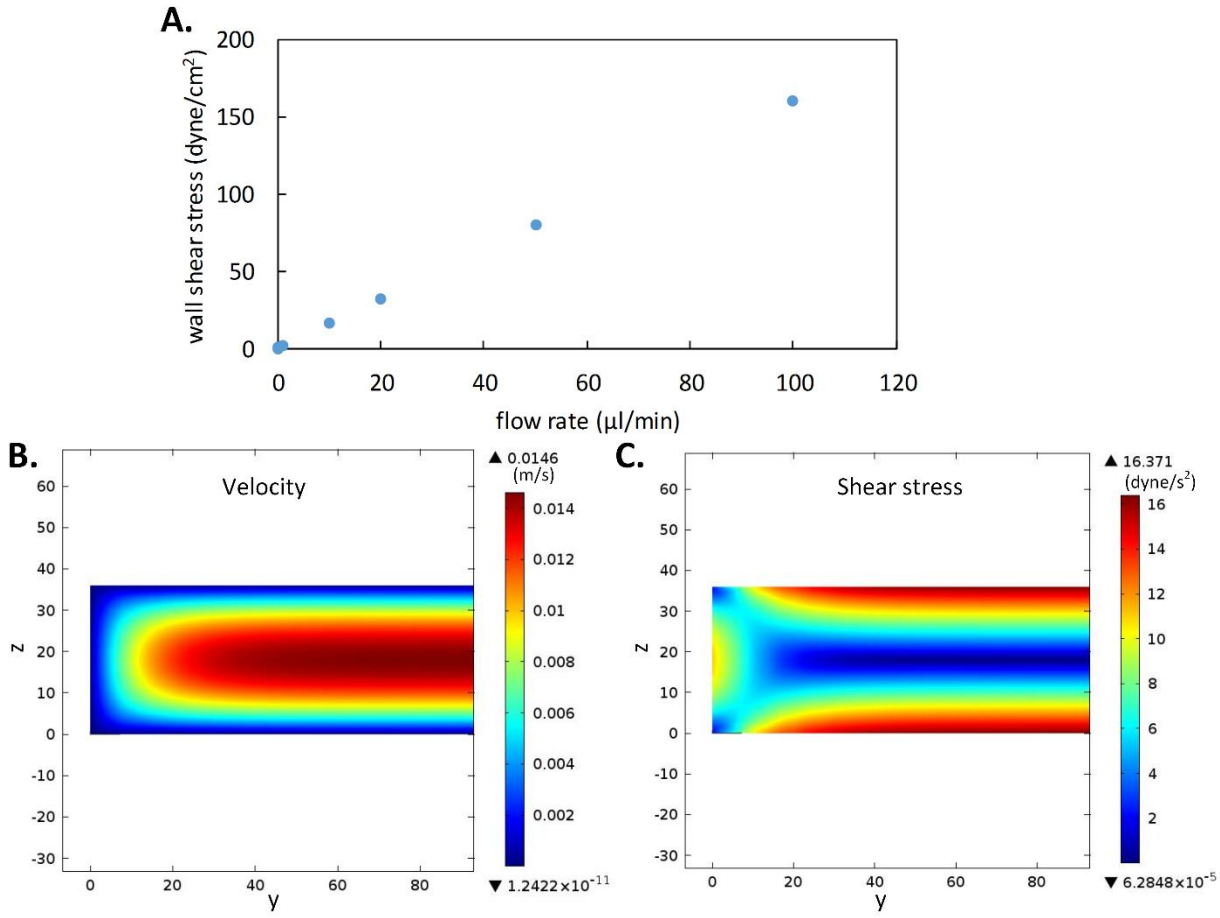

Figure 4.5. Results obtained from COMSOL Multiphysics modeling for the second device configuration. A) The wall shear stress with respect to the flow rate for the second set of experiments, at which the cells were attached on the device. B) The velocity profile at a x-z slice and at y = 4 mm (the total length of the device is 7 mm). The flow rate was 10 µl min^{-1}. C) The shear stress profile at the same x-z slice and for the same flow parameters.

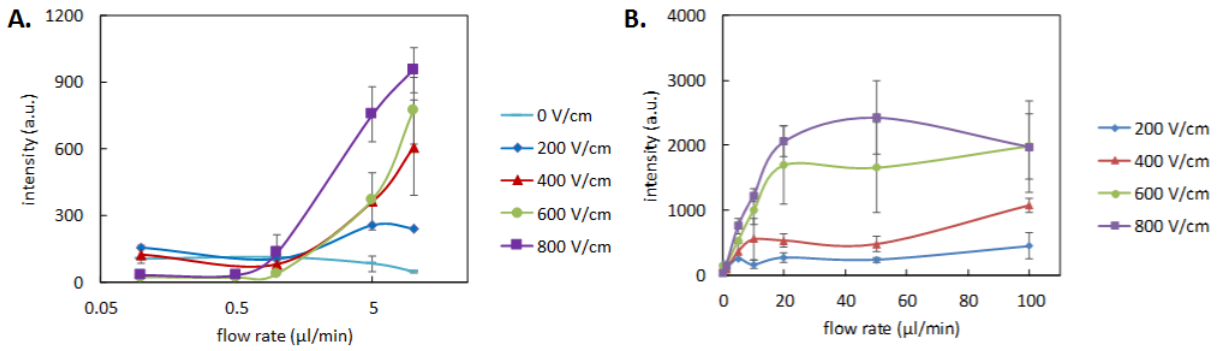

Figure 4.6. The fluorescence intensity of attached cells after electroporation with respect to the flow rate. The electric field intensity for each case is shown on the legend. A) The flow rate is shown on a logarithmic scale to better capture the effect of the low flow rates on the fluorescence intensity. B) The flow rate is presented on a non-logarithmic scale to better capture the effect of higher flow rates on the electroporation efficiency (as shown by the fluorescence intensity).

CHAPTER 5 – A SIMPLE METHOD FOR CHAMBER FORMATION IN MICROFLUIDIC DEVICES AND ITS IMPORTANCE ON SINGLE CELL ANALYSIS AND DIGITAL PCR

5.1 INTRODUCTION

The field of microfluidics emerged in the early 1980's and since then, it has given rise to many lab-on-a-chip (LOC) devices and micro-total-analysis systems (μTAS). The devices are characterized by channels of small dimensions (typically in the order of 10-1000μm), and therefore small volumes (in the order of 10^{-9} to 10^{-18} liters)[1]. As a consequence, less amounts of reagents are needed, and they can be easily manipulated. Moreover, the laminar flow profile, which is present in this systems, ensures excellent control of the streamlines and the flow profile of the sample.

These characteristics have established microfluidic platforms, to be ideal for studying biological cells. The mean diameter of a cell (~10 μm) is only one order of magnitude smaller compared to the typical width of a microfluidic channel (~100 μm). Manipulation of the cell trajectory can easily be achieved on chips, and visualization of the process is performed on inverse microscopes and is captured by CCD cameras. The biological applications of microfluidic systems range from including only a single step of a complicated process, such as separation of a particular cell type[2-4], to integrated chips that include several consecutive steps, such as cell lysis, DNA extraction, and DNA purification on chip[5-7].

Integrated microfluidic devices are often called micro total analysis systems (μTAS), because they include all (or most of) the steps of a process on chip. The miniaturization of the analysis on these lab-on-a-chip systems has led to simple, efficient, portable and automatic methods that are becoming increasingly popular. The input to these systems are often samples with cell suspensions, and in that case, cell trapping is the necessary first step.

5.1.1 CELL TRAPPING

Cell trapping often forms the first step in cell analysis studies. Downward analysis of the trapped cells might be simple observation of the cell cycle and the cell-cell interactions[8], or it might be more invasive, such as cell lysis, and analysis of the genetic information[5]. The conventional method demands that cellular studies are applied over a cell sample, in which case, the properties are averaged over the entire population, and variances between cells are lost. However, cells are rarely homogeneous in terms of phenotype, gene expression, and morphology[9]. As a result, the study of the cell heterogeneity is necessary, and it can be achieved through microfluidic platforms[10,11]. Cell trapping by surface modification (chemical or structural) or contactless immobilization have been demonstrated in such devices, and microfluidic arrays have been used for high throughput analysis. Such studies are important for numerous applications, including disease diagnosis, prognosis, treatment and drug testing. Below, a brief review of cell capture in microfluidic devices is presented, highlighting the main methods that are currently used.

Electrical methods have been used for cell separation and immobilization. They are mainly based on dielectrophoresis, during which a force is applied on the cells under an inhomogeneous electric field. Differences in the induced polarizability of the cells and the medium lead to the movement of the cells towards the higher electric field (p-DEP) or the lower electric field (n-DEP)[11]. The effective separation and trapping of viable and dead cells have been demonstrated by

several different electrode geometries [12, 13]. Single cell capture has also been shown to be effective using this method [14, 15], with the advantage of easy release of part or all of the captured cells.

Magnetic methods have also been used for cell trapping. For that to be accomplished, cells are bound and interact with magnetic particles, including nanowires and microbeads [16, 17]. The simplest way for magnetic manipulation is using external magnets, however more complicated devices have also been shown that include micro coils and layers of gold wires[18]. Time varying electromagnetic fields can also transport magnetic particles, for applications in cell separation.

Optical and acoustic manipulation of cells is normally used for non-contact immobilization of cells [19, 20]. Optical tweezers is a well-known method during which a laser beam traps and moves a particle or a cell. The advantage is that it can have very high precision; however overheating is likely to happen leading to cell death. On the contrary, acoustic waves do not seem to have such a result even for long term cell handling. Here, the cell movement depends on the acoustic contrast factor which is a function of the properties of both the cell and the solution.

Chemical patterning of surfaces has been shown advantageous for cell manipulation.[11, 21-23] The microchannel walls can be coated with cell adhesion molecules like fibronectin for cell enrichment[24], or be decorated with antibodies in order to capture rare cells, like circulating tumor cells (CTCs), from a cell population[21, 22]. The cells, then, are selectively adhered on the surface of the device depending on the cell surface properties. Chemical patterning for fabrication of adhesive islands has also been demonstrated for cell isolation at a specified compartment or to study the cell shape [25]. Although this method is a rather traditional one, it is not always optimal, especially if non-adherent cells are to be tested, or if reversible deposition of cells is necessary.

Another method for in-contact cell capture is using hydrodynamic trapping. The researchers take advantage of the dimensions of the microchannel using micro wells or micro

features to sieve the cells out of the suspension [26-29]. This is accomplished using dams that separate the channel into two smaller ones, or using structures with gaps smaller than the cells to immobilize them and permit only the flow of the fluid. Arrays of microwells have also successfully trapped single or multiple cells for subsequent culture and imaging. It has been proven that the number of cells captured with this method depends mainly on the dimensions of the structures [30, 31].

Methods for cell capture solely applied in microfluidic channels have been demonstrated using microfluidic valves, and microvortices. For example, Wang et al demonstrated the use of a microfluidic valve to seal individual compartments within the device that were filled with cells. Once the seal is introduced, the chamber is isolated and the rest of the solution flows through a bypass channel [32]. In another work, microvortices were created at specific flow rates due to backward facing steps on the side walls of the microchannel. The cells get trapped in the vortices while the rest of the fluid passes by, and they can be released if the flow rate decreases[33].

5.1.2 Isolation of specific areas in the microfluidic device

The fabrication of microfluidic devices is performed by soft lithography based on PDMS (polydimethylsyloxane). This method produces identical devices at low cost, and has the capability of producing multilayer devices. Typically, only one of these layers forms the fluidic channel, where the main experiment takes place, and the additional ones accommodate the so-called microfluidic valves. When pressure is applied on the microfluidic valves, a thin PDMS membrane inbetween two layers deforms, and blocks the flow in the fluidic layer[34].

Microfluidic valves are very important on μTAS devices. They are mainly used to isolate different areas of the device into compartments with distinct functions[35, 36]. Moreover, partial closure of the valve, can lead to trapping of μm-sized beads or cells[5]. Advancement of the field of microfluidics has led to the generation of more complicated applications, which require

sophisticated architectures of the microfluidic devices. Highly complex microfluidic features and devices can cause issues with the fabrication procedure, and handling by trained experts might be necessary, as fractures and breakage of the device become more likely. For example, White et al demonstrated a microfluidic device for lysis and genetic analysis of cells, by performing dilution of the initial sample, to subsequent bigger chambers, leading to an overall complicated device[37]. On another report, large-scale integration of microfluidic valves was used for the formation of confined picoliter chambers[38]. The downside of these methods is the complexity of the devices, which requires careful manipulation and very good alignment during fabrication.

Even though, miniaturization of a process is one of the main characteristics of microfluidics, this isn't necessarily accompanied with miniaturization of the architecture of the device. The distinctive dimensions found in this field, can give rise to novel, uncomplicated and straightforward approaches with additional advantages, and increased efficiency. In this chapter, a simple method for chamber formation in microfluidic systems is demonstrated. We envision that such a method will be implemented on integrated devices, for single cell analysis, and digital PCR.

5.2 MATERIALS AND METHODS

5.2.1 TRAP FABRICATION

The hydrodynamic traps on the microfluidic chip were made out either of PDMS or SU-8 2025 photoresist. For the first case, multilayer soft lithography based on PDMS was used (Appendix A). A chrome mask was used for the fabrication of the master, to effectively generate the small features (<20 μm). The PDMS traps were molded by the master, along with the rest of the features of the channel, and they were 25 μm tall (i.e. the channel was 25 μm deep). The PDMS

was later bonded with a precleaned glass slide. On the second case, hydrodynamic traps were photolithographically patterned on precleaned glass slides by SU-8. Chrome mask was still necessary for the reproducible generation of the small features. The height of the traps was controlled by the spin rate that was used after the deposition of the photoresist on the glass substrate, and it ranged from 20 μm to 30 μm. The fluidic and control layers of the channel were made out of PDMS (Appendix A). The patterned glass and the molded 2-layer PDMS were carefully aligned before plasma bonding. The device in figure 5.1A holds 400 hydrodynamic traps in total.

5.2.2 CELL PREPARATION

HEK cells were washed with PBS by centrifugation at 300g for 5 minutes. The cells were resuspended in PBS buffer at a concentration of 10^6 cells ml^{-1}, which was determined by a hemocytometer.

5.2.3 DEVICE OPERATION

The fabricated microfluidic device from figure 5.1A was mounted on an inverted fluorescence microscope (IX-71, Olympus, Melville, NY). The control layer was connected to N_2 gas for pneumatic actuation of the microfluidic valves, which were controlled by a computer. Otherwise, the control channels were connected to a tubing and a syringe filled with water, to manually actuate the valves. The experimental process was captured using a CCD camera (ORCA-285, Hamamatsu, Bridgewater, NJ) and a 10x dry objective. The fluidic layer of the device was first flushed with PBS buffer to remove all air bubbles. Then, water was inserted into the control channels from the single reservoir, until all bubbles were diffused out through the gas permeable PDMS. 10 μl of cell suspension flowed through the fluidic layer at a rate of 10 μl/min for single cell trapping. PBS buffer flowed through the device afterwards to flush out the non-specifically

trapped cells. After that, the control valves were pneumatically actuated to form individual chambers around each trap.

5.3 RESULTS AND DISCUSSION

The 2-layer PDMS device, shown in figure 5.1A, was used during the experiments of this project. The fluidic layer consists of four columns with a single inlet and two outlets (i.e. two columns share one outlet). Each column holds 100 hydrodynamic traps (Fig. 5.1B, 5.1C) that share a dual role; they are used to immobilize single cells, and they act as pillars for the formation of individual chambers. On top of this channel, two separate, control channels with a single reservoir each (i.e. control valves), lye on the control layer. When the control valves are pressurized, the thin PDMS membrane inbetween the two layers deforms, leading to the formation of chambers around the traps (Fig. 5.2C). We will analyze each part of the device separately, starting from the hydrodynamic traps.

Figure 5.1B shows a schematic of two traps. Each of them measures 60 μm x 30 μm in total in the x-y plane, and is 22.5 μm tall. The feature consists of three separate structures that leave two gaps of 6.5 μm. When the trap is empty, the streamlines of the fluid flow through these gaps, dragging along the cells in the suspension (top left trap of figure 5.1B). Because the cell diameter is bigger than the gap width (measuring 13 μm and 6.5 μm respectively), a cell is eventually immobilized at the physical barrier. The gaps of the trap are now physically blocked by the cell, altering the fluid flow (bottom right trap of figure 5.1B). The streamlines bypass the occupied trap, dragging the rest of the cells to other free traps downward the device.

Different trap sizes and designs were tested, to optimize the cell trapping technique. The architecture of the trap ranged from a single-structure, to three- and four- structure features. This variation lead to different flow profiles through and around the traps that affected the trapping efficiency. Typically, the more the fluid that flowed through the trap, the better the performance of the trap, with the limitation of having the gap size smaller than the cell diameter. For the case of a single-structure feature, the trap was fabricated to be shorter than the channel depth, to allow the streamlines of the flow to pass on top of empty traps. The problem of that technique, was that the cells would often stretch and squeeze through the fairly big gap, escaping from the trap. Although, the four-structure feature allowed more fluid to flow through, it also created difficulties during the fabrication procedure, due to the very small structures. The best set of characteristics, in terms of ease of fabrication and trapping efficiency, belonged to the three-structure features, with a height that was shorter than the channel depth (Fig. 5.1B, C).

The traps were designed to carry a basin upstream, to facilitate the immobilized cells. The number of trapped cells was strongly affected by the basin size. More specifically, a width of 20 μm was found to be the ideal for single cell trapping. Bigger width lead to multiple cell entrapment, and smaller width lead to increased number of empty traps. Even though cell populations are inhomogeneous, small variations in cell size didn't seem to affect the single cell trapping efficiency. The flow rate and cell concentration were systematically characterized and optimized. For the examined parameters, we observed, that the marginal traps of a very wide channel, would always remain empty. A narrow column with 4 to 6 traps was found to be optimal, permitting a 95% efficiency of single cell trapping.

The additional role of the hydrodynamic traps was to support the chamber formation process. Pneumatic actuation of the controlled chamber, squeezed the thin PDMS membrane,

which was located between the two layers, towards the glass slide (Fig. 5.2C). This time, each feature acted as a pillar to facilitate the creation of an individual compartment around it. The architecture and dimensions of the trap determined the volume of the chamber. Specifically, we calculated that the traps of figure 5.1A generated a 300 pl chamber (determined by fluorescent images, similar to figure 5.3) . The distance between adjacent traps was also important. If it was too small, this would jeopardize the complete sealing of a compartment, leading to leakage between chambers. On the other hand, much higher distance would decrease the trapping efficiency, allowing the streamlines to bypass the empty traps. As a solution, we ensured that the rows of the trap array were not aligned in the vertical direction. This way, the distance between neighboring traps was magnified, for a given length between two rows, allowing the formation of perfectly sealed individual chambers, and excellent single cell trapping efficiency.

Traps of different materials were tested. Initially, PDMS traps were fabricated, due to the ease of fabrication. Their ability to form solid pillars was investigated, by adding fluorescein solution in the chamber. After actuation of the control channel, fluorescein outlined the newly formed chambers, and permitted their visualization. Figure 5.3 shows that the pressurized control layer deformed the elastic PDMS pillars, prohibiting the generation of the picochamber. On the contrary, if the traps were made out of negative photoresist SU-8, the chamber could be supported by the strong, solid pillars.

The control layer of the device was consisted of two big chambers with a single reservoir each. This very simple architecture could easily facilitate the chamber formation in the fluidic layer. Due to the dimensions of the control channel (900 μm long and 500 μm wide), pillars (with a diameter of 30 μm) had to be added, to ensure that it wouldn’t collapse. Fabrication of a separate

control channel per one fluidic column was redundant, and would create unnecessary additional reservoirs, that would only add to the complexity of the device. On the other hand, the chamber would be too big, had it controlled all four fluidic columns, increasing the sensitivity of the device towards potential fractures. We concluded, that one control channel per two fluidic columns was optimal. Additionally, the thickness of the PDMS membrane between the two layers was characterized, and optimized at 100 μm. Thicker membrane lead to incomplete compartmentalization of the fluidic layer, though a thinner one could be easily broken.

An important advantage of our method, is the ability to reverse the chamber formation process. Removal of the additional pressure in the control layer, unifies the fluidic channel once more. The sample, now, can be washed out from the device for off-chip analysis. We anticipate that this device will be used for single cell analysis, and on-chip PCR. For example, the cells initially can be trapped in a single cell manner, and washed with the PCR master mix. Actuation of the valves leads to the entrapment of the cells in individual chambers, which facilitates the single cell PCR. After the on-chip analysis, the amplified product may be flushed out from the device for sequencing. Single cell PCR will completely rule out the PCR bias that exists in multi-template samples (samples with more than one unique genomes)[39]. Moreover, this simple method for compartmentalization of the device may also find use in digital PCR[40]. In comparison to the previous example, this technique is also used to carry single genome PCR, with the difference that the cell lysis takes place off chip. Here, the pillars may be in the form of cylinders of small diameter (less than 10 μm) to facilitate the formation of chambers with tiny volume, in an easy way.

5.4 CONCLUSION

In this chapter, we demonstrate a simple method for creating chambers in a microfluidic device. We show, that this technique can be used for enclosing single cells in individual compartments. Initially, the cells are immobilized by hydrodynamic traps that are located in the flow path of the fluidic layer. The small size of the traps ensures the trapping of single cells. After trapping, a control chamber that is located on top of the fluidic channel, is pressurized, squeezing down the thin PDMS membrane that is located between the two layers. The solid traps act as pillars, being responsible for the formation of chambers. The dual role of the traps (i.e. for cell trapping, and as pillars) ensures the entrapment of single cells in individual compartments. This is highly advantageous for studies regarding the inhomogeneity of cell populations, which require single cell analysis (e.g. single cell PCR). Additionally, the same simple method for chamber formation can be used for digital PCR, by decreasing the size of the pillars, which determines the volume of the chamber. The advantage of this method, is the reversibility of the compartmentalization of the device, if needed. After the on-chip analysis, the control chamber depressurizes, to create a unified channel once more, and the sample is flushed out for additional off-chip analysis (e.g. sequencing).

REFERENCES

1. G. M. Whitesides, *Nature*, 2006, **442**, 368-373.
2. Z. Cao, F. Chen, N. Bao, H. He, P. Xu, S. Jana, S. Jung, H. Lian and C. Lu, *Lab on a chip*, 2013, **13**, 171-178.
3. M. G. Lee, J. H. Shin, C. Y. Bae, S. Choi and J.-K. Park, *Analytical Chemistry*, 2013, **85**, 6213-6218.
4. E. Sollier, D. E. Go, J. Che, D. R. Gossett, S. O'Byrne, W. M. Weaver, N. Kummer, M. Rettig, J. Goldman, N. Nickols, S. McCloskey, R. P. Kulkarni and D. Di Carlo, *Lab on a chip*, 2014, **14**, 63-77.
5. T. Geng, N. Bao, N. Sriranganathanw, L. Li and C. Lu, *Analytical chemistry*, 2012, **84**, 9632-9639.
6. X. Chen, D. Cui, C. Liu, H. Li and J. Chen, *Analytica chimica acta*, 2007, **584**, 237-243.
7. J. Kim, M. Johnson, P. Hill and B. K. Gale, *Integrative Biology*, 2009, **1**, 574-586.
8. R. M. Johann, *Anal. Bioanal. Chem.*, 2006, **385**, 408-412.
9. A. Lawrenz, F. Nason and J. J. Cooper-White, *Biomicrofluidics*, 2012, **6**.
10. M. Leslie, *Science*, 2011, **331**, 24-26.
11. J. Nilsson, M. Evander, B. Hammarstrom and T. Laurell, *Analytica chimica acta*, 2009, **649**, 141-157.
12. G. H. Markx, M. S. Talary and R. Pethig, *J. Biotechnol.*, 1994, **32**, 29-37.
13. B. H. Lapizco-Encinas, B. A. Simmons, E. B. Cummings and Y. Fintschenko, *Electrophoresis*, 2004, **25**, 1695-1704.
14. B. M. Taff and J. Voldman, *Analytical Chemistry*, 2005, **77**, 7976-7983.

15. J. Voldman, M. L. Gray, M. Toner and M. A. Schmidt, *Analytical Chemistry*, 2002, **74**, 3984-3990.

16. M. Tanase, E. J. Felton, D. S. Gray, A. Hultgren, C. S. Chen and D. H. Reich, *Lab on a chip*, 2005, **5**, 598-605.

17. H. Lee, A. M. Purdon and R. M. Westervelt, *Appl. Phys. Lett.*, 2004, **85**, 1063-1065.

18. N. Pamme, *Lab on a chip*, 2006, **6**, 24-38.

19. X. B. Wei, B. J. Tromberg and M. D. Cahalan, *Proc. Natl. Acad. Sci. U. S. A.*, 1999, **96**, 8471-8476.

20. E. H. Brandt, *Nature*, 2001, **413**, 474-475.

21. A. A. Adams, P. I. Okagbare, J. Feng, M. L. Hupert, D. Patterson, J. Gottert, R. L. McCarley, D. Nikitopoulos, M. C. Murphy and S. A. Soper, *J. Am. Chem. Soc.*, 2008, **130**, 8633-8641.

22. S. L. Stott, C. H. Hsu, D. I. Tsukrov, M. Yu, D. T. Miyamoto, B. A. Waltman, S. M. Rothenberg, A. M. Shah, M. E. Smas, G. K. Korir, F. P. Floyd, A. J. Gilman, J. B. Lord, D. Winokur, S. Springer, D. Irimia, S. Nagrath, L. V. Sequist, R. J. Lee, K. J. Isselbacher, S. Maheswaran, D. A. Haber and M. Toner, *Proc. Natl. Acad. Sci. U. S. A.*, 2010, **107**, 18392-18397.

23. W. C. Chang, L. P. Lee and D. Liepmann, *Lab on a chip*, 2005, **5**, 64-73.

24. R. D. Lovchik, F. Bianco, M. Matteoli and E. Delamarche, *Lab on a chip*, 2009, **9**, 1395-1402.

25. M. Thery, V. Racine, A. Pepin, M. Piel, Y. Chen, J. B. Sibarita and M. Bornens, *Nat. Cell Biol.*, 2005, **7**, 947-U929.

26. D. Di Carlo, L. Y. Wu and L. P. Lee, *Lab on a chip*, 2006, **6**, 1445-1449.

27. M. S. Yang, C. W. Li and J. Yang, *Analytical Chemistry*, 2002, **74**, 3991-4001.

28. W. H. Tan and S. Takeuchi, *Proc. Natl. Acad. Sci. U. S. A.*, 2007, **104**, 1146-1151.

29. J. R. Rettig and A. Folch, *Analytical Chemistry*, 2005, **77**, 5628-5634.

30. L. Y. Wu, D. Di Carlo and L. P. Lee, *Biomed. Microdevices*, 2008, **10**, 197-202.

31. D. Di Carlo, N. Aghdam and L. P. Lee, *Analytical Chemistry*, 2006, **78**, 4925-4930.

32. H. Y. Wang, N. Bao and C. Lu, *Biosens. Bioelectron.*, 2008, **24**, 613-617.

33. C. M. Lin, Y. S. Lai, H. P. Liu, C. Y. Chen and A. M. Wo, *Analytical Chemistry*, 2008, **80**, 8937-8945.

34. M. A. Unger, H. P. Chou, T. Thorsen, A. Scherer and S. R. Quake, *Science*, 2000, **288**, 113-116.

35. D. N. Loufakis, Z. Cao, S. Ma, D. Mittelman and C. Lu, *Chemical Science*, 2014, **5**, 3331-3337.

36. S. Ma, D. N. Loufakis, Z. Cao, Y. Chang, L. E. K. Achenie and C. Lu, *Lab on a Chip*, 2014.

37. A. K. White, M. VanInsberghe, O. I. Petriv, M. Hamidi, D. Sikorski, M. A. Marra, J. Piret, S. Aparicio and C. L. Hansen, *Proceedings of the National Academy of Sciences*, 2011.

38. T. Thorsen, S. J. Maerkl and S. R. Quake, *Science*, 2002, **298**, 580-584.

39. P. S. Walsh, H. A. Erlich and R. Higuchi, *PCR methods and applications*, 1992, **1**, 241-250.

40. K. A. Heyries, C. Tropini, M. VanInsberghe, C. Doolin, O. I. Petriv, A. Singhal, K. Leung, C. B. Hughesman and C. L. Hansen, *Nat Meth*, 2011, **8**, 649-651.

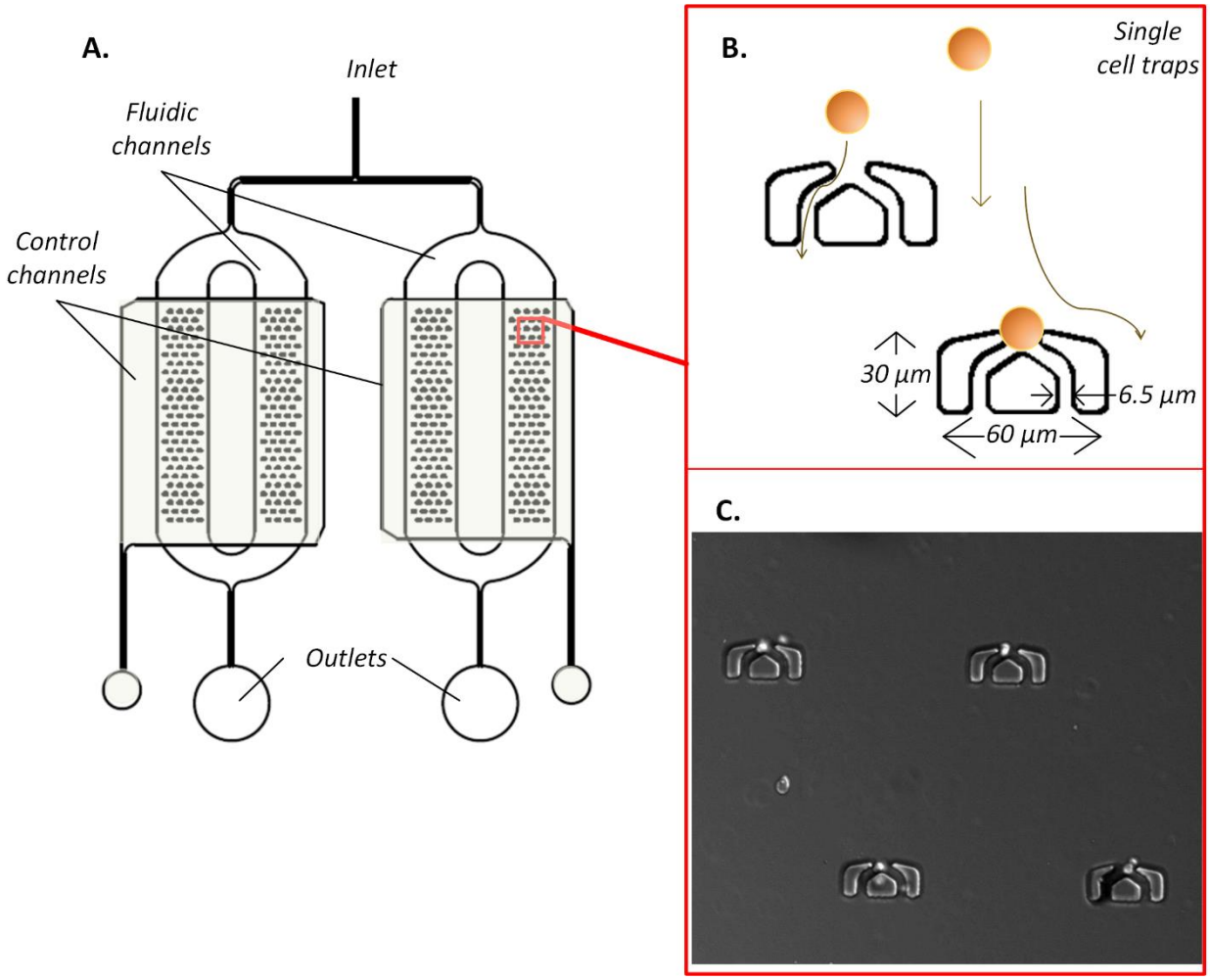

Figure 5.1. Illustration of the microfluidic device. A) The solution enters through a single inlet in the fluidic layer, and flows through the four columns that contain a total of 400 traps. Two big rectangular channels (shown in light grey) form the control layer of the device. B) Schematic representation of the hydrodynamic trap. The cells follow the streamlines, which flow through the two gaps in an empty trap. If the trap is occupied, then the streamlines surround it. C) Image of four individual occupied traps.

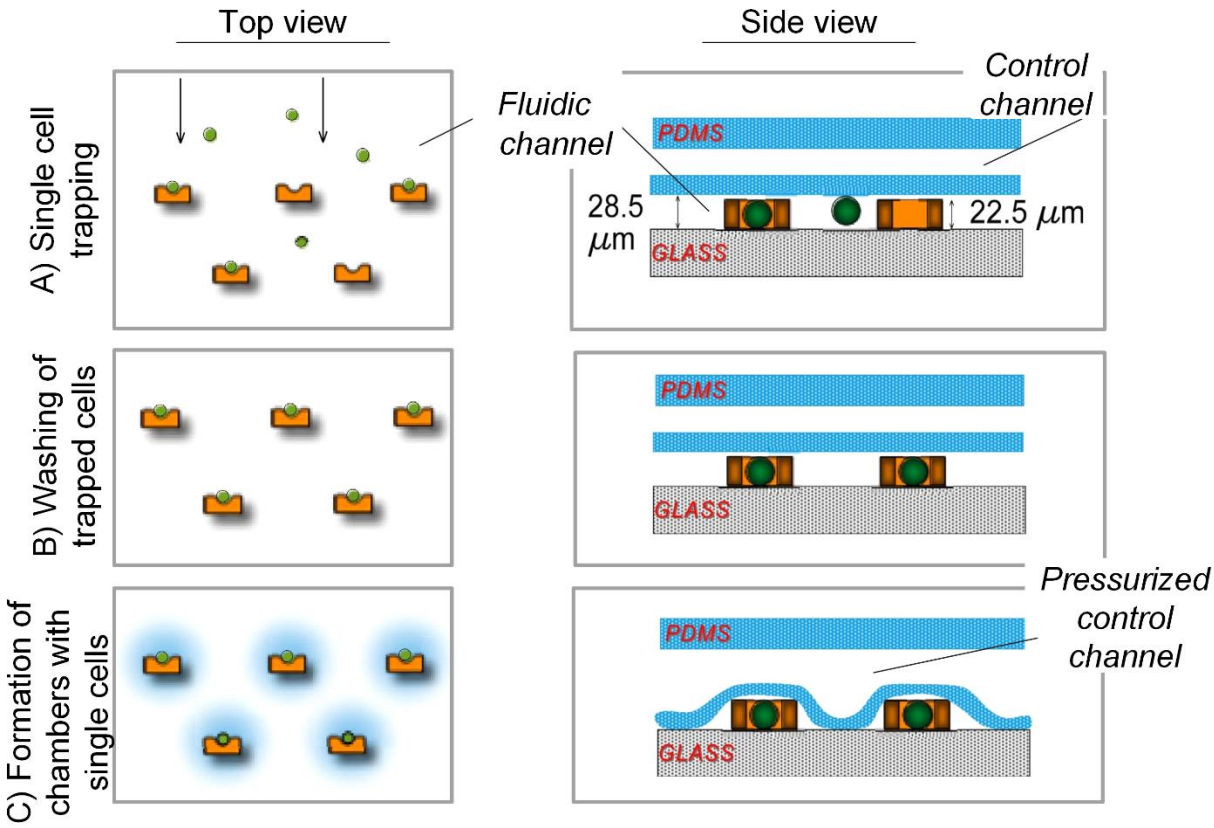

Figure 5.2. Schematic representation of the cell trapping in individual chambers. The top (left images) and side view (right images) of the device are shown. A) The cell solution flows through the fluidic layer of the device, and single cells get trapped. The control channel is depressurized. B) The control channel is still depressurized. A buffer is flushed through the fluidic layer to wash out the cells that are not specifically trapped. C) The control channel is pressurized, and the thin PDMS membrane inbetween the two layers is deformed. The traps act as pillars, and individual chambers are formed around each trap.

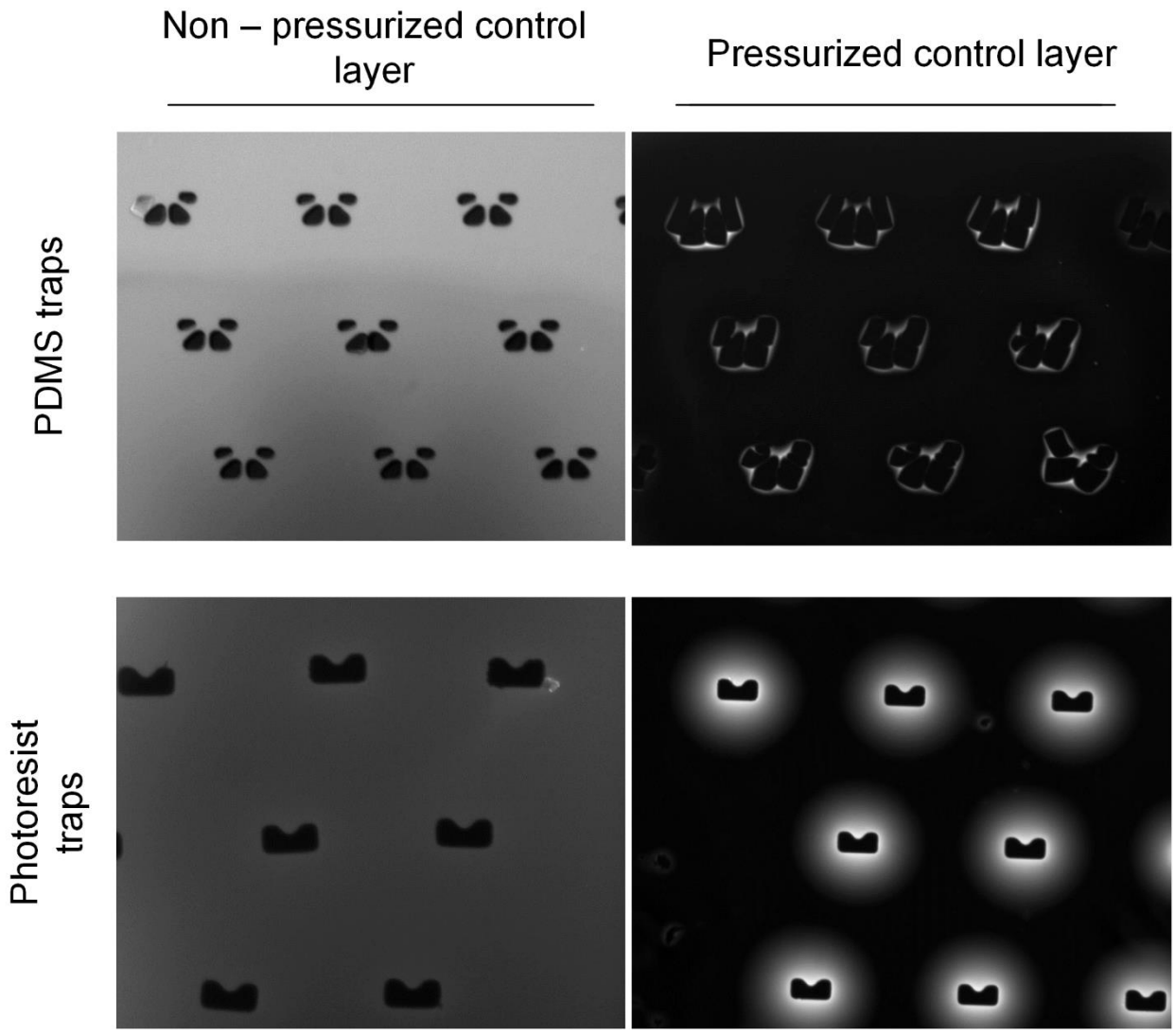

Figure 5.3. Images of the traps. The fluidic layer is filled with fluorescein solution. If the control layer is depressurized (images on the left), the fluidic chamber is a unified. However, if pressure is applied on the control layer, individual chambers are formed around each trap (images on the right). At the top and bottom set of images, the traps were made out of the elastomer PDMS, and photoresist SU-8 respectively.

CHAPTER 6 – HYDRODYNAMIC FOCUSING IN MICROFLUIDIC DEVICES FOR CONTROLLED SPATIAL DILUTION

6.1 INTRODUCTION

6.1.1 HYDRODYNAMIC FOCUSING

Hydrodynamic focusing is used in microfluidics as a tool to create a thin stream of the sample flow[1]. The laminar flow profile, that is present in microfluidic devices, ensures the generation of a multilayer flow in a microchannel with multiple inlets. Typically, side (sheath) flows squeeze the sample flow into a thin layer, the focusing width of which can be explicitly controlled by the flow rates and the geometry of the channel. The transport of molecules between the layers takes place only due to diffusion, due to the absence of turbulence. The restrain of the sample flow happens either in one axis (2-D hydrodynamic focusing)[2-4], or in both axes (3-D hydrodynamic focusing)[5-7], depending on the demands of each application.

Several lab-on-a-chip devices have been reported that take advantage of this technique. For example, Lu et al[5] demonstrated reproducible, and size-controlled synthesis of polyplexes, which showed better tranfection efficiency in comparison to the bulk-produced ones. The impressive results were attributed on the fact that the synthesis of the nanocomplexes was based on the well-controlled diffusion between the sample and side flows. On another example, Zhu et al[8] developed an electroporation chip, which allowed the electropermeation of yeast cells in the sample flow, by applying a voltage difference on the high conductivity sheath flows. Hydrodynamic focusing has

also shown critical improvements on flow cytometry applications. Mao et al[9] implemented 3-D hydrodynamic focusing to create a thin stream of cell suspension for downward laser detection in a microfluidic device. The vertical focusing of the sample was achieved in a curved channel. Dean flow was generated at the curve, which flipped the horizontally focused layer by 90 degrees. Additional horizontal focusing squeezed the solution further to a thin stream with a width similar to the size of single cells.

6.1.2 ERYTHROCYTE FRAGILITY

Erythrocytes or else red blood cells (RBCs) are present in the human blood, and are responsible for transporting oxygen and carbon dioxide throughout the body[10]. Their well-being in terms of shape, numbers and deformability is indicative of many diseases. For example, low RBCs count is diagnosed as anemia, which is associated with low quality of life[11]. Moreover, their irregular shape may be indicative of several blood disorders, such as sickle cell anemia[12] or spherocytosis[13, 14], during which the cells are shaped either like a crescent or a sphere respectively. They both cause hemolysis (i.e. lysis of RBCs), and they are responsible for severe pain and permanent organ damage.

A good indication of the RBCs health are the erythrocyte fragility tests, which detect the degree of susceptibility to hemolysis. Typically, red blood cells are highly flexible in order to easily move through the vessels of the body[15]. Decrease in their deformability has been linked with many diseases, such as diabetes mellitus, acute myocardial infarction and sickle cell anemia, and it is attributed to changes on the membrane structure and the membrane-cytoskeletal interactions[16-18]. For example, RBCs of diabetic patients have decreased resistance to oxidative agents, leading to increased oxidative lipid degradation, and decreased fluidity[19].

During erythrocyte fragility tests, RBCs are put under stress until they lyse. This stress may be stretching in atomic force microscopy (AFM) tests[20-22] or shear stress in rheoscopy methods[23, 24]. Osmotic fragility tests have also been reported, during which the RBCs are tested in the presence of hypoosmotic saline solutions[25, 26]. In all the cases, the percentage of lysed cells is plotted with respect to the stress agent, and the sample of interest is compared to a control group.

In this chapter, I present the computational study of the flow and concentration profiles of a microfluidic device with hydrodynamic focusing, which was used for erythrocyte fragility tests. The device was on a single layer, with three inlet streams and one outlet, for generation of 2-D hydrodynamic focusing. Diffusion between the layers resulted in changes in the concentration downward the device, which were responsible for RBC lysis. The effect of the ratio of the flow rates between the main and side flows was examined, as well as the effect of the proportional increase of all the flow rates. Correlation of the computational results with the experimental data, revealed good understanding of the physics. It is important to note that the laminar flow profile of the device, resulted in excellent reproducibility between different runs.

6.2 MATERIALS AND METHODS

6.2.1 COMSOL MULTIPHYSICS SIMULATIONS

The commercial CFD package COMSOL Multiphysics (4.0) was used to study the microfluidic channel shown in figure 1A. The modules “Laminar flow” and “Transport of Diluted Species” were coupled to solve for the velocity and concentration profiles of NaCl. A 2-D geometry in rectangular coordinate system was sufficient to produce accurate results. An “extremely fine” triangular surface mesh was generated, with minimum and maximum element

sizes equal to 1.36 μm and 15.7 μm respectively, and maximum element growth rate equal to 1.05. The total number of elements was 278,032.

The continuity equation (eqn. 1), the Navier-Stokes equation (eqn. 2) and the convection-diffusion transport equation (eqn. 3) were coupled and solved at steady state.

$$\nabla \cdot (\rho v) = 0 \qquad eqn.1$$

$$\rho(v \cdot \nabla v) = -\nabla P + \mu \nabla^2 v \qquad eqn.2$$

$$\nabla \cdot (-D\nabla \mathrm{c}) + v \cdot \nabla \mathrm{c} = 0 \qquad eqn.\ 3$$

where ρ is the density of the fluid, v is the velocity, P is the pressure, μ is the viscosity, D is the diffusion coefficient and c is the concentration.

The fluid was assumed to be incompressible, which simplified eqn. 1 to

$$\nabla \cdot v = 0 \qquad eqn.4$$

The boundary conditions for eqn. 2 were the known inlet velocities and concentrations, and an atmospheric pressure condition at the outlet. A no-slip boundary condition was also assumed at the walls of the channel. The inlet concentrations of the main and side streams were c_{NaCl} = 137mM and c_{NaCl} = 0mM respectively. The viscosity, and density of the fluid and the diffusion coefficient of NaCl are shown in table 6.1.

μ	8.925e-5 Pa s
ρ	998.2 kg m^{-3}
D_{NaCl}	1.49e-9 m^2 s^{-1}

Table 6.1. Constants used for the solution of the coupled equations in COMSOL Multiphysics

6.2.2 EXPERIMENTAL SETUP AND IMAGING

Multilayer soft lithography based on PDMS was used for the fabrication of the single-layer microfluidic device. Whole blood samples from healthy humans were purchased from Bioreclamation, Westbury, NY. The blood was washed three times with filtered phosphate buffer saline (PBS, Fisher Scientific, Suwanee, GA) by centrifugation at 1200g for 10 minutes. It was resuspended in PBS, and kept at 4^{o}C until used.

The chip was mounted on an inverted fluorescent microscope (IX-71, Olympus, Melville, NY) and a CCD camera (ORCA-285, Hamamatsu, Bridgewater, NJ) was used to capture the images. The images were later analyzed by a MATLAB program to detect erythrocyte lysis.

6.3 RESULTS AND DISCUSSION

The effect of hydrodynamic focusing on the concentration profiles of a microfluidic device was studied using COMSOL Multiphysics. The device was consisted of three inlets and one outlet, as shown in figure 6.1A. The length of the area of the device downstream the intersection (after the location x = 0mm as shown on the image), was 40mm and its width was 0.5mm. PBS solution entered the device through the main stream (sample flow) and water entered through the side streams (sheath flows). The laminar flow profile that was present in the microfluidic device, due to its dimensions, ensured that the mixing between the streams took place solely due to diffusion. We simulated the concentration profile of NaCl, which is the most abundant salt in PBS buffer (137mM), using COMSOL Multiphysics as discussed above. The microfluidic device was also tested experimentally for controlled red blood cell (RBC) lysis during the scope of a separate project, and some major results are discussed here for comparison with the computational data. The inset images of figure 6.1A show the phase contrast images of the RBCs at different lengths

of the device. At location a (x = 1.5mm) the erythrocytes are still intact, but at b (x = 13.5 mm) and c (x = 25.5 mm), their light intensity is decreased, due to the release of the intracellular material. At location d (x = 37.5 mm), the cells appear transparent, which indicates that they are lysed.

Snapshots of the simulated concentration profiles under different flow parameters are shown in figure 6.1B. The flow rates of the main and side streams are shown on the inset note of each image (the first number is the flow rate of the sample flow in μl min^{-1}, and the second number is the total flow rate of the sheath flows in μl min^{-1}). Two different sets of experiments were conducted. During the first one, the flow rate of the side streams increased from 0.6 μl min^{-1} to 3.6 μl min^{-1} in four steps, while the flow rate of the main stream remained the same. This increase created more rapid mixing and dilution in a given channel length. For example, the concentration of NaCl decreased by 15% at 12.5 mm downstream for the case that the flow rates were 0.1 – 0.6 μl min^{-1}. However, when the side flow rates were the highest (i.e. 0.1 – 3.6 μl min^{-1}), the decay of NaCl by 15% occurred at x = 2 mm. On the second set of experiments, the flow rates of all streams were increased proportionally, and ranged between 0.1 – 1.2 μl min^{-1} to 0.4 – 4.8 μl min^{-1} in four increments. In contrast to the previous runs, here, increase of the flow rates leads to slower mixing. Following the previous example, the same decrease of the concentration by 15% occurred at the earliest location (x = 4.9 mm) for the slowest flow rates (i.e. 0.1 – 1.2 μl min^{-1}), and at the farthest (x = 18.6 mm) for the fastest rates of 0.4 – 4.8 μl min^{-1}.

Next, we will analyze the focus width of the hydrodynamic focusing phenomenon. The size of it, is also a good indication of the mixing characteristics of the system at each flow condition. Figure 6.2 shows the concentration profile plots along the y-coordinate and at various locations downward the device. The location x = 0 mm is at the beginning of the intersection, as

shown in figure 6.1A, and the location x = 40 mm is at the end of the device. The plots at the left, show that, in general, higher side flow rates lead to narrower focus width. More specifically, for the first case scenario of 0.1 – 0.6 μl min^{-1}, the focus width was 320 μm, and it decreased to 210 μm, 136 μm, and 108 μm for the rest three cases of 0.1 – 1.2 μl min^{-1}, 0.1 – 2.4 μl min^{-1} and 0.1 – 3.6 μl min^{-1} respectively. The size of the focus width was determined by assuming a minimum concentration of 0.002 M. On the other hand, proportional increase of all flow rates lead to decreased focus width, from 210 μm at 0.1 – 1.2 μl min^{-1} to 116 μm at 0.4 – 4.8 μl min^{-1}. It is interesting to note, that the maximum concentration was also affected by the flow rates in the same trend. The reason is that the two findings are strictly related. For a given flow rate of the main stream, increase of the side flow rates, squeezes the main stream faster, leading to a narrower focus width at a given location. As a consequence, the diffusion length gets shorter, leading to faster mixing and dilution. On the other hand, increase of the flow rate of the main stream, corresponds to increase of the molar flow rate (assuming the same initial concentration), and as a result a higher peak concentration. A combination of the two aforementioned mechanisms contributes to the generation of concentration profiles of the plots on the right (i.e. proportional increase of all flow rates). As a result, the maximum concentration decreases from 0.046 M to 0.034 M, 0.025 M, and 0.02 M for increase of the side flow rates from 0.1 – 0.6 μl min^{-1}, to 0.1 – 1.2 μl min^{-1}, 0.1 – 2.4 μl min^{-1}, and 0.1 – 3.6 μl min^{-1} respectively, and it increases from 0.034 M, to 0.047 M, 0.05 M, and 0.064 M, if all the flows area increased from 0.1 – 1.2 μl min^{-1}, to 0.2 – 2.4 μl min^{-1}, 0.3 – 3.6 μl min^{-1}, and 0.4 – 4.8 μl min^{-1} respectively. By the end of the device (x = 40 mm), the final concentration profile varies within its y axis for 0.2 – 2.4 μl min^{-1}, 0.3 – 3.6 μl min^{-1}, and 0.4 - 4.8 μl min^{-1}, with the later showing the highest peak. This indicates, that the total length of the device

(40 mm) wasn't sufficient for complete mixing between the layers, for the specific flow parameters.

Using the computational data, we correlated the NaCl concentration along the length of the device (and at the center of the y-axis) with the corresponding experimental time. Figure 6.3 demonstrates that increase of the side flow rates from 0.6 μl min^{-1} to 3.6 μl min^{-1}, resulted to about 5 times faster, and 4.3 times higher final dilution. Each case showed a different correlation between the concentration and time. On the other hand, proportional increase of all side streams affected only the overall exposure time, without affecting its relationship with the concentration.

The microfluidic device was also tested experimentally to explore its capabilities, during the scope of a separate project. The most important results are presented here for comparison with the computational data. As stated before, the well predicted concentration profile, which varies along the x-coordinate due to diffusion, is ideal for controlled RBC lysis. The initial experimental results generated plots of the percent release of the intracellular material of RBCs with respect to the x-axis of the device (Fig. 6.4A, D). All the pairs of flow rates that were analyzed earlier, were also tested experimentally. As a general trend, it is observed, that increase of the flow rates, leads to reduced RBC lysis. For the first two flow parameters of the left plot (i.e. 0.1 – 0.6 μl min^{-1} and 0.1 – 1.2 μl min^{-1}), 100% release is observed downward the device, however for the other two cases the release reaches less than 50%. Similarly, at 6.3B, 100% release is only observed for the case of 0.1 – 1.2 μl min^{-1}. The percentage is the lowest for the case of 0.4 – 4.8 μl min^{-1}, which doesn't go above 20%. Both plots show very good reproducibility, which is indicative of the excellent control on the concentration profiles in the device.

On an effort to understand the main mechanism that causes the osmotic RBC lysis in the device, we hypothesized that both the time that the cells remain in the hypoosmotic buffer, and the

buffer's concentration are important. Using the computational data of figure 6.3, we plotted the experimental results with respect to the NaCl concentration and the exposure time. Comparison of figures 6.4B, and 6.4C show a more consistent relationship between the percent release and the cells exposure time, rather than with the concentration. This leads to the conclusion that the concentration is not the dominant cause for RBC lysis here, rather the exposure time is more important. However, if all the flow rates increase proportionally (Fig. 6.4E, 6.4F), the percent release data from these experiments show strong relationship with respect to both the concentration and the time. This was expected, since the concentration and exposure time are correlated with each other for this set of experiments (Fig. 6.3B).

6.4 CONCLUSION

In this chapter, we demonstrated a microfluidic device for osmotic lysis of erythrocytes. Hydrondynamic focusing was used to achieve controlled diffusion in the device, and create a hypoosmotic solution in terms of NaCl that lead to hemolysis. Computer simulations using COMSOL Multiphysics were performed to calculate the concentration profile of the system under different conditions. We varied the flow rates, in order to detect their effect on the concentration, by performing two different sets of experiments: a) we varied the flow rate of the side channels while keeping the flow rate of the middle stream the same, and b) we varied the flow rates of both the main and side streams in a proportionate fashion. Additionally, the computational results were compared and coupled with experimental data. Different runs of the experiments showed very good reproducibility, confirming the excellent control of the system's concentration profile, due to the diffusion under laminar flow. We envision that our technique will be beneficial on lab-on-chip devices for diagnosis of blood disorders.

REFERENCES

1. N. Nam-Trung and W. Zhigang, *Journal of Micromechanics and Microengineering*, 2005, **15**, R1.
2. A. Jahn, W. N. Vreeland, M. Gaitan and L. E. Locascio, *Journal of the American Chemical Society*, 2004, **126**, 2674-2675.
3. J. B. Knight, A. Vishwanath, J. P. Brody and R. H. Austin, *Physical Review Letters*, 1998, **80**, 3863-3866.
4. F. Wang, H. Wang, J. Wang, H. Y. Wang, P. L. Rummel, S. V. Garimella and C. Lu, *Biotechnology and bioengineering*, 2008, **100**, 150-158.
5. M. Lu, Y.-P. Ho, C. L. Grigsby, A. A. Nawaz, K. W. Leong and T. J. Huang, *ACS Nano*, 2013, **8**, 332-339.
6. C. Chih-Chang, H. Zhi-Xiong and Y. Ruey-Jen, *Journal of Micromechanics and Microengineering*, 2007, **17**, 1479.
7. H.-H. Hou, C.-H. Tsai, L.-M. Fu and R.-J. Yang, *Electrophoresis*, 2009, **30**, 2507-2515.
8. T. Zhu, C. Luo, J. Huang, C. Xiong, Q. Ouyang and J. Fang, *Biomedical microdevices*, 2010, **12**, 35-40.
9. X. Mao, S. C. Lin, C. Dong and T. J. Huang, *Lab Chip*, 2009, **9**, 1583-1589.
10. B. Alberts, *Molecular biology of the cell*, Garland Science, New York, 2002.
11. R. F. Paulson, *Nat Med*, 2014, **20**, 334-335.
12. P. van der Harst, W. Zhang, I. Mateo Leach, A. Rendon, N. Verweij, J. Sehmi, D. S. Paul, U. Elling, H. Allayee, X. Li, A. Radhakrishnan, S.-T. Tan, K. Voss, C. X. Weichenberger, C. A. Albers, A. Al-Hussani, F. W. Asselbergs, M. Ciullo, F. Danjou, C. Dina, T. Esko, D. M. Evans, L. Franke, M. Gogele, J. Hartiala, M. Hersch, H. Holm, J.-J. Hottenga, S.

Kanoni, M. E. Kleber, V. Lagou, C. Langenberg, L. M. Lopez, L.-P. Lyytikainen, O. Melander, F. Murgia, I. M. Nolte, P. F. O/'Reilly, S. Padmanabhan, A. Parsa, N. Pirastu, E. Porcu, L. Portas, I. Prokopenko, J. S. Ried, S.-Y. Shin, C. S. Tang, A. Teumer, M. Traglia, S. Ulivi, H.-J. Westra, J. Yang, J. Hua Zhao, F. Anni, A. Abdellaoui, A. Attwood, B. Balkau, S. Bandinelli, F. Bastardot, B. Benyamin, B. O. Boehm, W. O. Cookson, D. Das, P. I. W. de Bakker, R. A. de Boer, E. J. C. de Geus, M. H. de Moor, M. Dimitriou, F. S. Domingues, A. Doring, G. Engstrom, G. Ingi Eyjolfsson, L. Ferrucci, K. Fischer, R. Galanello, S. F. Garner, B. Genser, Q. D. Gibson, G. Girotto, D. Fannar Gudbjartsson, S. E. Harris, A.-L. Hartikainen, C. E. Hastie, B. Hedblad, T. Illig, J. Jolley, M. Kahonen, I. P. Kema, J. P. Kemp, L. Liang, H. Lloyd-Jones, R. J. F. Loos, S. Meacham, S. E. Medland, C. Meisinger, Y. Memari, E. Mihailov, K. Miller, M. F. Moffatt, M. Nauck, M. Novatchkova, T. Nutile, I. Olafsson, P. T. Onundarson, D. Parracciani, B. W. Penninx, L. Perseu, A. Piga, G. Pistis, A. Pouta, U. Puc, O. Raitakari, S. M. Ring, A. Robino, D. Ruggiero, A. Ruokonen, A. Saint-Pierre, C. Sala, A. Salumets, J. Sambrook, H. Schepers, C. Oliver Schmidt, H. H. W. Sillje, R. Sladek, J. H. Smit, J. M. Starr, J. Stephens, P. Sulem, T. Tanaka, U. Thorsteinsdottir, V. Tragante, W. H. van Gilst, L. Joost van Pelt, D. J. van Veldhuisen, U. Volker, J. B. Whitfield, G. Willemsen, B. R. Winkelmann, G. Wirnsberger, A. Algra, F. Cucca, A. P. d/'Adamo, J. Danesh, I. J. Deary, A. F. Dominiczak, P. Elliott, P. Fortina, P. Froguel, P. Gasparini, A. Greinacher, S. L. Hazen, M.-R. Jarvelin, K. Tee Khaw, T. Lehtimaki, W. Maerz, N. G. Martin, A. Metspalu, B. D. Mitchell, G. W. Montgomery, C. Moore, G. Navis, M. Pirastu, P. P. Pramstaller, R. Ramirez-Solis, E. Schadt, J. Scott, A. R. Shuldiner, G. Davey Smith, J. Gustav Smith, H. Snieder, R. Sorice, T. D. Spector, K. Stefansson, M. Stumvoll, W. H. Wilson Tang, D. Toniolo, A. Tonjes, P. M. Visscher, P.

Vollenweider, N. J. Wareham, B. H. R. Wolffenbuttel, D. I. Boomsma, J. S. Beckmann, G. V. Dedoussis, P. Deloukas, M. A. Ferreira, S. Sanna, M. Uda, A. A. Hicks, J. Martin Penninger, C. Gieger, J. S. Kooner, W. H. Ouwehand, N. Soranzo and J. C. Chambers, *Nature*, 2012, **492**, 369-375.

13. S. W. Eber, J. M. Gonzalez, M. L. Lux, A. L. Scarpa, W. T. Tse, M. Dornwell, J. Herbers, W. Kugler, R. Ozcan, A. Pekrun, P. G. Gallagher, W. Schroter, B. G. Forget and S. E. Lux, *Nat Genet*, 1996, **13**, 214-218.
14. F. Delhommeau, T. Cynober, P. O. Schischmanoff, P. Rohrlich, J. Delaunay, N. Mohandas and G. Tchernia, *Natural history of hereditary spherocytosis during the first year of life*, 2000.
15. M. Diez-Silva, M. Dao, J. Han, C. T. Lim and S. Suresh, *MRS bulletin / Materials Research Society*, 2010, **35**, 382-388.
16. M. Garnier, J. R. Attali, P. Valensi, E. Delatour-Hanss, F. Gaudey and D. Koutsouris, *Metabolism*, 1990, **39**, 794-798.
17. A. Vayá, M. Martinez, J. Garcia and J. Aznar, *Thrombosis Research*, 1992, **66**, 223-229.
18. M. Bryszewska, C. Watala and W. Torzecka, *British Journal of Haematology*, 1986, **62**, 111-116.
19. S. I. Rizvi and P. K. Maurya, *Annals of the New York Academy of Sciences*, 2007, **1100**, 373-382.
20. M. Radmacher, in *Methods in Cell Biology*, eds. W. Yu-Li and E. D. Dennis, Academic Press, 2007, vol. Volume 83, pp. 347-372.
21. I. Dulińska, M. Targosz, W. Strojny, M. Lekka, P. Czuba, W. Balwierz and M. Szymoński, *Journal of Biochemical and Biophysical Methods*, 2006, **66**, 1-11.

22. M. N. Starodubtseva, T. G. Kuznetsova, S. A. Chizhik and N. I. Yegorenkov, *Micron*, 2007, **38**, 782-786.

23. B. Avishay, K. Natanel, L. Alexander, L. Naomi, N. Yael and D. Uri, *Rheol Acta*, 2007, **46**, 621-627.

24. J. G. G. Dobbe, G. J. Streekstra, M. R. Hardeman, C. Ince and C. A. Grimbergen, *Cytometry*, 2002, **50**, 313-325.

25. E. Beutler, W. Kuhl and C. West, *Blood*, 1982, **59**, 1141-1147.

26. A. K. Parpart, P. B. Lorenz and et al., *The Journal of clinical investigation*, 1947, **26**, 636-640.

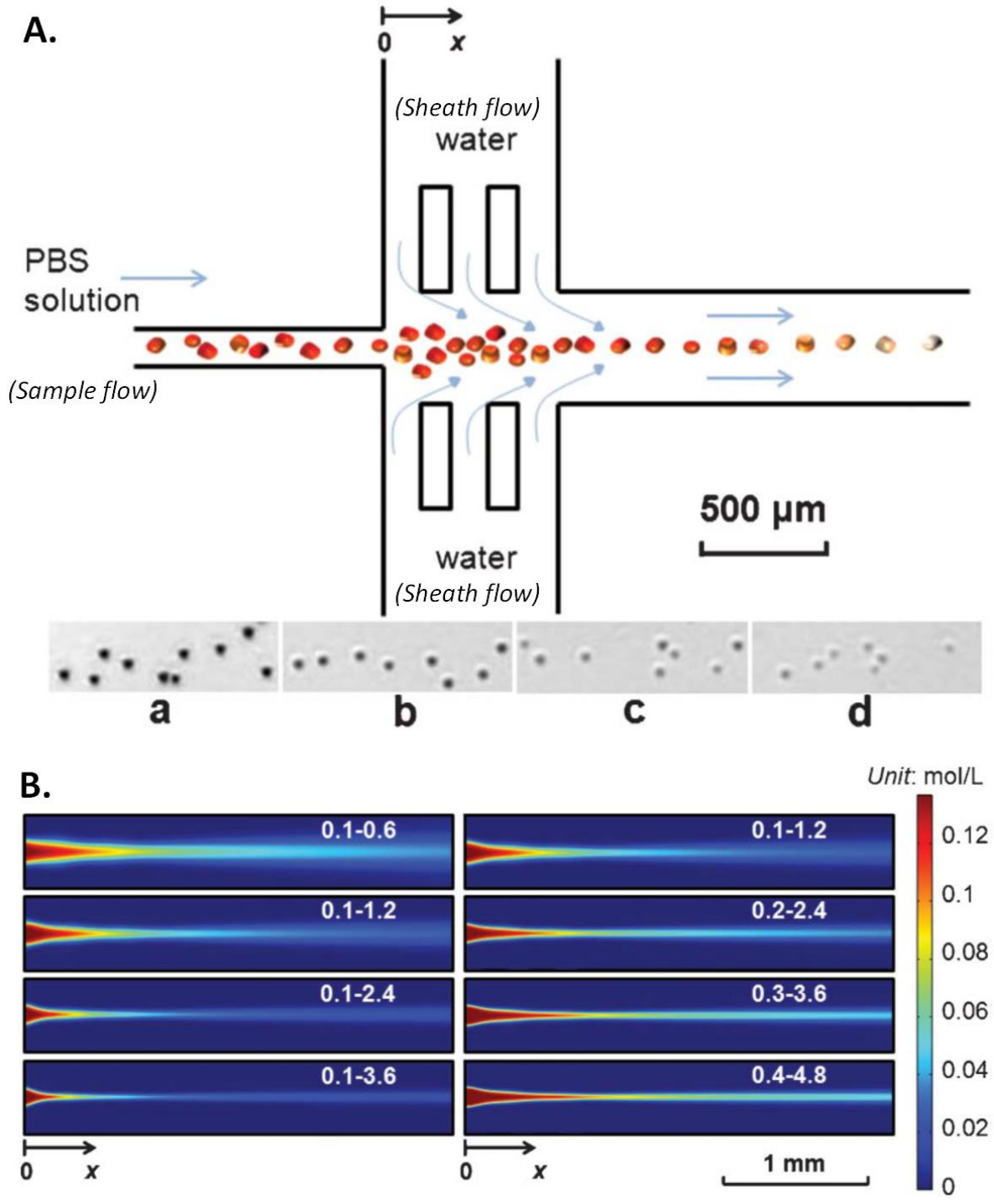

Figure 6.1. The hydrodynamic focusing. A) Schematic representation of the device. The sample flow enters through the central stream and is squeezed by two sheath flows. The concentration of the solution changes downward the device, leading to osmotic RBC lysis. The inset images show

RBCs under phase contrast at various locations downward the device (a: x = 1.5 mm; b: x = 13.5 mm; c: x = 25.5 mm; d: x = 37.5 mm). The light intensity of the erythrocytes varies due to release of intracellular material. B) The concentration profile, as it is shaped after hydrodynamic focusing. Different pairs of flow rates were used for the central and side streams, as it is shown on the top right corner of each image (the first number indicates the flow rate of the main stream, and the second number is the total flow rate of the side streams). The flow rate of the main stream varies from 0.1 μl min^{-1} to 0.4 μl min^{-1} and the total flow rate of the sheath flow vary from 1.2 μl min^{-1} to 4.8 μl min^{-1}. The concentration profile was modeled by COMSOL Multiphysics.

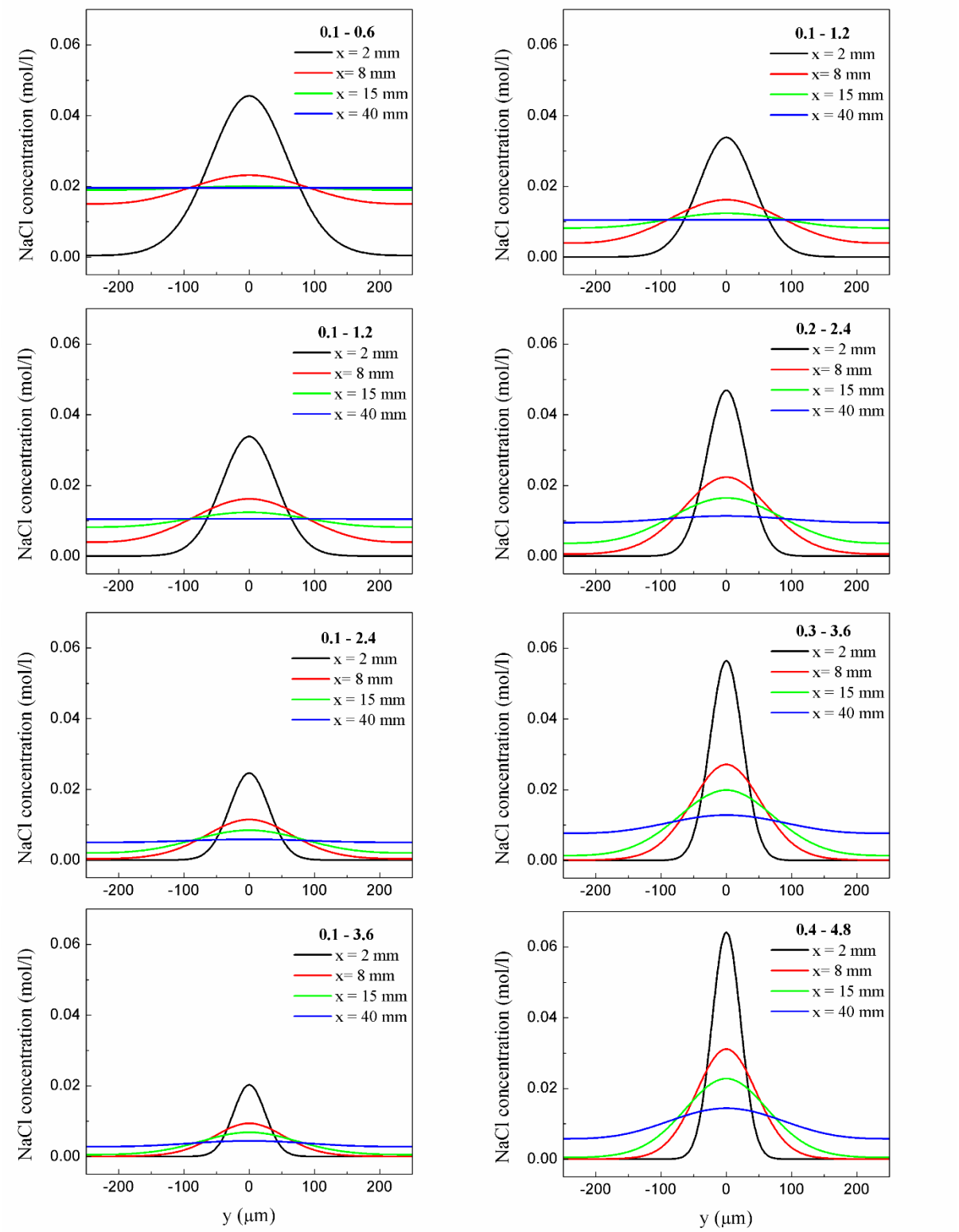

Figure 6.2. The NaCl concentration profile along the y axis at different positions downward the length of the device (x = 2 mm; x = 8 mm; x = 15 mm; x = 40 mm), and under various flow

conditions modeled by COMSOL Multiphysics. On the plots on the left, the flow rate of the main stream is always at 0.1 μl min^{-1}, while the total flow rate of the side streams varies from 0.6 μl min^{-1} to 3.6 μl min^{-1}. On the right, the flow rate of all streams increase proportionally and varies from 0.1-1.2 μl min^{-1} to 0.4-4.8 μl min^{-1}.

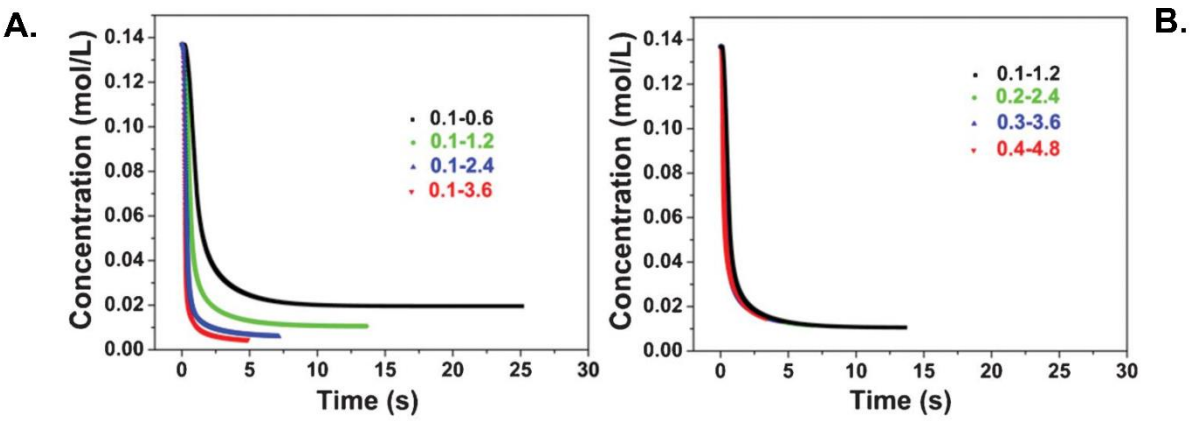

Figure 6.3. Data for the concentration profile with respect to the time were extracted from the COMSOL Multiphysics simulations A) The flow rate of the side streams increased from 0.6 µl min^{-1}, to 1.2 µl min^{-1}, 2.4 µl min^{-1} and 3.6 µl min^{-1} while the flow rate of the main stream was constant at 0.1 at all cases. B) The flow rates of all streams increased proportionally from 0.1 – 1.2 µl min^{-1} to 0.2 – 2.4 µl min^{-1}, 0.3 – 3.6 µl min^{-1} and 0.4 – 4.8 µl min^{-1}.

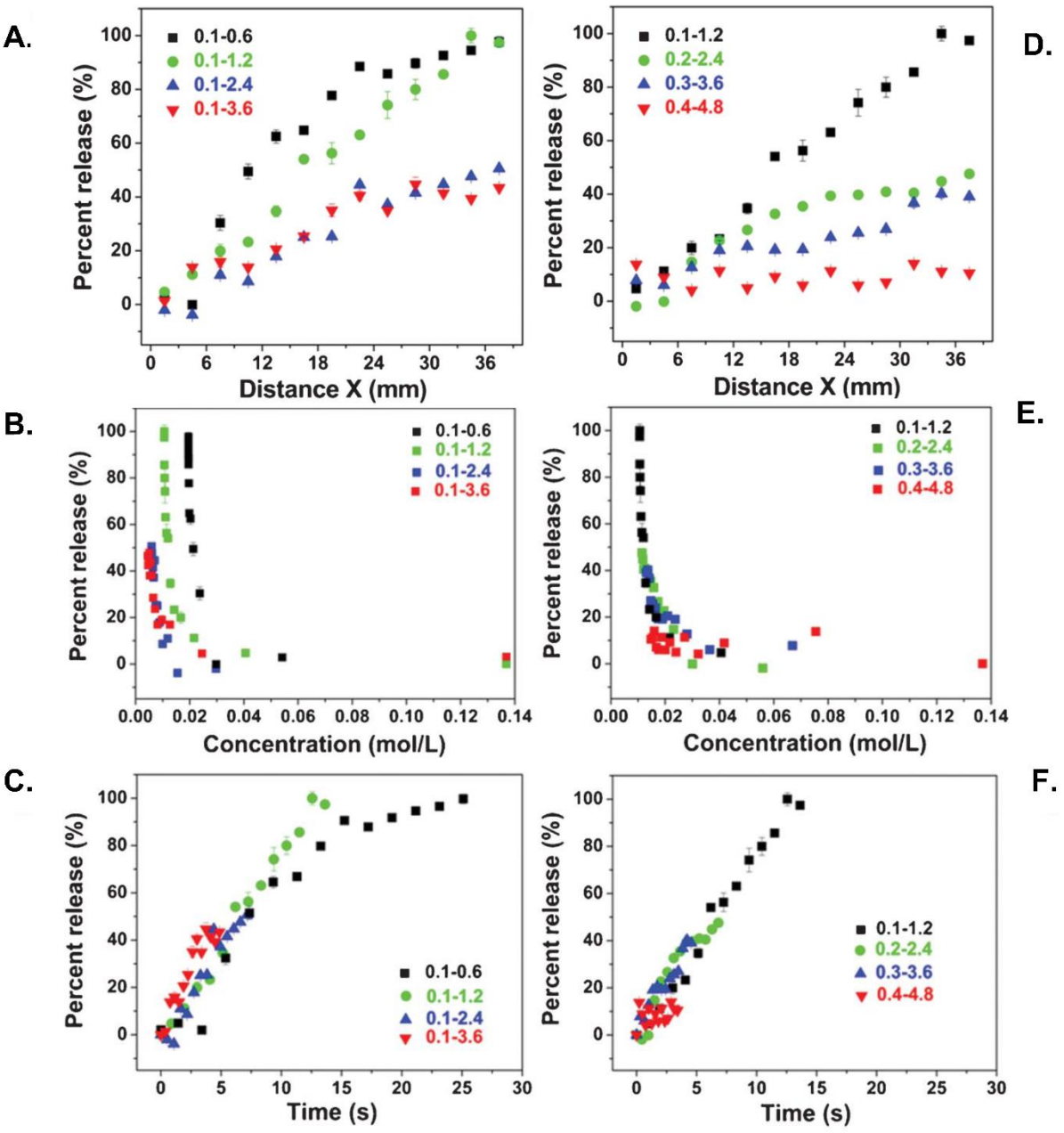

Figure 6.4. Experimental results of the percent release of intracellular material from RBCs while they flow through the microfluidic device. The results were plotted with respect to the location along the x-coordinate of the device (A,D), the concentration (B, E) and the time (C, F). The results were obtained for two different sets of flow velocity ratios, increasing only the sheath flow velocity (A, B, C), and increasing the sample and the sheath flows proportionally (D, E, F).

CHAPTER 7 – CONCLUSIONS

This dissertation was focused on the development of novel microfluidic methods for the manipulation and analysis of biological cells. The studies were performed on a microfluidic platform. Microfluidic channels are ideal for studying biological samples, mainly due to their characteristic dimensions (~hundreds of μm), which are comparable to the size of cells (e.g. diameter of mammalian cells ~ 10-20 μm). The thesis is divided into two general categories; the first group explores the capabilities of cell manipulation and analysis with the integration of electrical fields into the system, while in the second category, the development of novel methods arises from the manipulation of the architecture of the microchannels and the corresponding flow profiles that are developed in the system. The novelty and the unique contributions that our methods provide to the scientific community, are summarized in the following lines.

At Chapter 2, a novel method for focusing mammalian cells is presented. This is based on the generation of a high pH gradient that takes place in a confined microfluidic chamber due to the effect of water electrolysis during electrical pulses. Mammalian cells that are present in the system, experience a change in their cell surface charge, due to the pH change in their environment. As a result, the electrophoretic mobility of the cells is affected, leading to a change in their directionality. After the completion of several pulses, the cells appear focused in a narrow area close to the center of the chamber, at which location they experience a neutral surface charge. The method is similar to isoelectric focusing (IEF) that is normally performed for the separation of

proteins. IEF is typically performed in a gel that incorporates carrier ampholytes for the generation of a pH gradient, and the separation is completed by the application of an electric field. Although, IEF of small bioparticles (diameter < 5 μm) and in low concentrations has been demonstrated, IEF of mammalian cells (diameter ~ 10 μm) in such a system is much harder, due to possible blockage of the cells in the gel matrix. Our approach, is the first microfluidic method that is reported for concentration of mammalian cells in free solution due to IEF. In comparison to other methods for cell concentration in a microfluidic scheme (such as dielectrophoresis, hydrodynamic trapping, or chemical treatment of the cell surface), our method does not require complicated geometries of the chamber or the electrodes.

On the next chapter, a novel and simple device for DNA extraction from cells and subsequent DNA analysis is demonstrated. The integrated microfluidic device has the capability of performing cell lysis and PCR amplification on the same reaction chamber. Initially, DNA is released from mammalian cells during irreversible electroporation, with the application of high intensity electrical pulses. The implementation of this "clean" method for cell lysis, allows the elimination of the step of DNA purification, which typically takes place before DNA analysis. This is a great breakthrough on the on-chip analysis of DNA. The reason is, that the integration of the DNA purification step (which is typically necessary in the conventional methods for cell lysis with chemical reagents), often requires the incorporation of other materials on the chip (such as a filter), resulting to an overall highly complex, and expensive microfluidic device. In contrast to these alternative methods, our scheme allows the analysis of DNA (with on-chip PCR) immediately after the DNA extraction, on a simple microfluidic chip.

The effect of shear stress that is generated in microchannels, on the electroporation efficiency was examined in chapter 4. On two separate sets of experiments, cells in suspension and

attached cells were electroporated, while varying the shear stress profile in the channel. The experiments showed, that increase in the flow rate (and therefore increase of the magnitude of the shear stress) during electroporation results in enhanced delivery of extracellular molecules to the cells. Although the exact mechanism that underlies this process was not examined here, it is suspected that the shear stress intensified the generation of pores on the cell membrane during electroporation. Additionally, it was determined that the attached cells were more susceptible to the effect of shear stress in comparison to cells in suspension. This was expected, because their fixed location allowed a better control of the stress they experienced. This study has been the first attempt for a systematic characterization of the effect of the fluid flow on mammalian cells during electroporation. The results add significant value to the continuous effort for improvement of electroporation protocols.

Chapter 5 explores the capabilities of a microfluidic system for "smart" and reversible compartmentalization of a channel. Specifically, it was demonstrated that solid structures in the fluidic channel may act as pillars to support the formation of chambers around them, when pressure is applied on a secondary layer on top. These structures may even hold a dual nature, and also act as hydrodynamic traps, to entrap mammalian cells in a single cell manner. As a result, after compartmentalization of the fluidic layer, each cell is entrapped in an individual chamber, which acts as a separate reactor. Although, single cell arrays have been previously demonstrated, these devices didn't have the capability to individually isolate each cell. In order to do that, a complicated network of channels and microfluidic valves was necessary. However, such a tool is important for the genetic analysis of rare events, which is typically performed by PCR amplification of single cells. In particular, research has shown, that DNA amplification (i.e. PCR) of multitemplate systems shows amplification bias towards one template, which results to elimination of one event

over the other in the final product. As a result, genetic analysis of single cells in individual reactors is necessary to produce unbiased results, and study heterogeneous cell populations. Our method is a significant contribution to single cell arrays, and will serve as an important tool for genetic analysis of single cells.

The last chapter of this dissertation demonstrates and systematically characterizes a novel microfluidic device for red blood cell (RBC) analysis and detection of blood disorders. The characteristic dimensions of the system resulted to the development of laminar flow profile in the channel, which had three inlets and one outlet. Controlled dilution of the main sample (i.e. central stream) downward the device was accomplished by hydrodynamically focusing it by two side streams with water. As a result, RBCs, which were present in the main sample, experienced controlled osmotic lysis, as they were flowing in the device. Systematic analysis of the concentration profile in the channel was performed by computational methods, and under different flow rates of the inlet streams. The results showed, that RBC lysis depended mostly on the time the erythrocytes remained in the hypotonic solution, rather than the final concentration of the buffer. This device allows the detection of blood disorders on a microfluidic platform with excellent reproducibility.

APPENDICES

APPENDIX A - FABRICATION OF MICROFLUIDIC DEVICES

Multilayer soft lithography based on polydimethylsiloxane (PDMS, R. S. Hughes Company, Sunnyvale, CA) was used for the fabrication of the devices. The masks were designed using Macromedia Freehand and printed on a 4000 dpi film by Infinity Graphics (Okemos, MI). SU-8 2025 (Microchem Corporation, Newton, MA) or AZ 9260 (Capitol Scientific Microfabrication Materials, Carrollton, TX) photoresist was spin-coated on a 3-inch silicon wafer (University Wafer, South Boston, MA) for the control channel (30-80 μm deep) and the fluidic channel (~13 μm deep) (Fig. A.1A). A final hard bake of the AZ 9260 features, at 130 ^{o}C for 1 min, created a circular cross-section.

Degassed prepolymer mixture, which consisted of monomer (RTV 615 A) and curing agent (RTV 615 B) at a mass ratio 10:1 was poured in a petri dish on top of the control layer or the single layer master (~5 mm in the PDMS thickness). Prepolymer mixture was also poured on top of the fluidic layer, and was spun at 1100 rpm (~110 μm in the PDMS thickness formed) (Fig. A.1B). All PDMS layers were baked at 80^{o}C for 0.5h. For the case of a multilayer device, the two layers were plasma treated (Harrick Plasma, Ithaca, NY), and were then aligned and bonded. A final bake followed for 45 min to ensure strong bonding between. The access holes for the inlets and the outlets were punched.

If the device was supplemented with gold surface electrodes, the procedure was as follows. On top of pre-cleaned glass slides, a 20 nm-thick layer of titanium (Kurt J. Lesker Company, Clairton,

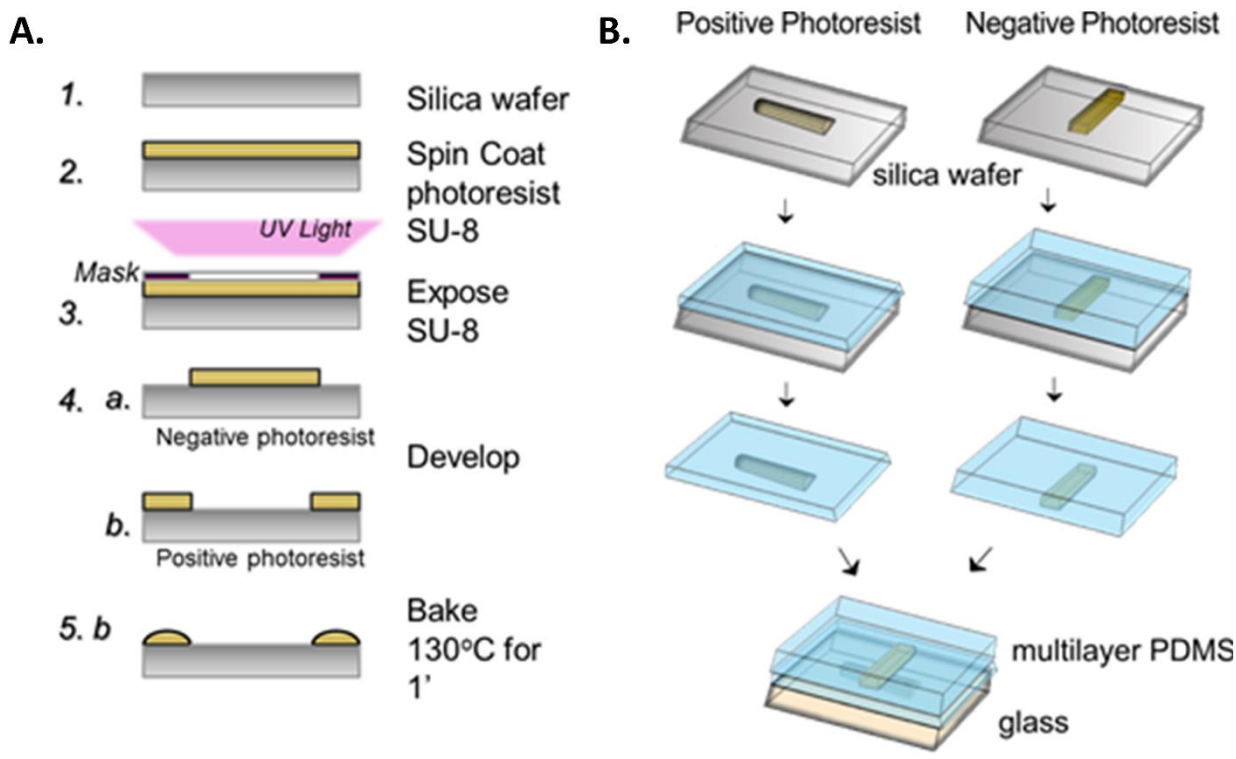

Figure A.1. Device fabrication process. A) Schematic representation of the process for the master fabrication. B) Schematic representation of the multilayer soft lithography technique.

PA) was deposited, followed by the deposition of a 150 nm-thick layer of gold (Kurt J. Lesker Company, Clairton, PA) using an e-beam evaporator (PVD 250; Kurt J. Lesker Company, Clairton, PA). The metal layer was then patterned using AZ 9260 before being wet-etched using standard gold etchant (Aldrich, Milwaukee, WI) and titanium etchant ($HF:H_2SO_4$:DI water=1:1:10). The remaining photoresist was stripped using acetone, leaving 2 surface electrodes of 120μm wide each and 1 mm apart.

Finally, the PDMS layers and the glass slide were bonded using oxygen plasma. A final bake at 80 ^oC for 0.5 h followed to create the assembled microfluidic device.

APPENDIX B – CELL CULTURES

CHO-K1 (ATCC, Manassas, VA) cells were grown in F-12K growth medium supplemented with 10% Fetal Bovine Serum (Atlanta Biologicals, Flowery Branch, GA) and 100 U/ml penicillin−100 mg/mL streptomycin (Life Technologies Corporation, Grand Island, NY) in a 25 cm^2 flask, and in a humidified incubator containing 5% CO_2 at 37 °C. Every 2 days they were trypsinazed and subcultured at a ratio of 1:10 in order to be maintained in the exponential growth phase.

Jurkat cells (ATCC, Manassas, VA) were grown in a humidified incubator containing 5% CO_2 at 37^{o}C in RPMI-1640 growth medium supplemented with 10% Fetal Bovine Serum. The cell concentration was measured every day using a hemocytometer, and fresh medium was added to the flask when needed, to keep the cell concentration below 3×10^6 cells/ml.

Before the experiment, the cells were harvested, by centrifugation at 300 g for 5 min at room temperature, and washed with phosphate buffer saline (PBS, Fisher Scientific, Suwanee, GA). Later, they were resuspended in the buffer required by each experiment, and at a concentration determined by a hemocytometer. Cells were incubated on ice until use. For fluorescently labeled cells, several dyes and methods were used:

Hoechst 33342 (Life Technologies Corporation, Grand Island, NY) was used to label the cells by intercalation on their DNA. Prior to washing, the cells were kept in medium at 3×10^6 cells ml^{-1}, and Hoechst 33342 was added to a final concentration of 10 μg ml^{-1}. Incubation at a water bath maintained at 37^{o}C for 45 min followed. Finally, they were washed with PBS and resuspended in the phosphate buffer.

Propidium iodide (Life Technologies Corporation, Grand Island, NY) dye was used to label the dead cells. The dye solution was added to the cell suspension at a concentration of 1 μg ml^{-1}. The cell suspension was incubated in the dark, and at room temperature for 15 minutes. Finally the cells were washed with PBS by centrifugation at 300g for 15 minutes, and were resuspended in PBS.

APPENDIX C – MATLAB CODE FOR IMAGE ANALYSIS OF CELLS

To analyze the standard deviation of the position of cells in the microchamber

```
% to analyze the standard deviation of the position of cells in the microchamber

clear all

clc

% tic

A=imread('1.tif');

figure, imshow(A,[])

title('A, original image')


% if you want to extract the background

background=imopen(A,strel('disk',15));

I=imsubtract(A,background);

% figure, imshow(I,[])

% title('I, background extracted')


h=mat2gray(I);

% T=graythresh(h);

% j=im2bw(h,T);

% figure, imshow(j)
```

```
% title('j, im2bw with T')
% if T is not correct

% T needs to be adjusted at every image!
T=0.1428;
j2=im2bw(h,T);
figure, imshow(j2)
title('j2, im2bw with adjusted T')
hold on
% PP=imcrop(j2);
% figure, imshow(PP)
% title('PP')

j=j2;

% Now, get the standard deviation in the x and the y axis
[X,Y]=size(j);
z=sum(sum(j));
COM=0;
COM2=0;
   for x=1:X
      for y=1:Y
%           Count the white pixels, or else move forward
```

```
        if j(x,y)==1
            com=y/(z);
            COM=com+COM;
            com2=(y^2)*j(x,y)/z;
            COM2=com2+COM2;
        end
    end
  end
COM
P1=[COM,1];
P2=[COM,X];
plot([P1(1),P2(1)],[P1(2),P2(2)],'Color','r','LineWidth',2)
stdev2=sqrt(COM2-COM^2)

[X,Y]=size(j);
z=sum(sum(j));
COMY=0;
COM2Y=0;
  for x=1:X
    for y=1:Y
%         Count the white pixels, or else move forward
        if j(x,y)==1
            comY=x/(z);
```

```
            COMY=comY+COMY;
            com2Y=(x^2)*j(x,y)/z;
            COM2Y=com2Y+COM2Y;
        end
    end
  end
COMY
P1=[1,COMY];
P2=[Y,COMY];
plot([P1(1),P2(1)],[P1(2),P2(2)],'Color','r','LineWidth',2)
stdev2Y=sqrt(COM2Y-COMY^2)

% toc
```

To stitch many videos together to a single video

```
% to stitch many videos together to a single video
% all pulses.m
A=imread('0.tif');
imwrite(A,'all_pulses.tif','WriteMode','append','compression','none');
for i=1:50
fname=[num2str(i),'.tif'];
info=imfinfo(fname);
num_images=numel(info);
   for k=1:num_images
      A=imread(fname, k, 'Info', info);
      imwrite(A,'all_pulses.tif','WriteMode','append','compression','none');
   end
end
```

To calculate the mean intensity of cells

```
% calculate the mean intensity of cells
clear all
clc
a(2000)=0;
average(20)=0;
for i=1:6
    fname=[num2str(i),' 250.tif'];
    figure (1),
    subplot(1,2,1);
imshow(imread(fname),[]);
text(1400,1,fname)
subplot(1,2,2);
    I= imcrop(imread(fname));
sI=size(I);
for n=1:sI(1)
    for m=1:sI(2)
        if I(n,m)==4095
            I(n,m)=min(min(I));
        end
    end
end
```

```
% imshow(I,[])
% figure, imshow(I,[])
I_eq = adapthisteq(I);
bw = im2bw(I_eq, graythresh(I_eq));
% figure, imshow(bw)
bw2 = imfill(bw,'holes');
bw3 = imopen(bw2, ones(5,5));
bw4 = bwareaopen(bw3, 40);
bw4_perim = bwperim(bw4);
figure (2), imshow(bw4);
title(fname);
% addpath ( 'T:/Documents on T/Projects/matlab codes' );
% overlay1 = imoverlay(I_eq, bw4_perim);
% figure, imshow(overlay1,[])
for n=1:sI(1)
   for m=1:sI(2)
      if bw4(n,m)==1
         a=I(n,m);
      end
   end
end
average(i)=mean(a)
end
```

APPENDIX D – SPECTRUM OF FLUOROPHORES

Fluorophore	*EX (nm)**	*EM (nm)***	*Application*
Hoechst 33342	350	461	Cell-permeant nucleic acid stain
SYTOX Green	504	523	Nucleic acid stain; impermeant to live cells
EGFP	487	509	Protein labeling in live cells
Propidium Iodide	535	645	Nucleic acid stain; impermeant to live cells
Fluorescein	490	525	Fluorescently labels the solution

* EX : excitation wavelength; data from Life Technologies, Inc.

** EM : emission wavelength; data from Life Technologies, Inc.

APPENDIX E – PLASMID PREPARATION

The pEGFP-C1 plasmid vector (4.7 Kb, Clontech, Palo Alto, CA), which encodes enhanced green fluorescent protein (EGFP), was delivered to mammalian cells during the electroporation experiments. Prior to the experiments, it was amplified in Escherichia Coli. The QIAfilter Plasmid Giga kit (QIAGEN, Valencia, CA) was used to extract the plasmid from the bacteria, and purify it, according to the protocol. After purification, it was resuspended in Tris-EDTA buffer, and it was stored at -80^{o}C. The buffer concentration was measured using a spectrophotometer, and by determining the absorbance at 260 nm.

PUBLICATIONS

JOURNAL PAPERS

1. **Loufakis, D.N.**, Cao, Z., Ma, S., Mittelman, D., Lu, C. Focusing of mammalian cells under an ultrahigh pH gradient created by unidirectional electropulsation in a confined microchamber. *Chemical Science* 5 (2014) 3331-3337 *(impact factor 8.314)*

2. Ma, S., **Loufakis, D.N.**, Cao, Z., Chang, Z., Achenie, L., Lu, C. "One-pot" Genetic Analysis of Cells Based on Microfluidic Polymerase Chain Reaction. *Lab on a Chip* 14 (2014) 2905-2909 (*impact factor 5.695)*

3. del Rosal, B., Sun, C., **Loufakis, D.N**., Lu, C., Jaque, D. Thermal loading in flow-through electroporation microfluidic devices. *Lab on a Chip* 13 (2013) 3119-3127 *(impact factor 5.697)*

4. Zhan, Y., **Loufakis, D. N.**, Bao, N. and Lu, C. Characterizing osmotic lysis kinetics under microfluidic hydrodynamic focusing for erythrocyte fragility studies. *Lab on a Chip* 12 (2012) 5063-5068 *(impact factor 5.697)*

5. Ma, S., Schroeder, B., Sun, C., **Loufakis, D.N.**, Cao, Z., Sriranganathan, N., Lu, C. Electroporation Significantly Increases Bioavailability of Cell-Penetrating Peptide (CPP)-Peptide Nucleic Acid (PNA) Conjugates for Antisense Inhibition of Intracellular Salmonella in Macrophages. Submitted to Integrative Biology. *(impact factor 4.321)*

6. **Loufakis, D.N.**, Ma, S., Sun, C., Lu, C. Shear induced electroporation. In preparation

7. **Loufakis, D.N.**, Ma, S., Cao, Z., Lu, C. Electrical lysis of mammalian cells and PCR amplification in a microfluidic device. In preparation

CONFERENCES

1. **Loufakis, D. N.**, Cao, Z., Ma, S., Mittelman, D., Lu, C. Cell allignement under unidirectional electropulsation in a microfluidic device. ***AICHE 2013*** *3-8 Nov 2013, San Francisco, CA* (USA)

2. **Loufakis, D. N.**, Lu, C., Cao, Z., Ma, S., Mittelman, D. Alignment of cells under unidirectional electric pulses. *Invited talk,* ***FACSS SCIX 2013*** *29 Sept- 4 Oct 2013,* Milwaukee, WI (USA)

3. **Loufakis, D. N.**, Varghese, R., Mittelman, D., Lu, C. A Microfluidic device for single cell PCR. ***BMES Annual Meeting*** *24-27 October 2012,* Atlanta (USA)

4. **Loufakis, D. N.**, Varghese, R., Mittelman, D., Lu, C. Single-cell PCR for studying gene mutations. ***ChEGSA Annual Symposium*** *12 April 2012,* Virginia Tech, Blacksburg, VA (USA)

5. Zhan, Y., **Loufakis, D. N.**, Bao, N., Lu, C. Biomechanical study of erythrocytes using microfluidic osmotic lysis. ***BMES Annual Meeting*** *24-27 October 2012,* Atlanta, GA (USA)

6. Zhan, Y., **Loufakis, D. N.**, Bao, N., Lu, C. Rapid lysis of erythrocytes under hydrodynamic focusing reveals cell biomechanics. ***15th International Conference on Miniaturized Systems for Chemistry and Life Sciences (μTAS)*** *2011*, pp 544-546, Seattle, WA (USA)